

# An Effective Particle Approach to the Photophysics of Conjugated Polymers

by

Melissa Anne Pasquinelli

A dissertation submitted in partial fulfillment  
of the requirements for the degree of  
Doctor of Philosophy

in the subject of

**Chemistry**

Carnegie Mellon University  
Pittsburgh, PA 15213

***Examining Committee:***

David Yaron, Advisor

Hyung Kim, Chair

Richard McCullough

David Sholl

**January 2002**

**An Effective Particle Approach  
to the Photophysics  
of Conjugated Polymers**

© Copyright 2002

by

Melissa Anne Pasquinelli

*All rights reserved.*

*To all my best teachers, whose inspiration fed my desire.*

# Contents

<b>List of Figures</b>	<b>vii</b>
<b>List of Tables</b>	<b>xiv</b>
<b>Acknowledgments</b>	<b>xv</b>
<b>Abstract</b>	<b>1</b>
<b>1 Introduction</b>	<b>3</b>
1.1 Introduction to Conjugated Polymers . . . . .	3
1.1.1 Photophysical Essential States . . . . .	5
1.2 Motivation for the Effective Particle Model and Thesis Overview . . . . .	7
<b>2 Background Details of the Theoretical Methods</b>	<b>13</b>
2.1 The Electronic Hamiltonian . . . . .	13
2.2 Hartree Fock Theory . . . . .	14
2.3 Semi-Empirical Models . . . . .	15
2.3.1 Hückel Theory . . . . .	16
2.3.2 Pariser-Parr-Pople (PPP) . . . . .	16
2.3.3 Intermediate Neglect of Differential Overlap (INDO) . . . . .	17
2.4 Excited States via Configuration Interaction . . . . .	18
2.4.1 Equation-of-Motion Method . . . . .	19
2.4.2 Hamiltonian Comparison . . . . .	20
2.5 Periodic Boundary Conditions . . . . .	22
2.6 Dielectric Solvation . . . . .	23
<b>3 Localized Orbital Technique</b>	<b>27</b>
3.1 Introduction . . . . .	27
3.2 Methodology . . . . .	29
3.3 Results and Discussion . . . . .	36
3.3.1 Formation of Localized Molecular Orbitals . . . . .	36
3.3.2 Truncation of Excited State Calculations . . . . .	36

3.4	Conclusion . . . . .	39
3.5	Appendix: The Formation of Hybrid Orbitals . . . . .	40
<b>4</b>	<b>Description of the Effective Particle Approach and Energy Landscapes</b>	<b>42</b>
4.1	Introduction . . . . .	42
4.2	Methodology . . . . .	43
4.2.1	Defining the Effective Particles . . . . .	43
4.2.2	Two Methods for Forming the Effective Particles . . . . .	46
4.2.3	Computational Benefits . . . . .	47
4.3	Applications . . . . .	49
4.3.1	Energy Landscapes . . . . .	49
4.3.2	Position-dependent Effective Masses . . . . .	50
4.4	Results and Discussion . . . . .	51
4.4.1	Chain End Defects in Polyacetylene . . . . .	51
4.4.2	Chain End Effects in PPV . . . . .	54
4.4.3	Chain Length Effects . . . . .	54
4.4.4	PPP vs INDO Hamiltonian for Polyacetylene . . . . .	58
4.4.5	Test of the Separation of the Form of the Effective Particle and Its Dynamics . . . . .	63
4.5	Conclusion . . . . .	69
4.6	Appendix . . . . .	70
<b>5</b>	<b>Application to Chemical Defects</b>	<b>72</b>
5.1	Introduction . . . . .	72
5.2	Methodology . . . . .	73
5.3	Results and Discussion . . . . .	74
5.3.1	Polyacetylene with Carbonyl Defect . . . . .	74
5.3.2	PPV with Carbonyl Defect . . . . .	80
5.3.3	PPV with <i>meta</i> -linkage Defect . . . . .	82
5.4	Conclusion . . . . .	89
<b>6</b>	<b>Application to Conformational Disorder</b>	<b>90</b>
6.1	Introduction . . . . .	90
6.2	Methodology . . . . .	92
6.3	Results and Discussion . . . . .	92
6.4	Conclusion . . . . .	97
<b>7</b>	<b>Application to Exciton-Exciton Interactions</b>	<b>98</b>
7.1	Introduction . . . . .	98
7.2	Formalism . . . . .	99
7.2.1	Scattering Formalism . . . . .	100

7.2.2	Frenkel Scattering Calculations . . . . .	101
7.2.3	Contracted Scattering Calculations . . . . .	102
7.3	Results and Discussion . . . . .	104
7.3.1	Frenkel Excitons . . . . .	105
7.3.2	PPP Oligomers . . . . .	110
7.3.3	Long PPP Chains . . . . .	111
7.4	Summary . . . . .	121
	<b>Bibliography</b>	<b>123</b>

# List of Figures

1.1	A depiction of a light emitting diode. The device functions by injecting electrons and holes into the emitting polymer layer via the electrode layers. The electrons and holes then travel through the polymer layer, combine to form an exciton, and emit a photon of visible light. . . . .	4
1.2	The essential photophysical states for conjugated polymers. The optical gap and the exciton binding energy are also indicated. . . . .	6
1.3	The unit cell structure of the conjugated polymers investigated in this work, polyacetylene and poly-( <i>p</i> -phenylenevinylene). Note that this work will refer to the size of PPV by the number of phenyl rings, rather than the number of unit cells. . . . .	8
2.1	A singly excited configuration for (a) non-localized orbitals obtained from a Hartree-Fock calculation, and (b) segment-localized molecular orbitals. Using localized molecular orbitals enables one to define the unit cell on which the electron or hole is located. . . . .	19
2.2	The electron-hole correlation as a function of the difference between the electron and hole site positions for 20 unit cells of polyacetylene. The PPP Hamiltonian results are represented by square symbols, and the triangle symbols are for the INDO results. The probability at electron-hole separation of zero was doubled in order to account for volume effects. The dotted lines are the electron-hole correlations obtained when the dielectric solvation model in Section 2.6 is included. . . . .	22
2.3	The two limiting dielectric solvation cases. . . . .	24
2.4	The dielectric function, $G( \mathbf{r}_i - \mathbf{r}_j )$ , of Eq. 2.23. The solid line is from explicit calculations on a cylinder of polyacetylene. The effects due to the finite size of the cylinder are removed by splicing the long range form in Eq. 2.24. . . . .	25

3.1	A schematic representation of the procedure used to divide a molecular system into molecular segments. The line between segments is drawn through an atom rather than a bond. The atoms and hybrid orbitals indicated in gray are included in the second segment, the atoms and hybrid orbital in white are included in the first segment. . . . .	30
3.2	A depiction of the block form of a generic Fock matrix. The dimension of the Fock matrix is $N_{AO}$ by $N_{AO}$ , where $N_{AO}$ is the total number of atomic orbitals. Each block represents a segment of the molecule. . .	31
3.3	The geometries of (a) a 3 unit cell oligomer of poly( <i>p</i> -phenylenevinylene) (PPV), (b) <i>p</i> -nitrophenylacetic acid, and (c) a peptide of Cys-His. The segments defined for the orbital localization are depicted. . . . .	33
3.4	Two illustrations of the excited state behavior of the electron and hole for 12 unit cells of PPV that can be generated with the use of segment-localized orbitals; (a) the correlation of the electron and hole as a function of the distance between the electron and hole segments, and (b) the wavefunction probability of the most intense optical state ( $1^1B_u$ ) as a function of the unit cell location of the average position of the electron and hole. . . . .	37
3.5	Excited state energies from INDO/S-CI calculations for a PPV chain of 12 unit cells as a function of (a) the truncation of two electron integrals, $\Delta$ , and (b) limiting the number of single electron-hole configurations by constraining the segment distance the electron and hole can be apart, $m_{e-h}$ . Only the $\pi$ molecular orbitals have been included. . . . .	38
3.6	The hybrid orbital coordinate system, defined from the axes of the bonds with other heavy atoms. . . . .	41
4.1	A depiction of an effective particle, which is made up of a linear combination of electron-hole pair configurations representing an excitation on a molecular segment. The effective particle convention in this depiction is defined according to the electron position. . . . .	44
4.2	The two methods for establishing the form of the effective particles. The first method includes the effects of delocalization in its form, while the other does not. . . . .	46
4.3	An energy landscape for a polyacetylene chain of 20 unit cells, extracted from the full S-CI solution of the INDO Hamiltonian within the $e_{cent}^-$ convention. Each point on the graph represents the energy it takes to create an effective particle on that location in the molecule. No dielectric solvation was included. The $1^1B_u$ state energy obtained from the full S-CI calculation is 2.7 eV. . . . .	49

4.4	An effective mass landscape for a polyacetylene chain of 20 unit cells using INDO with the $e_{cent}^-$ convention (see Fig. 4.3.1). Each point on the graph represents the transfer energy for the effective particle to move to an adjacent location in the molecule. . . . .	50
4.5	Energy landscapes and effective masses for 20 unit cells of polyacetylene with the PPP Hamiltonian both with (dotted lines) and without (solid lines) dielectric solvation included. The $1^1B_u$ state energies obtained from the full S-CI calculations are 2.08 and 2.71 eV, respectively. Results are given for all effective particle center conventions. . . . .	52
4.6	Energy (solid lines) and effective mass (dotted lines) landscapes for 12 unit cells of PPV with different groups at the end of the chain and for different effective particle center conventions. The $1^1B_u$ state energy obtained from the full S-CI calculation for both structures is 3.00 eV. The INDO Hamiltonian was used. No dielectric solvation is included. . . . .	55
4.7	Same as Figure 4.6, but with dielectric solvation included. The $1^1B_u$ state energy obtained from the full S-CI calculation for both structures is 2.39 eV. . . . .	56
4.8	Energy landscapes (bottom) and effective masses (top) for polyacetylene with different chain lengths. The INDO Hamiltonian was used. The effective particles are $e_{cent}^-$ ; the results are comparable for the other types of effective particle center conventions. The results are given without (solid lines) and with (dotted lines) dielectric solvation included. The $1^1B_u$ state energies obtained from the full S-CI calculations are given in Table 4.1. . . . .	57
4.9	Energy landscapes (bottom) and effective masses (top) for PPV with different chain lengths. The INDO Hamiltonian was used. The effective particles are $e_{cent}^-$ ; the results are comparable for the other types of effective particle center conventions. The results are given without (solid lines) and with (dotted lines) dielectric solvation included. The $1^1B_u$ state energies obtained from the full S-CI calculations are given in Table 4.1. . . . .	59
4.10	Energy and effective mass landscapes for 20 unit cells of polyacetylene using both the PPP (dotted lines) and INDO (solid lines) Hamiltonians and for different effective particle center conventions. The $1^1B_u$ state energies obtained from the full S-CI calculations are 2.67 and 2.71 eV, respectively. The PPP curves are the same as those given in Figure 4.5. Dielectric solvation is not included. . . . .	60
4.11	Same as Figure 4.10, but with dielectric solvation included. The $1^1B_u$ state energies obtained from the full S-CI calculations are 2.32 for PPP and 2.08 eV for INDO. . . . .	61

4.12	Energy (solid lines) and effective mass (dotted lines) landscapes for 20 unit cells of polyacetylene for different particle center conventions using the INDO Hamiltonian. The form of the effective particles was calculated in two ways, as depicted in Fig. 4.2. The first method includes the effects of the delocalization dynamics (square symbols), and the second method has the dynamics turned off (triangle symbols). No dielectric solvation is included. The $1^1B_u$ state energy obtained from the full S-CI calculations is 2.71 eV and the $1^1B_u$ state energies obtained from the frozen calculations are 3.18, 2.77, and 2.94 eV for the $e^-h_{cent}^+$ , $e_{cent}^-$ , and $h_{cent}^+$ effective particles, respectively. The square symbol curves are the same as those given in Figure 4.10. . . . .	64
4.13	Same as Figure 4.12, but with dielectric solvation included. The $1^1B_u$ state energy obtained from the full S-CI calculations is 2.08 eV and the $1^1B_u$ state energies obtained from the frozen calculations are 2.52, 2.20, and 2.10 eV for the $e^-h_{cent}^+$ , $e_{cent}^-$ , and $h_{cent}^+$ effective particles, respectively. The square symbol curves are the same as those given in Figure 4.11. . . . .	65
4.14	Same as Figure 4.12, but with the PPP Hamiltonian. . . . .	67
4.15	Same as Figure 4.13, but with the PPP Hamiltonian. . . . .	68
5.1	Excited state energy levels with and without dielectric solvation for 20 unit cells of polyacetylene with (dotted lines) and without (solid lines) a carbonyl defect at the end of the chain. The numbers indicate the oscillator strength to that state. The probability densities per unit cell for $e_{cent}^-$ effective particles for the lowest two excited states, labelled 1 and 2, are shown at the bottom. The filled squares are for a regular polyene and the open circles are for a polyene with a carbonyl defect. . . . .	75
5.2	Energy landscapes (solid lines) and effective masses (dotted lines) without dielectric solvation for 20 unit cells of polyacetylene with (triangles) and without (squares) a carbonyl defect at the end of the chain. The inset graphs correspond to the probability density per unit cell for the $1^1B_u$ state. The $1^1B_u$ state energies and dipole moments are given in Table 5.1. . . . .	77
5.3	Same as Figure 5.2, except with dielectric solvation included. The $1^1B_u$ state energy obtained from the full S-CI calculation for polyacetylene is 2.18 eV, and is 2.19 eV with the carbonyl defect. . . . .	79

5.4	The normalized electron-hole correlations per unit cell for 20 unit cells of polyacetylene with (top) and without (bottom) a carbonyl defect at the end of the chain, for $e_{cent}^-$ effective particles. Only the correlations for the half of the chain containing the carbonyl defect are included. Each curve in Figure 5.4 corresponds to a different location of the electron, and the width of the curve indicates the degree to which the hole is bound to the electron at that position. The electron-hole correlation for the defect unit cell is indicated with filled-in symbols.	81
5.5	Excited state energy levels with and without dielectric solvation for 12 unit cells of PPV with (dotted lines) and without (solid lines) a carbonyl defect at the end of the chain. The numbers indicate the oscillator strength to that state. The wavefunction probability per unit cell for $e_{cent}^-$ effective particles for the lowest two excited states are also indicated.	83
5.6	Energy landscapes (solid lines) and effective masses (dotted lines) without dielectric solvation for 12 unit cells of PPV with (triangles) and without (squares) a carbonyl defect at the end of the chain. The inset graphs correspond to the wavefunction probability per unit cell for the $1^1B_u$ state. The $1^1B_u$ state energies and dipole moments are given in Table 5.1.	84
5.7	Same as Figure 5.6, except with dielectric solvation included.	85
5.8	The normalized electron-hole correlations per unit cell for 12 unit cells of PPV with (top) and without (bottom) a carbonyl defect at the end of the chain for $e_{cent}^-$ effective particles. Only the correlations for the second half of the chain is included. The electron-hole correlation for the defect unit cell is indicated with filled-in symbols.	86
5.9	Energy landscapes (solid lines) and effective masses (dotted lines) for 12 unit cells of PPV with (triangles) and without (squares) a <i>meta</i> -linkage defect at the center of the chain. Dielectric solvation is not included. The stars show the landscapes obtained for a regular PPV oligomer with 6 unit cells. The inset graphs show the probability density per unit cell for the $1^1B_u$ state for PPV with (hollow triangles) and without (solid squares) a <i>meta</i> -linkage defect. The $1^1B_u$ state energies and dipole moments are given in Table 5.1.	87
5.10	Same as Figure 5.9, but with dielectric solvation included. The results are qualitatively similar.	88
6.1	The heat of formation vs. the torsion angle, obtained from a MOPAC calculation.	93

6.2	Energy landscapes for the $1^1B_u$ state using $e_{cent}^-$ effective particles of a 8 unit cell PPV oligomer, which is depicted at the bottom of the figure. The torsional angle, $\theta$ is increased from $0^\circ$ to $60^\circ$ . The filled-in symbols give the landscapes for a planar 4 unit cell oligomer (left) and a 4 unit cell oligomer with torsional angles of $40^\circ$ and $60^\circ$ (right). Dielectric solvation is not included. The $1^1B_u$ state energies are given in Table 6.1.	94
6.3	The effective mass landscapes for the system of Figure 6.2, using equivalent notation. . . . .	95
6.4	The probability density for the center of the $e_{cent}^-$ effective particle as a function of the unit cell location of the effective particle center. . .	96
7.1	Excited-state absorption from the $1^1B_u$ one-exciton state, for long chain Frenkel excitons with various $E_{exc-exc}$ , using periodic boundary conditions and $N = 71$ . The dotted line is $K = 0$ , and the solid line is $K = 2$ . The units of intensity are the same for all panels. . . . .	106
7.2	Analysis of the wavefunctions for the states giving rise to the transitions in the spectra in Fig. 7.1 for $E_{exc-exc} = 4.5$ (solid line) and $2.0$ (dotted line). The $K = 2$ wavefunctions have the same form as $K = 0$ . The probability density is shown as a function of exciton-exciton separation, $m_{exc-exc}$ . . . . .	108
7.3	Excited-state absorption from the $1^1B_u$ state, for a Frenkel exciton system with $E_{exc-exc} = 4.5$ (solid line) and $2.0$ (dotted line) and $N$ unit cells. The $1^1B_u$ state energies are indicated by arrows. To allow comparison with chain length, the scale of the axes is the same for all panels, such that a constant height indicates the intensity is linearly dependent on chain length. . . . .	109
7.4	Excited-state absorption for polyenes with $N$ unit cells. The $1^1B_u$ state energies are indicated by arrows. The numbers above the peaks indicate the relative contribution of double electron-hole pair configurations to the relevant excited state. . . . .	112
7.5	Excited state absorption from the $1^1B_u$ state obtained for periodic polyacetylene chains with 71 unit cells and the indicated scattering regions, $n_{scat}$ . The dotted line is $K = 0$ , and the solid line is $K = 2$ . . .	114
7.6	Excited state absorption from the $1^1B_u$ state obtained for periodic polyacetylene chains with $N$ unit cells and a scattering region of $n_{scat} = 9$ . The arrows indicate the $1^1B_u$ state energies, hence where the $2 \times E_{1^1B_u}$ peak is expected. The dotted line is $K = 0$ , and the solid line is $K = 2$ . The marked peaks are explained in the text. . . . .	115

- 7.7 Analysis of the wavefunctions for the states giving rise to the transitions in the  $N = 71$  spectrum of Fig. 7.6. The probability density is shown as function of exciton-exciton separation,  $m_{\text{exc-exc}}$ . The dotted lines show the average probabilities within the scattering region. (Note that the probabilities due to single electron-hole configurations are not included.) 117
- 7.8 Same as Fig. 7.6, but without inclusion of single electron-hole pair configurations in the calculation of the two-photon excited states (D-EOM). . . . . 119

## List of Tables

3.1	The segment-localized molecular orbitals for a 3 unit cell oligomer of PPV. The segments are indicated in Fig. 3.3(a). Each number in the table represents the probability density of the orbital on that segment. The maximum probability for each molecular orbital is indicated in bold. Because the orbitals are written in the unhybridized atomic basis, the $\sigma$ bonds between segments appears as an orbital with probability spread between the respective segments. . . . .	34
3.2	Same as Table 3.1, but for <i>p</i> -nitrophenylacetic acid, whose segments are indicated in Fig. 3.3(b). . . . .	35
3.3	Same as Table 3.1, but for a simple peptide made of His-Cys, whose segments are indicated in Fig. 3.3(c). . . . .	35
4.1	The $1^1B_u$ state energies (in eV) obtained from a full S-CI calculation for polyacetylene and PPV chains of various lengths in Figures 4.8 and 4.9. . . . .	58
5.1	The $1^1B_u$ state energies (eV) and dipole moments (D) obtained from a full S-CI calculation for polyacetylene and PPV chains with and without chemical defects, corresponding to the curves in Figures 5.2, 5.3, 5.6, 5.7, and 5.10. . . . .	78
6.1	The $1^1B_u$ state energies (in eV) obtained from a full S-CI calculation for the 8 unit cell PPV oligomer of Fig. 6.2 and for the 4 unit cell oligomer obtained from the right side of the structure shown in Fig. 6.2.	94
7.1	Analysis of the wavefunctions giving rise to the transitions in the spectra of Fig. 7.6. The relative probabilities are listed for single electron-hole pair configurations ( $\%$ singles) and for double electron-hole pair configurations within ( $<n_{\text{scat}}$ ) and outside ( $>n_{\text{scat}}$ ) of the scattering region. The $K = 0$ and the corresponding $K = 2$ peaks are aligned in the table. . . . .	116

## Acknowledgments

Who we are is not only comprised of the knowledge we have gathered, but also of those who have influenced us. I am lucky to have been influenced by many incredible people, and I want to thank all of them for being a part of who I am today.

First, I would like to thank my family. Mom and Dad, thank you for teaching me to never give up, and for being so patient with my curiosity and my desire to take things apart. To all of my grandparents, thank you for your love and support. Paula, I appreciate your attempting to answer many of my questions when we were kids, especially for helping me learn to read, and for not getting too mad at me when I took your belongings apart. John, thank you for being such a loving and supportive brother-in-law. Amanda and Johnny, thank you for being my friends, and for knowing how to make me laugh.

I also want to acknowledge all my teachers from Queen of the World and Elk County Christian High School. Norma Inge, thank you for encouraging an ambitious first grader. Nancy Cartwright, thank you for making math so fun! Sandra Florig, I appreciate your sparking my interest in science. Mary Buerk, thank you for making algebra seem so simple. Greg Snelick, thank you for being such an incredible teacher – for making calculus and trigonometry challenging yet understandable, and for making robotics class so fun that I frequently used my study hall time to do extra assignments. John Kowach, I appreciate all of the encouragement you gave me during high school. Finally, Brian Donahue, thank you for making sure that I got to school everyday, for teaching me all about how our government and economy work, and for encouraging me throughout the years.

I also want to thank my professors at Seton Hill College. Sr. Colette, I appreciate your encouraging my interest in writing and poetry. Sr. Susan Yochum, thank you for being a good role model. Robert Frank, thank you for teaching math so well, and for your encouragement. Sr. Dorothy Jacko, I appreciate your thought-provoking courses. John Cramer, thank you for being a great teacher, and for your guidance and support.

There are many people at Carnegie Mellon who have helped me along my journey, and I want to acknowledge them as well. Rea Freeland, thank you for helping me to learn how to be an effective teacher, for your friendship and encouragement over the years, and for being such a great role model. Hyung Kim, thank you for being an incredible mentor, especially for helping me grow into a better scientist and teacher. Rick McCullough, thank you for all of the encouragement that you have given me, and for being so receptive to graduate student feedback. Linda Peteanu, I appreciate having you as a mentor, and all of the advice you have given me over the years. Bob Stewart, thank you for all of your guidance and support, and for sharing your science cartoons with me. To all of my former recitation students and SI leaders, I appreciate all you have taught me, and your involvement in my enjoyment of teaching. To everyone at the Eberly Center, thank you for guiding me to think more critically about education, and for helping me to improve my teaching and communication skills. To my friendship support group – especially Marion Gehrman, Dan Savin, Jason Weibel, Angela Liu, Rich Pilston, Joanne Kehlbeck, and Nadine Fattaleh – thanks for being there for me. Linda Hooper, I very much appreciate your friendship, support, encouragement, and patience. Ann Follette, I appreciate all of the morning talks that we had, and all of our trips to Ali Baba. Karen Stump, thank you for helping me to become a better teacher, and for all of your support and encouragement. To the library and chemistry department staff, I appreciate your assistance and friendliness. To the past and present members of the Yaron group – especially Jason Weibel, Eric Moore, Ivaylo Ivanov, Aimee Tomlinson, Nitin Patel, Angela Liu, Lu Liu, Ben Janesko, Dan Vogel, Matt Kofke, Mike Karabinos, and Donovan Lange – thank you for all of your support and guidance throughout the years, and for creating a friendly working atmosphere. Last but definitely not least, Dave Yaron, thank you for sharing your knowledge with me, for helping me to become a better communicator, and for believing in me.

Finally, I want to thank my friends and everyone else that has helped me along my journey. Sharon Donahue, thank you for being an incredible mentor, especially for helping me to develop my intellectual curiosity, and for the best orange juice popsicles that I have ever had. Father Leon Hont, I appreciate all of your kindness,

guidance, and love. Marion Gehrmann, thank you for all of our talks about school, life, and everything in-between, and for making sure that I got out of the building once in awhile for lunch. Heidi (Younkin) Nicely, thank you for being such a patient lab partner, and for being a good friend. (I really miss the other half of my brain!) Janet Martha, thank you for giving me a writing internship at AT&T the summer before I started grad school and for making sure that I enjoyed it, for looking out for my well-being ever since, and for being such a wonderful mentor. Dan and Sally Tate, I appreciate your making my time at Dairy Queen feel like more than just a job, and your teaching me about managing a business and how to deal with people. Chris Johnson and Beth LaRosa, thank you for making sure that I had fun once in awhile. Heather and Sean Kozik, I appreciate your support, love and friendship, and for being so fun to be around. For all of my friends that I have not already mentioned – especially Julie (Armanini) Anthony, Angie (Schaut) Bennett, Marcy D’Amore, Brooke Weinert, and Heather Lawrence – thank you for being such great people. Morgan and Madalyn Kozik, thank you for being lovely and fun girls, for making me smile, and for your love. Ed Lewetag, I really appreciate your showing interest in my work, and your helping me to stay in touch with emerging technologies. Bess Lewetag, thank you for the abundance of love and support. Dave and Cheryl Lewetag, thank you for opening your home and heart to me, for all of your wisdom, and for being wonderful role models. Finally, Dave Lewetag, thank you for your friendship, support, encouragement, patience, and love.

## Abstract

An Effective Particle Approach  
to the Photophysics  
of Conjugated Polymers

by

Melissa Anne Pasquinelli  
Doctor of Philosophy in Chemistry

Carnegie Mellon University

David Yaron, Advisor

This thesis develops a computational technique, called “the effective particle approach,” that enables structure-property relationships of conjugated polymers to be extracted from quantum chemistry calculations. This approach views an excited state as containing one or more “effective particles” that move on an energy landscape with a position-dependent “effective mass.” For the 1Bu state of conjugated polymers, the effective particle is an exciton, or bound electron-hole pair. The form of the particle is defined by the relative motion of the electron and hole, and its delocalization is described by its “center-of-mass” motion. This technique yields computational savings as well as interpretive advantages.

This approach relies on the ability to form orbitals that are localized on molecular segments. A technique is developed that uses sub-blocks of the Fock matrix in a hybrid atomic orbital basis to generate reasonable trial functions for each segment, and the local orbitals are then obtained by projecting these trial functions into the proper orbital space. This method can localize occupied/unoccupied molecular orbitals and can include both sigma and pi electrons. This robust technique enables the inclusion of solid-state dielectric effects and yields computational savings in post Hartree-Fock methods.

Effective particles are used to generate energy landscapes and effective mass profiles that provide insight into how the structure of a material relates to its photophysical properties. Calculations on a carbonyl defect in polyacetylene and poly(*p*-phenylenevinylene) (PPV) quantify the degree to which the carbonyl attracts an electron and repels a hole, thereby promoting charge separation that is strongly influenced by dielectric solvation. Landscapes and effective masses for a *meta*-linkage defect and torsional disorder in PPV reveal that even relatively small torsional defects have fairly large effects on the energy and reduced mass landscapes.

This approach is combined with a scattering formalism to study the photophysics of long polymer chains. This methodology is used to investigate whether biexcitons are stable and can be observed in two-photon spectroscopy. The results indicate that biexciton states are not stable in the limit of long chains but could be stabilized on short chains by confinement effects.

# Chapter 1

## Introduction

### 1.1 Introduction to Conjugated Polymers

Conjugated polymers exhibit semiconducting properties because the bonding and anti-bonding  $\pi$  orbitals along the polymer chain form valence and conduction bands that support mobile charge carriers. These polymers are ideal for device applications since they combine the processability and the mechanical properties of polymers with the optical and electronic properties of semiconductors. These properties can be fine-tuned through the flexibility provided by organic synthesis. Due to their combination of photophysical and semiconducting properties, conjugated polymers are promising materials for the construction of devices such as light-emitting diodes<sup>1-5</sup> and solid-state lasers.<sup>6-11</sup>

Light-emitting diodes (LEDs) made with conjugated polymers became an active area of research in 1990 when electroluminescence from poly-(*p*-phenylenevinylene)(PPV) was demonstrated.<sup>12</sup> Polymer-based LEDs are envisioned for applications such as flat-screen displays because of their flexibility,<sup>13</sup> high thermal stability,<sup>1</sup> and ability to emit throughout the visible spectrum.<sup>14-16</sup> Most importantly, LED devices made with organic materials are easier to manufacture and design than active-matrix liquid crystal displays.<sup>1</sup>

These organic LED devices operate by injecting electrons and holes into thin polymer films. The electrons and holes travel through the polymer and combine to form

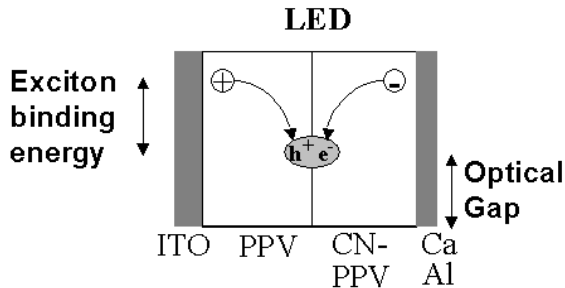


**Figure 1.1:** A depiction of a light emitting diode. The device functions by injecting electrons and holes into the emitting polymer layer via the electrode layers. The electrons and holes then travel through the polymer layer, combine to form an exciton, and emit a photon of visible light.

an exciton, or bound electron-hole pair, which then emits visible light. Figure 1.1 is a depiction of such an organic LED made with PPV and a substituted PPV sandwiched between two electrode layers. The hole-injecting electrode layer is typically made of a material with a high work function, such as indium tin oxide (ITO), and the electron-injecting electrode layer is one with a low work function, such as calcium, aluminum, or magnesium. For optimal efficiency, the amount of electrons and holes injected into the polymer needs to be balanced, since excessive amounts of one of the charges can inhibit exciton formation. Organic materials tend to preferentially transport holes (called p-type semiconductors) because of their low electron affinities,<sup>1</sup> so an electron transport layer is also typically placed into the device to improve device performance. In the device depicted in Figure 1.1, the CN-PPV serves as the electron transport layer.

LED device performance is dependent upon the luminescence efficiency of the polymer material. The luminescence of these polymers tends to be lower in the solid state than for isolated chain molecules because the excitons can migrate to quenching sites, such as aggregates or chemical defects.<sup>17-25</sup> Aggregates can serve as quenching centers because interchain interactions can produce optically dark excited states lower in energy than the optical state that provides a non-radiative pathway to the ground state.<sup>2,26-31</sup> Intercchain interactions can be reduced by attaching bulky side groups to

the conjugated polymer backbone, such as alkyl groups. These side groups serve to dilute the polymer backbones, which minimizes the effects of aggregation, but they can also inhibit the transport of charges through the polymer film.<sup>32</sup> More recently, in order to reduce the significance of  $\pi$  stacking, helical polymer structures have been formed by the inclusion of a biphenyl group in the unit cell structure, which has been shown to increase photoluminescence efficiencies.<sup>33,34</sup> Luminescence is also affected by the structure of the polymer. For instance, structural distortions along the chain, such as a “kink” or torsional disorder along the chain, can reduce the delocalization of the  $\pi$  bonds along the polymer backbone.<sup>29,32,35–40</sup> The planarity of the polymer is affected by the nature of the substituents, temperature, and the choice of solvent.

To improve material design, it is important to understand the effects of chemical defects and chain morphology on the photophysics. This thesis presents a computational approach that enables such structural information to be extracted from quantum chemistry. This method is based on the effective particle language commonly used in the physics community to describe the features of semiconductor materials.

### 1.1.1 Photophysical Essential States

The linear and nonlinear optical properties of  $\pi$  conjugated polymers are dependent upon the energetic location and nature of their excited states. The primary excited states, depicted in Figure 1.2, are identified according to the symmetry labels of the corresponding states in trans-polyacetylene:  $1^1A_g$ ,  $1^1B_u$ ,  $m^1A_g$ ,  $n^1B_u$ , and the free charge continuum.<sup>41</sup> These states are either of even parity ( $A_g$ ) or odd parity ( $B_u$ ), and only transitions between states of opposite symmetry are allowed.

The excited states can be viewed as containing electrons and “holes,” which are formed from the ground state by promoting electrons from filled (valence band) orbitals to the empty (conduction band) orbitals. In the free charge continuum, these electrons and holes move in an uncorrelated manner, meaning that the knowledge of the position of either an electron or hole does not yield any information about the location of the other. Any state that lies below the band edge of the continuum is known as an excitonic state. In these states, the motion of the electron and hole are

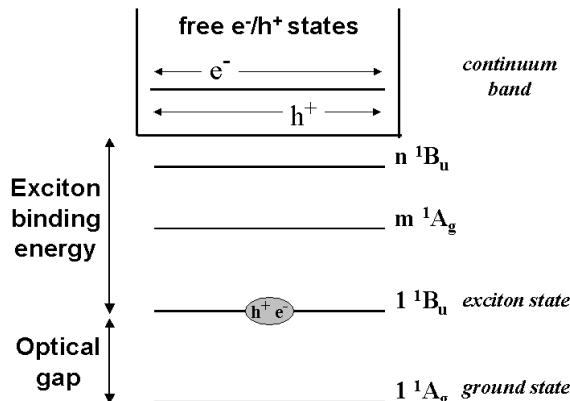


**Figure 1.2:** The essential photophysical states for conjugated polymers. The optical gap and the exciton binding energy are also indicated.

correlated, and therefore the electron and hole are bound. This correlation can be used to interpret the behavior of the electrons and holes in the excited states.

Since the ground state is of  $A_g$  symmetry, the lowest optically allowed one-photon state is the  $1^1B_u$ , and the energy difference between the  $1^1A_g$  and  $1^1B_u$  states is called the optical gap. The  $1^1B_u$  state, which carries most of the one-photon intensity, contains an exciton in which the electron and hole are bound together with an average electron-hole pair separation of about 2.5 unit cells.<sup>42</sup> This state is important for device design because it is believed to be the state that emits the fluorescent photon.<sup>19,39,43</sup> However, there is another state that is close in energy, the  $2^1A_g$  state. This state lies lower in energy than the  $1^1B_u$  in some  $\pi$  conjugated polymers, which creates a non-radiative decay pathway for the  $1^1B_u$  state and significantly reduces the fluorescence yield.<sup>30,44</sup> In phenylene-containing conjugated polymers, the  $2^1A_g$  state lies above the  $1^1B_u$ , and so these polymers are typically used for the construction of LEDs.<sup>45,46</sup>

As described in Section 1.1, many applications of  $\pi$  conjugated polymers, such as LEDs, utilize their luminescent properties. In these devices, an electron and hole are injected into the conjugated polymer layer, such as poly-(*p*-phenylenevinylene). The electron and hole migrate through the material, combine, and then emit a photon. In the language of the essential states described above, the injected electron and hole

correspond to the free charge continuum, and the bound electron and hole that emits the photon is the  $1^1B_u$  state. The difference in energy between the band edge of the continuum and the emitting state is called the *exciton binding energy*. For inorganic semiconductors, the exciton binding energy typically lies in the 10 meV range. In PPV, experimental estimates for the exciton binding energy include 0.2-1.1 eV,<sup>47-53</sup> and theoretical estimates include 0.4-0.9 eV.<sup>48,54-56</sup>

Higher energy states can be reached through multi-photon processes. The  $m^1A_g$  state has a large transition moment from the  $1^1B_u$ , and therefore carries a significant amount of two-photon intensity. The  $n^1B_u$  state has a large transition moment from the  $m^1A_g$ , and can be observed in three-photon experiments.<sup>57</sup>

## 1.2 Motivation for the Effective Particle Model and Thesis Overview

The photophysics of conjugated polymers and other molecular systems can be modelled with electronic structure calculations. As described in Section 1.1, the luminescence efficiency of conjugated polymers is affected by chemical defects and chain morphology. However, the relation between molecular structure and electronic properties can be difficult to interpret from traditional calculations. For instance, a calculation with the Intermediate Neglect of Differential Overlap (INDO) Hamiltonian on a PPV oligomer with 8 benzene rings produces 31  $\pi$  and 31  $\pi^*$  orbitals, each of which is delocalized throughout the polymer chain. In even the simplest theory, such as Singles Configuration Interaction (S-CI), the excited states are composed of thousands of excitations between these  $\pi$  orbitals.

Additional insight can be gained about the electronic structure with the ability to observe how defined components of the system, like functional groups or monomer units, contribute to properties like electronic excitations<sup>58-63</sup> or intramolecular charge transfer.<sup>64-68</sup> This report presents a method, called the “effective particle approach,” that can be used to extract from traditional electronic structure calculations how the structural components of conjugated polymers, such as the unit cells or a defect,

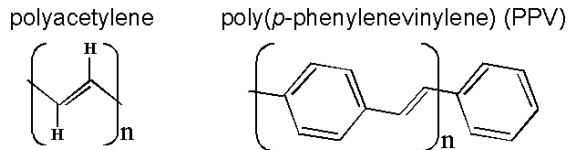


**Figure 1.3:** The unit cell structure of the conjugated polymers investigated in this work, polyacetylene and poly-(*p*-phenylenevinylene). Note that this work will refer to the size of PPV by the number of phenyl rings, rather than the number of unit cells.

affect the electronic properties. This method combines the effective particle language of physics with the computational techniques of quantum chemistry. This work focuses on the  $1^1B_u$  state (see Section 1.1.1) since radiative emission occurs from this state in many conjugated polymers, although other excited states can also be studied with this method. A popular luminescent polymer, poly-(*p*-phenylenevinylene) (PPV), and polyacetylene will be used in order to illustrate the effectiveness of this method. The unit cell structures of these two conjugated polymers are given in Figure 1.3.

Chapter 2 gives background information on the standard tools of quantum chemistry used in this work. Since the study of the photophysics of  $\pi$  conjugated polymers is the main goal,  $\pi$ -electron Hamiltonians such as Pariser-Parr-Pople (PPP) and Intermediate Neglect of Differential Overlap (INDO) have been used. While PPP theory includes only the  $\pi$  electrons, INDO theory includes both the  $\sigma$  and  $\pi$  electrons. Unlike PPP theory, INDO theory has a systematic procedure for deriving the Hamiltonian parameters for arbitrary molecular structure, so INDO can make detailed predictions for structure-property relationships. Also, the PPP Hamiltonian only includes one-electron terms between nearest neighbors, and this causes the valence (hole) and conduction (electron) bands to be symmetric about the Fermi level. The INDO Hamiltonian includes all one-electron terms, which causes the valence bandwidth to increase and the conduction bandwidth to decrease.<sup>69,70</sup> This differing behavior of the electron and hole is referred to as electron-hole symmetry breaking, which makes the hole lighter than the electron in INDO calculations.

The ground state molecular orbitals are calculated with Hartree-Fock theory, and

the excited electronic states are calculated using Configuration Interaction (CI) theory. CI theory represents an excited state as a linear combination of all the possible configurations of electrons and holes within the Hartree-Fock molecular orbitals. The ground state of the system in this report is constrained to remain the Hartree-Fock ground state via the equation-of-motion method so that the calculations are size-consistent, which means that they scale properly with chain length. For ordered systems with translational symmetry, periodic boundary conditions can also be used, which yields computational savings so that the limit of long polymer chains can be investigated.

The computational tool that is crucial to the effective particle model is the ability to decompose the molecular system into components. This ability can be achieved through the use of localized molecular orbitals. Chapter 3 develops a simple yet efficient localized orbital method. This technique uses a projection method to localize molecular orbitals on arbitrary segments of a molecule, such as the unit cells of a polymer. In order to obtain the localized molecular orbitals, trial local orbitals corresponding to the molecular segments are extracted from the Fock matrix, and then the trial orbitals are projected onto the original molecular orbitals. A crucial aspect of this method is the use of hybridized atomic orbitals, which allows molecular segments to be formed without breaking chemical bonds. The molecular orbitals resulting from this localization method are over 80% localized on the defined segments. This localized orbital method is versatile since it can localize both the occupied and unoccupied orbitals, and can handle both  $\sigma$  and  $\pi$  orbitals.

Segment-localized molecular orbitals provide a number of interpretive and computational advantages. The interpretive advantages result from the ability to define a spatial position for the electron and hole in the excited state configurations. There are a number of computational advantages. The spatial position of the electron and hole enables CI calculations to be truncated efficiently by either reducing the two-electron integrals that need to be calculated, or limiting the number of electron-hole configurations that are used to describe the excited states. Also, localized orbitals allow the inclusion of dielectric screening to the interaction of the electron and hole, so that solid-state effects on the photophysical properties can be included. Standard

quantum chemistry models typically incorporate dielectric screening by solvating the average charge distribution, which means that the system is solvated after it has been delocalized. For nonpolar systems, such as the conjugated polymers that are considered in this work, this type of dielectric screening vastly underestimates the dielectric effects. The dielectric screening model that is used in this work, described in Chapter 2, mimics that of inorganic semiconductors, where the electron and hole are each first solvated, and then the charges are delocalized. This model has been shown to accurately capture the effects of the dielectric on conjugated polymers.<sup>71,72</sup> The dielectric parameters are adjusted to experimental observations.

The development of the effective particle model for the photophysics of organic semiconductors is presented in Chapter 4. This approach relies on the segment-localized molecular orbitals from Chapter 3, which allow a spatial position to be assigned to the electron and hole in CI calculations. An effective particle is formed by creating a linear combination of CI electron-hole configurations, or a contracted function,<sup>58,59</sup> that represents an excitation centered on a particular molecular segment. Since many CI basis functions are grouped into a single contracted function with this approach, computational savings are obtained from a reduction of the basis set. The convention for the center of these localized effective particles can be defined according to position of the electron, position of the hole, or the average position of the electron and hole.

The form of the effective particles can be determined in two ways. The first method extracts the form from a full CI calculation, which gives the form of the particle while it is in motion. The second method constructs effective particles “frozen” on a particular segment. The difference between these two methods is that the former method includes the effects of the dynamics in its form, whereas the latter does not. A comparison of these two methods reveals the extent to which the form of the effective particles depends on the dynamics. For polyacetylene, the form and the dynamics can be separated with little loss of accuracy, which can yield substantial computational savings.

The effective particle approach yields useful information on the nature of the excited states, such as the energy landscape and effective mass of the particles. The

energy landscape and effective masses are extracted from the Hamiltonian matrix elements between effective particles. The diagonal Hamiltonian matrix elements represent the energy it takes to create an effective particle on a particular molecular segment, and thus gives the energy landscape. The off-diagonal matrix elements represent the transfer energy of an effective particle to move to another segment in the molecule, and these give the “effective mass” of the particle.

Chapter 4 explores various details about this effective particle approach and the information gained from the energy and effective mass landscapes. The use of both the PPP and the INDO Hamiltonian will be contrasted. The landscape results will be shown to be independent of chain length for reasonably-sized systems. The inclusion of dielectric solvation will also be explored. Finally, chain-end defects will be investigated and shown to act as hard-wall potentials.

The remaining chapters present applications of the effective particle approach to the photophysics of conjugated polymers. Chapter 5 examines how a chemical defect, such as a *meta*-linkage in aromatic substituted systems such as PPV or a carbonyl defect, affects the luminescence efficiency of  $\pi$ -conjugated polymers. Experimentally, it has been observed that *meta*-linkages can increase the luminescence efficiency by breaking the  $\pi$  conjugation along the chain backbone, thereby possibly promoting exciton confinement.<sup>73–75</sup> The presence of carbonyl defects that arise from photo-oxidation of the sample, however, leads to a substantial decrease in emission.<sup>18–25</sup> Energy landscapes and effective mass results are used to show that a *meta*-linkage can in fact lead to exciton confinement, which can enhance emission. These interpretive schemes will also be utilized to quantify the degree to which a carbonyl defect acts as an electron-withdrawing trap. Such a trap can lead to a decrease in the bound character of the exciton, an effect which is enhanced by the ability of the dielectric surroundings to stabilize charge separated configurations. The reduction in the correlation between the electron and hole can lead to dissociation of the exciton, which will quench the luminescence. These results support Rothberg’s suggestion that the carbonyl defect can act as an electron trap.<sup>19</sup>

Chapter 6 explores how conformational disorder along the polymer backbone affects the electronic structure of conjugated polymers. The absorption and emission

spectra of these polymers should scale as the inverse of the chain length, but typically a saturation of the spectra occurs for long chain polymers. The chain length where this saturation occurs is called the effective conjugation length. The absorption and emission spectra also frequently exhibit inhomogeneous broadening. These spectral observations have been attributed to a distribution of conjugation lengths in the sample that is caused by the interruption of the  $\pi$  delocalization. This distribution of conjugation lengths has been attributed to the presence of defects and torsional disorder.<sup>38,76,77</sup> Results are presented for an oligomer of PPV with 8 rings that include torsional disorder along the second half of the polymer chain. The energy and effective mass landscapes indicate that even small torsional disorder of  $10^\circ$  along the polymer backbone can cause the exciton to localize on more ordered segments.

Finally, Chapter 7 examines the formation of biexcitons in conjugated polymers. The calculations combine the effective particle approach with a scattering formalism that provides a size-consistent description of excited states containing both single and double electron-hole pair excitations. Calculations were performed on polyacetylene oligomers with up to 9 unit cells, and on long chains using periodic boundary conditions. Excited-state absorption spectra from the  $1^1B_u$  exciton state will be presented and examined for signatures of biexciton formation. The spectra indicate that polyacetylene with between 7 to 31 unit cells exhibit states with some of the features expected for biexcitons, but such states are not seen in the limit of long chains. These results suggest that exciton-exciton interactions in conjugated polymers are not of sufficient strength to lead to biexciton formation in the limit of long chains, and that their presence in shorter chains is due to confinement effects. Transitions are however found to states with energies above that required to make two free excitons, and that consist of bound electron-hole pairs. These transitions may result from scattering resonances between excitons.

## Chapter 2

# Background Details of the Theoretical Methods

### 2.1 The Electronic Hamiltonian

The Born-Oppenheimer approximation states that to good approximation, the electrons in a molecule can be considered to be moving in a field of fixed nuclei since nuclei are much heavier than electrons. Therefore, the electronic portion to the total energy of the system can be considered independently. The time-independent Schrödinger equation can then be expressed as an eigenvalue problem,

$$\hat{H}_{elec}\Psi_{elec} = \varepsilon_{elec}\Psi_{elec}. \quad (2.1)$$

The electronic Hamiltonian, which describes the motion of  $N$  electrons in the field of  $M$  nuclear point charges is defined as,

$$\hat{H}_{elec} = -\sum_{i=1}^N \frac{1}{2} \nabla_i^2 - \sum_{i=1}^N \sum_{A=1}^M \frac{Z_A}{r_{iA}} + \sum_{i=1}^N \sum_{j>i}^N \frac{1}{r_{ij}}. \quad (2.2)$$

The first two terms are one electron terms; the first one represents the kinetic energy of each of the  $N$  electrons, the second one represents the potential energy between the electrons and nuclei. The third term represents the potential energy between each distinct pair of electrons. Within a basis, the one-electron Hamiltonian matrix elements are defined by  $(i|\hat{h}|j)$ . The two-electron matrix elements using spatial orbitals

are represented by,<sup>78</sup>

$$(ij|kl) = (\psi_i\psi_j|\psi_k\psi_l) = \int d\mathbf{r}_1 d\mathbf{r}_2 \psi_i^*(\mathbf{r}_1) \psi_j(\mathbf{r}_1) (\mathbf{r}_1 - \mathbf{r}_2)^{-1} \psi_k^*(\mathbf{r}_2) \psi_l(\mathbf{r}_2). \quad (2.3)$$

The electronic Hamiltonian in Eqn. 2.2 can be written in terms of its matrix elements using creation and destruction operators,<sup>78</sup>

$$\hat{H} = \sum_{i,j} \sum_{\sigma} h_{ij} a_{i\sigma}^{\dagger} a_{j\sigma} + \frac{1}{2} \sum_{\sigma,\rho} \sum_{i,j,k,l} (ij|kl) a_{i\sigma}^{\dagger} a_{k\rho}^{\dagger} a_{l\rho} a_{j\sigma}, \quad (2.4)$$

where  $a_{i\sigma}$  destroys an electron with spin  $\sigma$  on atom  $i$ , and  $a_{i\sigma}^{\dagger}$  creates an electron with spin  $\sigma$  on atom  $i$ .

There are many methods available for approximate calculations of the electronic structure of molecular systems. The methods used in this work will be described below.

## 2.2 Hartree Fock Theory

Hartree-Fock (HF) theory is the starting point for most electronic structure calculations. HF theory generates the one-electron wavefunctions, or molecular orbitals, and their corresponding energies. This theory describes a single electron moving in an average potential of the other electrons and the nuclei. The HF one-electron wavefunctions,  $\psi_i$ , are typically represented as a linear combination of  $n$  atomic orbitals,  $\chi_j$ ,

$$\psi_i(\mathbf{r}) = c_1\chi_1(\mathbf{r}) + c_2\chi_2(\mathbf{r}) + \cdots + c_n\chi_n(\mathbf{r}). \quad (2.5)$$

The aim of HF theory is to find the best form of the one-electron wavefunctions,  $\psi_i$ , by minimizing the total energy,  $\varepsilon_i$ . This leads to the eigenvalue problem,

$$\hat{F}_i \psi_i = \varepsilon_i \psi_i, \quad (2.6)$$

where  $\hat{F}$  is the Fock operator. The occupied molecular orbitals correspond to the  $m$  lowest eigenvalues of  $\hat{F}$ . The Fock operator,  $\hat{F}$ , is given by,<sup>78</sup>

$$\hat{F}_i = h_i^{(1)} + v^{HF}(i), \quad (2.7)$$

where  $h_i^{(1)}$  represents the one electron terms of Eq. 2.2, and  $v^{HF}(i)$  is the average potential felt by the  $i^{th}$  electron due to the presence of the other electrons. For a closed-shell system with  $N$  electrons,  $v^{HF}(i)$  is given by,

$$v^{HF}(i) = \sum_a^{N/2} 2J_{ia} - K_{ia}. \quad (2.8)$$

$J$  is the coulomb operator, and is described by two electron integrals from Eq. 2.3 of the form  $(ii|aa)$  that give the repulsion between two charge clouds.  $K$  is the exchange operator, described by two electron integrals from Eq. 2.3 of the type  $(ia|ai)$ , which arises from the indistinguishability of electrons and the antisymmetric properties of the electronic wavefunction.

Since the HF potential described in Eq. 2.8 depends on the wavefunctions of the other electrons, the Hartree-Fock equation in Eq. 2.6 must be solved iteratively. Due to this iterative approach, HF theory is also known as self-consistent-field (SCF).

## 2.3 Semi-Empirical Models

A primary difference between various electronic structure models is how the two electron matrix elements in Eq. 2.3 are calculated. The number of integrals that need to be calculated scales as the fourth power of the number of basis functions in the molecule, so calculations for even small molecules can be cumbersome. *Ab initio* methods calculate all of the two electron terms explicitly. Semi-empirical methods choose values for these matrix elements in some approximate way, such as parameterizing the matrix elements to experimental measurements. The most common semi-empirical Hamiltonians for  $\pi$ -electron systems are the Hückel, Pariser-Parr-Pople (PPP), and Intermediate Neglect of Differential Overlap (INDO) Hamiltonians. The differences among these Hamiltonians with respect to the excited state calculations will be discussed in Section 2.4.2.

### 2.3.1 Hückel Theory

The simplest model for describing  $\pi$  electron systems completely ignores the electronic repulsions in Eqn. 2.4. The Hamiltonian can then be written,

$$\hat{H}_{Huckel} = \sum_{i,j=1}^{N_\pi} \sum_{\sigma=\alpha,\beta} h_{ij} a_{i\sigma}^\dagger a_{j\sigma}. \quad (2.9)$$

The matrix elements,  $h_{i,j}$  are defined to be

$$h_{i,j} = \begin{cases} \alpha & i = j \\ \beta & i, j \text{ neighbors} \\ 0 & \text{otherwise} \end{cases} \quad (2.10)$$

### 2.3.2 Pariser-Parr-Pople (PPP)

The PPP Hamiltonian models the  $\pi$ -electron system<sup>62</sup> by including one  $p$  orbital per carbon and assuming zero-differential overlap between these orbitals. Zero-differential overlap sets all two electron matrix elements of Eq. 2.3 to zero except when  $i = j$  and  $k = l$ . The Hamiltonian in Eq. 2.4 then becomes,

$$\hat{H} = \sum_{i,j} \sum_{\sigma} h_{ij} a_{i\sigma}^\dagger a_{j\sigma} + \frac{1}{2} \sum_{\sigma,\rho} \sum_{i,j} (ii|jj) a_{i\sigma}^\dagger a_{j\rho}^\dagger a_{j\rho} a_{i\sigma}. \quad (2.11)$$

In terms of standard semi-empirical parameters, this Hamiltonian can be rewritten as,

$$\hat{H} = \sum_{i,\sigma} \left[ -I - \sum_{j \neq i} \Gamma_{ij} \right] a_{i\sigma}^\dagger a_{j\sigma} + \sum_{i,j,\sigma} \beta_{ij} a_{i\sigma}^\dagger a_{j\sigma} + \frac{1}{2} \sum_{i,j,\sigma,\rho} \Gamma_{ij} a_{i\sigma}^\dagger a_{j\rho}^\dagger a_{j\rho} a_{i\sigma}, \quad (2.12)$$

where  $I$  represents the atomic ionization energy, and  $\beta_{i,j}$  is the one-electron matrix element between electrons on carbons  $i$  and  $j$  in polyenes. One electron matrix elements are included between bonded carbon atoms, with  $\beta_1 = -2.5809$  eV for double bonds and  $\beta_2 = -2.2278$  eV for single bonds. The Coulomb energy,  $\Gamma_{ij}$ , is calculated using the Ohno parameterization,<sup>79</sup>

$$\Gamma_{ij} = \frac{14.397 \text{ eV } \overset{\circ}{\text{Å}}}{\sqrt{\left[ \frac{14.397 \text{ eV } \overset{\circ}{\text{Å}}}{U} \right]^2 + r_{ij}^2}}, \quad (2.13)$$

where  $r_{ij}$  is the distance between the  $i^{th}$  and  $j^{th}$  orbitals and the Hubbard parameter  $U$  is 11.13 eV, the difference between the ionization potential and electron affinity of carbon. The carbon-carbon double and single bond lengths are set to 1.35 and 1.46 Å, respectively, and bond angles are 120°.

### 2.3.3 Intermediate Neglect of Differential Overlap (INDO)

The INDO Hamiltonian models the molecular system by including all valence electrons on each atom. Also, differential overlap between orbitals on the same atom is included, such that the only two electron matrix elements of Eq. 2.3 that are retained are those with  $i, j, k, l \in A$ , where  $A$  is an atomic center. The electronic Hamiltonian in Eqn. 2.4 can then be represented as,

$$\begin{aligned} \hat{H} = & \sum_{i,j} \sum_{\sigma} h_{ij} a_{i\sigma}^{\dagger} a_{j\sigma} + \frac{1}{2} \sum_A^{N_{atoms}} \sum_{\sigma,\rho} \sum_{i,j,k,l \in A} (ij|kl) a_{i\sigma}^{\dagger} a_{k\rho}^{\dagger} a_{l\rho} a_{j\sigma} \\ & + \frac{1}{2} \sum_{A,B}^{N_{atoms}} \sum_{\sigma,\rho} \sum_{i \in A} \sum_{j \in B} (ii|jj) a_{i\sigma}^{\dagger} a_{j\rho}^{\dagger} a_{j\rho} a_{i\sigma}. \end{aligned} \quad (2.14)$$

As with the PPP Hamiltonian in Section 2.3.2, the values for the one and two electron integrals are parameterized<sup>80</sup> to spectroscopic measurements. The one-electron matrix elements on a single atom,  $h_{ii}$ , are obtained from the Slater-Condon factors. Between atoms, the one electron matrix elements are given by,

$$(i|\hat{h}|j) = \bar{S}_{ij} (\beta_A + \beta_B) / 2, \quad (2.15)$$

where  $\bar{S}_{ij}$  is the overlap between the  $i^{th}$  and  $j^{th}$  orbitals, scaled such that the  $\pi$  overlaps between  $p$ -orbitals are multiplied by 1.266 and the  $\sigma$  overlaps between  $p$ -orbitals are multiplied by 0.585.  $\beta_A$  and  $\beta_B$  are semi-empirical parameters that depend only on the respective elements. The overlaps between Slater orbitals are calculated using the method of Rico *et al.*<sup>81</sup>

For the two electronic integrals described by Eqn. 2.3, both Coulomb and exchange integrals (see Section 2.2) are retained for orbitals residing on the same atom,

$$J_{ij}^A = (ii|jj)_{atom\ A}, \quad K_{ij}^A = (ij|ji)_{atom\ A}. \quad (2.16)$$

These values are obtained from the Slater-Condon factors as in Ref. 80. The zero differential overlap approximation is assumed between atoms,

$$(ij | kl) = \Gamma_{AB} \delta_{ij} \delta_{kl}, \quad (2.17)$$

where the  $i^{th}$  orbital is on atom A, and the  $k^{th}$  orbital is on atom B. The Coulomb repulsion between nuclei is also described by  $\Gamma_{AB}$ , and the attraction between an electron on atom A and the core of atom B. The coulomb repulsion is determined from a modified form of the Mataga-Nishimoto formula,

$$\Gamma_{AB} = \frac{1}{2/(\Gamma_{AA} + \Gamma_{BB}) + \varepsilon R_{AB}}, \quad (2.18)$$

where  $\Gamma_{AA}$  is the Hubbard parameter for atom A, and  $R_{AB}$  is the distance between atoms A and B. The form used in INDO is equivalent to that of Eqn. (2.18) with  $\varepsilon = 1/1.2$ , a value chosen to obtain better agreement with the spectrum of benzene.<sup>80</sup> Since the work presented in this thesis investigates long range Coulomb effects,  $\varepsilon$  was set to 1.

Since the intention of the work presented in this thesis is to understand the photo-physics of conjugated polymers, unless otherwise indicated, the excited state calculations using the INDO Hamiltonian were performed using just the  $\pi$  and nonbonding molecular orbitals. This approximation allows for the study of larger polymer systems.

## 2.4 Excited States via Configuration Interaction

Excited states are calculated via Configuration Interaction (CI) theory. In CI, a singly excited configuration is defined by removing an electron from one of the “filled” molecular orbitals and placing it into one of the “empty” molecular orbitals, as depicted in Figure 2.1(a). With the use of segment-localized molecular orbitals (refer to Chapter 3), it is possible to define spatial positions for the electron and hole. This allows the electron-hole configurations to be written in terms of the segment positions of the electron and hole, as depicted in Figure 2.1(b).

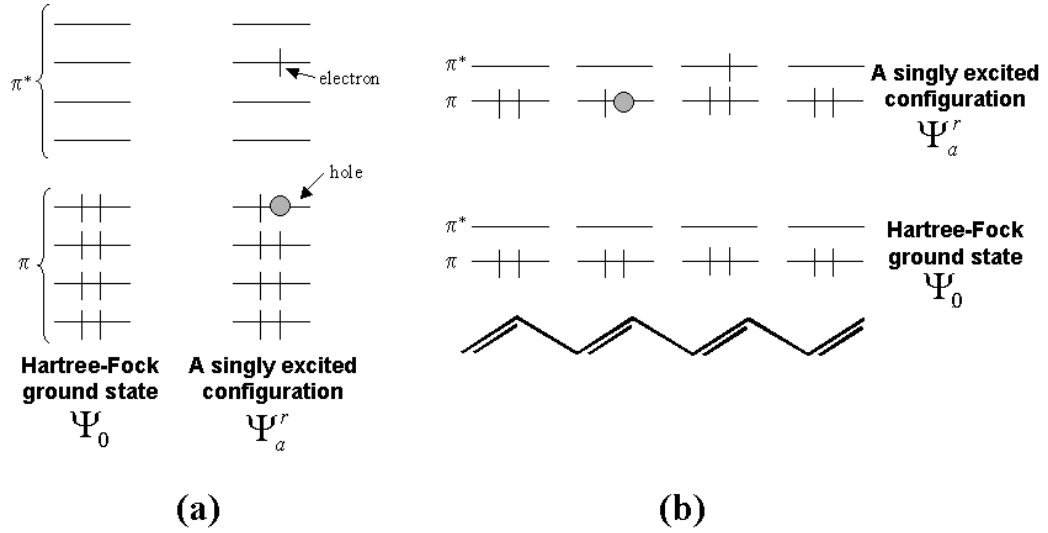


**Figure 2.1:** A singly excited configuration for (a) non-localized orbitals obtained from a Hartree-Fock calculation, and (b) segment-localized molecular orbitals. Using localized molecular orbitals enables one to define the unit cell on which the electron or hole is located.

The excited states in CI theory are described by,

$$\begin{aligned}
 |\text{ES}\rangle &= c_0 |\text{HF}\rangle + \sum_{\substack{a \in \text{occ} \\ r \in \text{unocc}}} c_a^r a_r^\dagger a_a |\text{HF}\rangle + \sum_{\substack{a < b \in \text{occ} \\ r < s \in \text{unocc}}} c_{ab}^{rs} a_r^\dagger a_s^\dagger a_b a_a |\text{HF}\rangle \\
 &= c_0 |\Psi_0\rangle + \sum_{\substack{a \in \text{occ} \\ r \in \text{unocc}}} c_a^r |\Psi_a^r\rangle + \sum_{\substack{a < b \in \text{occ} \\ r < s \in \text{unocc}}} c_{ab}^{rs} |\Psi_{ab}^{rs}\rangle,
 \end{aligned} \tag{2.19}$$

where  $|\text{HF}\rangle$  is the Hartree-Fock ground state,  $a_a$  destroys an electron (creates a hole) in the valence-band orbital on the  $a^{\text{th}}$  unit cell,  $a_r^\dagger$  creates an electron in the conduction-band orbital centered on the  $r^{\text{th}}$  unit cell, and  $c_a^r$  gives the amplitude for finding a hole on the  $a^{\text{th}}$  unit cell and an electron on the  $r^{\text{th}}$  unit cell. The linear expansion coefficients are determined variationally.

### 2.4.1 Equation-of-Motion Method

Size consistency is necessary for the energy obtained in a CI calculation to scale correctly with chain-length in the limit of a long chain. (A size-consistent method

is one that describes both small and large systems with equivalent accuracy.) When only single electron-hole configurations are included (S-CI theory), CI theory is size consistent. However, inclusion of double electron-hole pair configurations (SD-CI) leads to size inconsistencies that prevent proper convergence to a long-chain limit. To overcome this issue, an equation-of-motion (EOM) formalism is used, which has previously been shown to be size consistent.<sup>58,82</sup> This method differs from CI theory in that it constrains the ground state to remain the Hartree-Fock ground state.

The excited electronic states can then be written,

$$| \text{excited state} \rangle = \Omega^\dagger | \text{HF} \rangle, \quad (2.20)$$

where  $| \text{HF} \rangle$  is the Hartree-Fock ground state, and  $\Omega^\dagger$  is a linear combination of electron-hole pair creation operators. In the EOM method, the excitation operator  $\Omega^\dagger$  describes only the difference between the ground and excited states, i.e. it is used only to create electron-hole pairs in the excited state. In CI theory, the excitations are also used to describe electron-correlation in the ground electronic state, and it is this attempt to include ground-state correlation that leads to size inconsistencies. Due to Brillouin's theorem, whereby singles do not interact with the Hartree-Fock ground state, EOM and CI theory are equivalent at the singles level. The differences arise at the doubles level, and SD-EOM is useful since it provides a size-consistent description of excited states containing both single and double electron-hole pairs.

## 2.4.2 Hamiltonian Comparison

In the work presented in this thesis, both the PPP and INDO Hamiltonians have been used to study the excited states of conjugated polymers. However, the nature of both of these Hamiltonians causes differences in the electron and hole bands, which will be explained below.

Conjugated hydrocarbons, such as polyacetylene, and aromatic molecules with an even number of atoms in the ring, like benzene, exhibit alternancy symmetry. A molecule is considered alternant if the atoms can be divided into two disjoint sets in such a way that all members of one set are bonded only to atoms in the

other set. PPV also exhibits alternancy symmetry. For  $\pi$  electron models that only include one-electron matrix elements between adjacent atoms, such as Hückel or PPP theory, the molecular orbitals of alternant molecular structures exhibit interesting characteristics.<sup>83,84</sup> First, the occupied and unoccupied orbitals are “paired;” for every occupied orbital with energy  $E_i$ , there exists an unoccupied orbital at energy  $-E_i$ . Therefore, the valence (or hole) and conduction (or electron) bands are distributed symmetrically. Also, for each bonding/anti-bonding “pair” of molecular orbitals, the coefficients of the same atomic orbital are equal in magnitude, but for one of the two sets of atoms, these coefficients change sign from the occupied to the unoccupied molecular orbital. This alternancy symmetry is also called electron-hole symmetry or charge-conjugation symmetry.

However, the electron-hole symmetry of the molecular orbitals is broken when the INDO Hamiltonian is used because of the inclusion of one-electron matrix elements between all atoms.<sup>69,70</sup> This break in symmetry causes the valence bands to be wider than the conduction bands. The bandwidth for both the occupied and unoccupied molecular orbitals using the PPP Hamiltonian is 5.73 eV for 20 unit cells of polyacetylene. With the INDO Hamiltonian, the bandwidth for the  $\pi$  occupied molecular orbitals in polyacetylene is 6.64 eV, and is 4.03 eV for the unoccupied orbitals. For 12 unit cells of PPV, these values are 7.67 eV and 4.43 eV, respectively. Because the valence band is wider than the conduction band, the hole is lighter than the electron in INDO calculations.

As explained in Section 1.1.1, the correlation between the electron and hole represents the bound character of the exciton. Since the PPP Hamiltonian displays electron-hole symmetry, the most probable location of an electron and the corresponding hole will therefore be on the same site. For the INDO Hamiltonian, this may not necessarily be the case due to the break in electron-hole symmetry. Figure 2.2 shows a comparison of the electron-hole correlation for 20 unit cells of polyacetylene with both the PPP and INDO Hamiltonians. These results show that for polyacetylene, the most probable location of an electron and hole relative to one another is on the same site with the PPP Hamiltonian, but on adjacent sites with the INDO Hamiltonian.

These Hamiltonians will also be contrasted with respect to the intermediate in-

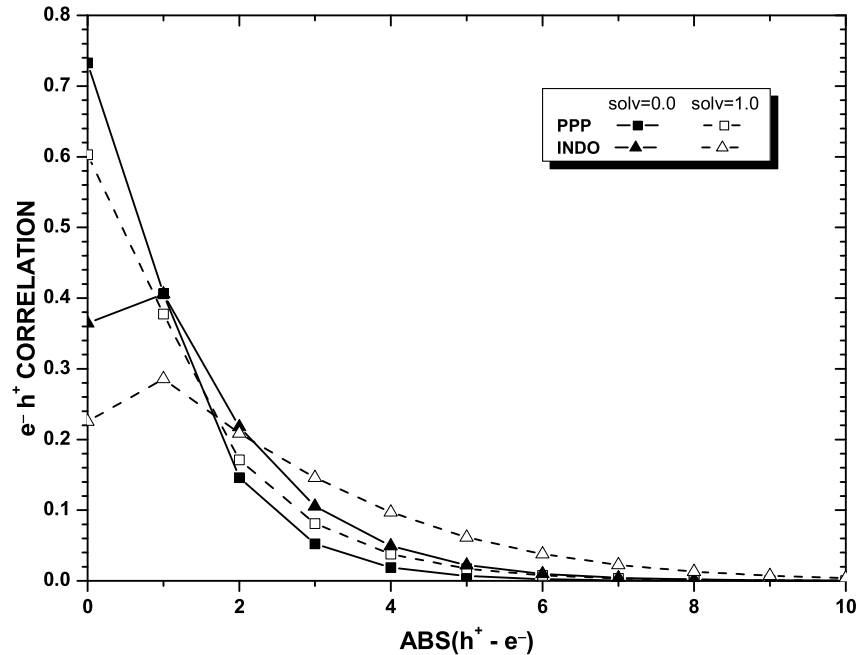


**Figure 2.2:** The electron-hole correlation as a function of the difference between the electron and hole site positions for 20 unit cells of polyacetylene. The PPP Hamiltonian results are represented by square symbols, and the triangle symbols are for the INDO results. The probability at electron-hole separation of zero was doubled in order to account for volume effects. The dotted lines are the electron-hole correlations obtained when the dielectric solvation model in Section 2.6 is included.

formation gained from the effective particle approach in Section 4.4.4.

## 2.5 Periodic Boundary Conditions

Periodic boundary conditions are useful for studying the limit of a long polymer chain.<sup>58,69</sup> Due to the resulting translational symmetry, the excited electronic states may be written,

$$| \text{excited state} \rangle = \frac{1}{\sqrt{N}} \sum_{n=1}^N e^{i(\frac{2\pi}{N})Kn} \Omega_n^{(K)\dagger} | \text{HF} \rangle, \quad (2.21)$$

where the sum is over all  $N$  unit cells and  $K$  is the wave vector that describes the crystal momentum for the motion of the “center of mass” of the electrons and holes.

$\Omega_n^{(K)\dagger}$  creates electrons and holes relative to the  $n^{\text{th}}$  unit cell, and describes the motion of the electrons and hole relative to one another. Due to the translational symmetry of the polymer,  $\Omega_n^{(K)\dagger}$  has the same form on each unit cell,  $n$ , but its form is dependent on the crystal momentum  $K$ . The basis set for the excitation operator  $\Omega_n^{(K)\dagger}$  is a factor of  $N$  smaller than the basis for a corresponding oligomer, and this reduction in basis set is the computational advantage of using translational symmetry.

To be consistent with periodic boundary conditions, the transition moment operator is that for a ring of polymer with  $N$  unit cells.<sup>58,69,85</sup> This leads to a selection rule  $\Delta K = \pm 1$ . The one-photon allowed states then have  ${}^1B_u$  symmetry and  $K = \pm 1$  and the two-photon allowed states have  ${}^1A_g$  symmetry and  $K = 0, \pm 2$ .

The localized orbitals used in periodic boundary conditions are Wannier functions,<sup>69,70</sup> described by,

$$W_n^{\text{band}}(x) = \frac{1}{\sqrt{N}} \sum_{\mathbf{k}} e^{-i\delta_{\mathbf{k}}} e^{-i\mathbf{k}n} \Psi_{\mathbf{k}}^{\text{band}}(x), \quad (2.22)$$

which is the inverse Fourier transform of the Bloch functions. The  $\delta_{\mathbf{k}}$ 's are arbitrary phase factors. The optimal Wannier functions are obtained by finding the  $\delta_{\mathbf{k}}$ 's that minimize the size of the Wannier function.<sup>69,70</sup> This minimization is done with the Simplex algorithm.<sup>86</sup>

Only the calculations in Chapter 7 utilized periodic boundary conditions.

## 2.6 Dielectric Solvation

As described in Section 1.1.1, an important experimental observable in conjugated polymers is the exciton binding energy, the difference in energy between the band edge of the free electron-hole states and the  ${}^1B_u$  exciton state. However, the INDO and PPP Hamiltonians, when applied to a single chain, drastically overestimate the exciton binding energy in conjugated polymers. For instance, INDO calculations on PPV give an exciton binding energy of 3.5 eV, whereas the experimental measurements estimate it to be around 0.2-1.1 eV.<sup>47-53</sup> This overestimation of the exciton binding energy can be overcome with the inclusion of dielectric screening of the electron-hole interaction.

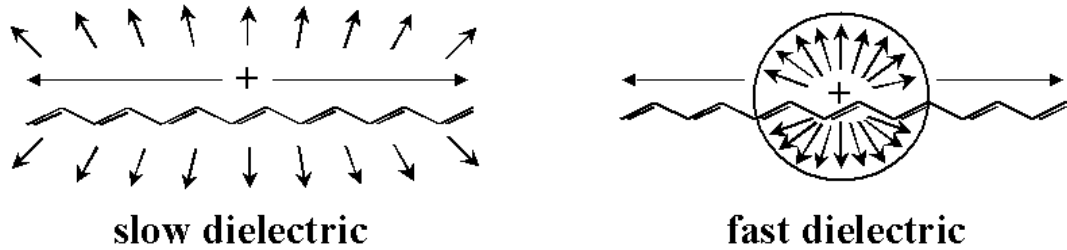


**Figure 2.3:** The two limiting dielectric solvation cases.

There are two well-established models of dielectric screening, which are depicted in Fig. 2.3. The standard model of inorganic semiconductors is a fast dielectric model, which assumes that the solvent polarization is faster than the electron-hole motion, such that the polarization is set by the instantaneous position of the electron and hole. In this model, the electrons and holes are solvated first and then delocalized. The timescale of electron-hole motion is set by the exciton binding energy, and the timescale of the dielectric is set by the optical gap, so the fast dielectric model is valid for systems where the optical gap is much greater than the exciton binding energy. The standard model of quantum chemistry is a slow dielectric model, which assumes that the solvent polarization is slower than the electron-hole motion. In this model, the electron and hole are delocalized first and the averaged charge distribution is then solvated. The slow dielectric model is valid for systems where the optical gap is much less than the exciton binding energy.

So what model applies for conjugated polymers, where the exciton binding energy and the optical gap are the same magnitude? A dynamic dielectric model has previously been developed,<sup>71,72</sup> which is a hybrid of these two models. This model first creates a solvent basis set, with each basis function describing the solvent polarization equilibrated to a particular location of an electron or hole on the solute chain. Product functions are then formed, which combine the S-CI electron-hole configuration for the solute with the corresponding solvent basis functions. The advantage of this model is that it goes smoothly between the fast and slow dielectric limits. It also allows each excited state to be solvated separately, which is important since the elec-

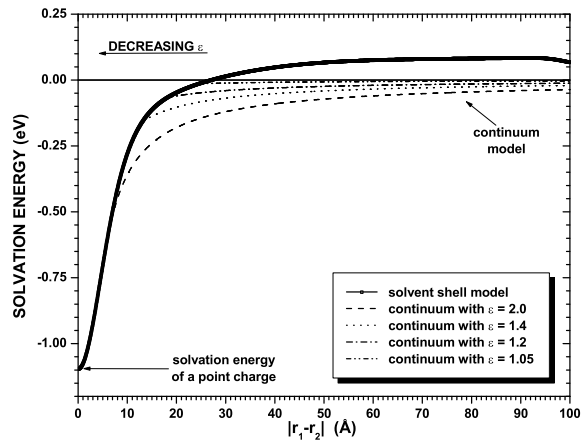


**Figure 2.4:** The dielectric function,  $G(|\mathbf{r}_i - \mathbf{r}_j|)$ , of Eq. 2.23. The solid line is from explicit calculations on a cylinder of polyacetylene. The effects due to the finite size of the cylinder are removed by splicing the long range form in Eq. 2.24.

tron and hole behave differently in each state. The results of this dynamic dielectric model indicate that the fast dielectric model is reasonable for single electron-hole pair states of conjugated polymers.

As will be described in Chapter 3, the advantage of using a site model derived from segment-localized molecular orbitals is that a spatial position for the electron and hole can be assigned. Therefore, it is possible to include a fast dielectric model in these calculations. This fast dielectric model is implemented by adding the solvation energy of the charge distributions corresponding to the electron-hole configurations,  $\Psi_a^r$  and  $\Psi_{ab}^{rs}$ , to the diagonal elements of the CI Hamiltonian matrix.

Within a linear dielectric approximation, the solvation energy of an arbitrary charge distribution is given by,

$$E_{solv} = \sum_{i,j}^N \rho_i \rho_j G(|\mathbf{r}_i - \mathbf{r}_j|), \quad (2.23)$$

where  $\rho_i$  is the charge density at site  $i$ , and  $G(|\mathbf{r}_i - \mathbf{r}_j|)$  describes the energy of interaction between a charge at  $\mathbf{r}_i$  and the polarization induced by a charge at  $\mathbf{r}_j$ . The functional form of  $G(|\mathbf{r}_i - \mathbf{r}_j|)$  is shown in Figure 2.4. At short charge density separations,  $G(|\mathbf{r}_i - \mathbf{r}_j|)$  is calculated explicitly for a cylinder of polyacetylene sol-

vent chains.<sup>72,87</sup> At large charge density separations,  $G(|\mathbf{r}_i - \mathbf{r}_j|)$  is obtained from a continuum dielectric model,

$$G(|\mathbf{r}_i - \mathbf{r}_j|) = \frac{1}{2} \left[ \frac{1 - \varepsilon}{\varepsilon} \right] \frac{1}{|\mathbf{r}_i - \mathbf{r}_j|}, \quad (2.24)$$

where  $\varepsilon$  is the dielectric constant of the material. Organic systems typically have a low dielectric constant. In the calculations presented in this work,  $\varepsilon = 2.0$  was used unless otherwise indicated.  $G(|\mathbf{r}_i - \mathbf{r}_j|)$  is then obtained by splicing together the form obtained from explicit calculations at short distances with the behavior expected at large distances, represented in Figure 2.4.

The solvation energies calculated via Eq. 2.23 are multiplied by a scaling parameter so the calculations can be fit to experimental observations, such as the location of the  $m^1A_g$  or  $1^1B_u$  states. For the polymer systems studied in this thesis, the solvation scales were chosen so that the  $1^1B_u$  state is around 2.5 eV and the  $m^1A_g$  state is 0.6 eV above that. Therefore, for the polymers given in Figure 1.3 used in this work, the solvation scale was set to 1.25 for PPV, and to 1.0 for polyacetylene.

# Chapter 3

## Localized Orbital Technique

### 3.1 Introduction

Electronic structure calculations are useful for investigating the structure-property relationships of molecular systems. Additional insight can be gained from these calculations with the ability to observe how defined components of the system, such as functional groups or monomer units, contribute to properties like electronic excitations<sup>58-63</sup> or intramolecular charge transfer.<sup>64-68</sup> Such studies are aided by localized molecular orbitals, and this chapter presents a robust approach for forming molecular orbitals localized on arbitrary molecular segments.

The localized orbital technique presented here was motivated by our studies of the photophysics of conjugated polymers. Local orbitals make it possible to analyze the results of electronic excited state calculations in terms of effective particle theory by generating energy landscapes for the motion of charge or energy.<sup>59</sup> For instance, we are currently looking at how chemical defects and non-uniform morphologies alter the energy landscapes and thus the photophysics of these systems.<sup>59,88,89</sup> For these applications, it is necessary to have molecular orbitals that are localized on various segments of the molecule, since this allows definite spatial positions to be assigned to the electrons and holes. Local orbitals also lead to computational savings that enable Configuration Interaction (CI) excited state calculations to be performed efficiently on large systems.<sup>58,82</sup> Our goal is an *a posteriori* localization technique that is com-

patible with the INDO model of organic photophysics. Therefore, it is crucial for the localization technique to be able to treat both  $\sigma$  and  $\pi$  orbitals, and to localize both the occupied and unoccupied molecular orbitals.

For periodic systems, Wannier functions provide a useful local orbital basis, and it is these functions that are typically used to construct electron-hole models of semiconductors. The Wannier functions are obtained by taking the inverse Fourier transform of the Bloch functions, and typically leads to orbitals that are well-localized on each unit cell of the system. The technique developed in this chapter can be viewed as providing the functionality of Wannier functions, but in a manner that is applicable to disordered systems. A number of techniques have been developed that grow a molecular system by adding fragments in order,<sup>90–95</sup> and these have some analogy to the construction of molecular orbitals that are localized on fragments. However, the goal of this work is to devise a method that take as inputs the Hartree-Fock solution of a large system and the structure of the desired fragments, and yield a set of Hartree-Fock orbitals localized on these fragments.

Local orbital techniques use either intrinsic or extrinsic criteria for localization. Intrinsic criteria include interaction energy between orbitals and the spatial extension of the orbitals.<sup>96–99</sup> These techniques typically yield orbitals that are localized on bonds or lone pairs, as opposed to molecular fragments. While intrinsic techniques tend to localize filled molecular orbitals effectively, they often fail to localize the unoccupied orbitals. This difficulty with localizing unoccupied orbitals makes intrinsic techniques of limited utility for excited state calculations.

Localization methods based on extrinsic criteria have also been developed.<sup>95,100–108</sup> The extrinsic criteria are typically designed to target the localized orbitals to particular segments. Some methods focus strictly on generating molecular orbitals localized on a particular fragment,<sup>106,109–113</sup> rather than complete transformation of all molecular orbitals to localized orbitals, but such techniques are not of use for our purposes. A particularly effective class of extrinsic techniques are those based on projection. These techniques begin with a set of localized “trial” functions, which have the desired localization properties but which can not, as required for localized Hartree-Fock orbitals, be obtained by a unitary transformation among just the filled or empty canonical

Hartree Fock orbitals. Application of a projection operator followed by an orthogonalization procedure transforms the “trial” functions into valid localized Hartree-Fock orbitals. The success of the projection technique relies on choosing trial functions that will retain their localization properties after application of the projection operator and orthogonalization procedure. Most techniques use localized bond molecular orbitals for the trial functions. For instance, the method developed by Karplus *et al.*<sup>62</sup> uses the  $\pi$  and  $\pi^*$  orbitals of ethylene as trial functions for polyenes, such that each of the trial functions is completely localized to a particular double bond of the polyene. Projection and orthogonalization leads to a slight delocalization of the orbitals, but they retain most of their localized character.

The localized molecular orbital technique described in this report is based on existing projection techniques.<sup>62,102,114–116</sup> The method is versatile since it can localize on molecular segments instead of bonds, and it can handle all valence orbitals. The projected trial functions are extracted from a block-diagonalized form of the Fock matrix. A key step is the use of hybrid atomic orbitals that allow the fragments to be broken across atoms instead of across bonds. This is necessary because breaking fragments across bonds can lead to trial functions that do not retain their localization properties when projected. Localized molecular orbitals obtained from this localization technique are presented for several different kinds of molecular systems, including a conjugated polymer oligomer, a di-substituted benzene, and a simple peptide. Benefits of using segment-localized molecular orbitals in CI calculations are also discussed.

## 3.2 Methodology

The formation of localized orbitals from projection techniques involves two basic steps. First, localized trial functions are determined. Second, these trial functions are projected onto the appropriate molecular orbital space and orthogonalized. The choice of trial functions in the first step is of particular importance since a poor choice of trial functions will lead to poorly localized orbitals after application of the second step.

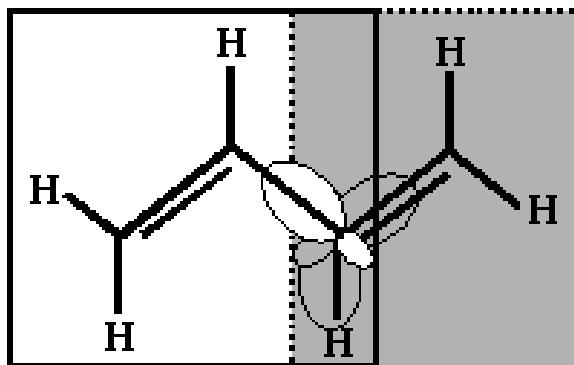


**Figure 3.1:** A schematic representation of the procedure used to divide a molecular system into molecular segments. The line between segments is drawn through an atom rather than a bond. The atoms and hybrid orbitals indicated in gray are included in the second segment, the atoms and hybrid orbital in white are included in the first segment.

In this method, the trial functions are obtained from a block-diagonal form of the Fock matrix, with each block corresponding to a segment of the molecule. The segments for a polymer, for instance, can be the individual unit cells, and the segments for an organic system can be defined according to its functional group constituents. The Fock matrix for a molecule consisting of three molecular segments is shown schematically in Fig. 3.2. The trial orbitals for the first segment are obtained by diagonalizing the sub-block of the Fock matrix corresponding to this segment.

The simplest way to divide the molecule into segments is to draw lines through the bonds connecting various fragments. For instance, butadiene could be fragmented into two  $\text{H}_2\text{CCH}$  subunits. However, this choice breaks a sigma bond and the fragments become radicals. The molecular orbitals of these fragments then bear little resemblance to the local orbitals appropriate for the system when it is bonded to the remainder of the molecule. The trial functions obtained by diagonalizing the Fock matrix corresponding to this fragment will then not be good trial functions.

Appropriate trial functions can instead be obtained by drawing the line between molecular fragments through atoms instead of through bonds, as depicted in Fig. 3.1. To accomplish this, the atomic orbitals on the dividing atom are transformed to

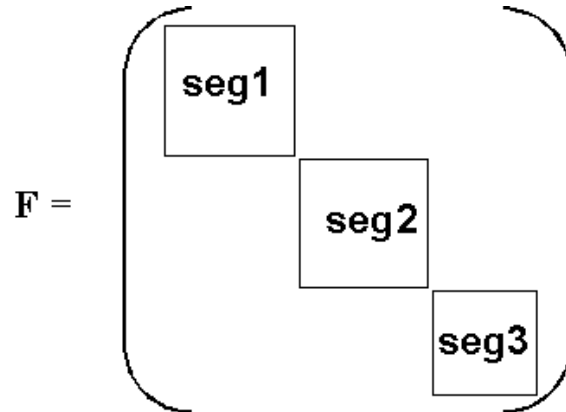


**Figure 3.2:** A depiction of the block form of a generic Fock matrix. The dimension of the Fock matrix is  $N_{AO}$  by  $N_{AO}$ , where  $N_{AO}$  is the total number of atomic orbitals. Each block represents a segment of the molecule.

appropriate hybrid orbitals, and the hybrid that forms a sigma bond with the adjoining molecular segment is absorbed into that segment. This prevents the creation of molecular segments from bond breaking. Fig. 3.1 shows this process schematically for butadiene, with the line between segments drawn through the first carbon atom of the second fragment. This atom is hybridized such that one of its  $sp^2$  hybrids points towards the last carbon atom of the first segment. (The definition of hybrid orbitals is given in the Appendix.) This hybrid orbital is then absorbed into the basis for the first segment, while the rest of the atomic orbitals on this carbon remain in the second segment. The block of the Fock matrix corresponding to the first segment then describes the entire first segment, along with the sigma bond to the second segment. The orbitals obtained from diagonalizing this submatrix thereby reflect the bonding situation present in the actual molecule and provide useful trial functions.

Once the molecular segments are defined, the portion of the Fock matrix representing each of these segments, as depicted in Figure 3.2, is extracted. These submatrices are then individually diagonalized, and the resulting eigenfunctions are used as trial functions for the projection method. For the sake of simplicity, each subsystem is defined to be a closed shell system through the proper choice of dividing atoms. Therefore, the trial functions for the occupied orbitals of segment  $i$  are the lowest

$n_i/2$  eigenfunctions, where  $n_i$  is the number of electrons on segment  $i$ . The remaining eigenfunctions are trial functions for the unoccupied orbitals. For convenience, the trial functions are then expressed in the original non-hybridized atomic basis.

Although the occupied (unoccupied) trial functions have the desirable property of being localized on the molecular segments, they are not valid Hartree-Fock orbitals since they can not, in general, be obtained from a unitary transformation of only the occupied (unoccupied) Hartree-Fock orbitals of the molecule. Rather, the occupied trial functions may have some non-zero component in the unoccupied molecular orbital space, and vice versa. These inappropriate components can be removed by application of an operator that projects the trial function into the appropriate molecular orbital subspace. The effects of these projection operators on the trial functions are defined as,

$$\begin{aligned} P_{\text{occ}} |trial_a^{\text{occ}}\rangle &= \sum_{i=1}^{n_{\text{occ}}} \sum_{j=1}^{n_{\text{tot}}} |\Phi_i\rangle \langle \Phi_i | \phi_j\rangle \langle \phi_j | trial_a^{\text{occ}}\rangle \\ P_{\text{unocc}} |trial_a^{\text{unocc}}\rangle &= \sum_{i=n_{\text{occ}}}^{n_{\text{tot}}} \sum_{j=1}^{n_{\text{tot}}} |\Phi_i\rangle \langle \Phi_i | \phi_j\rangle \langle \phi_j | trial_a^{\text{unocc}}\rangle, \end{aligned} \quad (3.1)$$

where  $\phi_i$  are the atomic orbitals,  $|trial_a^{\text{occ/unocc}}\rangle$  are the trial functions, and  $\langle \Phi_i | \phi_j\rangle$  are the eigenfunctions of the full Fock matrix expressed in the atomic basis. The projected trial functions are then orthogonalized using Löwdin symmetric orthogonalization.<sup>117</sup> The localized molecular orbitals can then be defined as,

$$\begin{aligned} |\tilde{\Phi}_a^{\text{occ}}\rangle &= \sum_{i,j} (\mathbf{S}_{i,j}^{\text{occ}})^{-1/2} P_{\text{occ}} |trial_j^{\text{occ}}\rangle \\ |\tilde{\Phi}_a^{\text{unocc}}\rangle &= \sum_{i,j} (\mathbf{S}_{i,j}^{\text{unocc}})^{-1/2} P_{\text{unocc}} |trial_j^{\text{unocc}}\rangle, \end{aligned} \quad (3.2)$$

where  $\tilde{\Phi}_a$  are the localized molecular orbitals, and  $S_{i,j}$  is the overlap between the  $i^{\text{th}}$  and  $j^{\text{th}}$  projected trial function from Eq. 3.1.

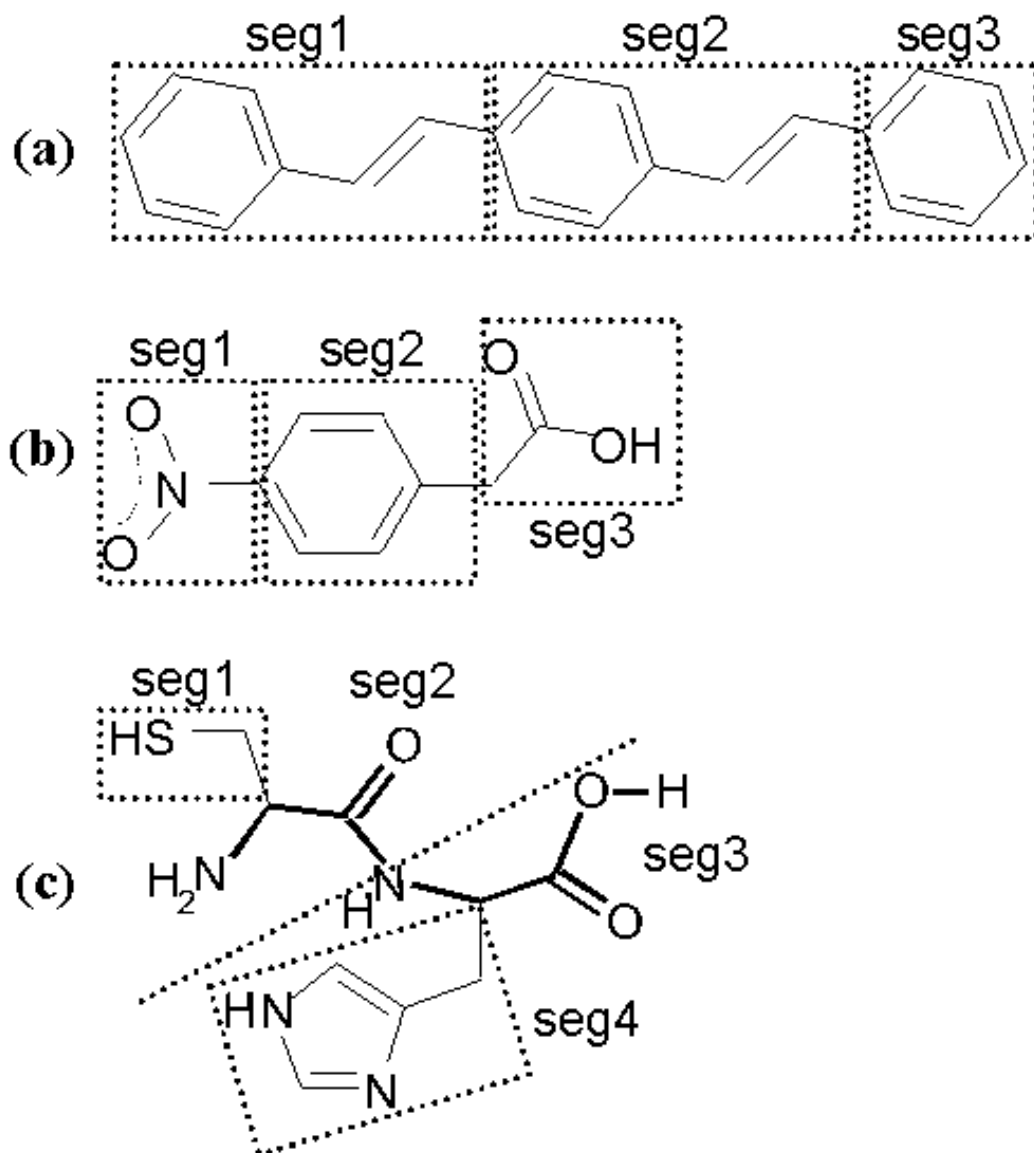


**Figure 3.3:** The geometries of (a) a 3 unit cell oligomer of poly(*p*-phenylenevinylene) (PPV), (b) *p*-nitrophenylacetic acid, and (c) a peptide of Cys-His. The segments defined for the orbital localization are depicted.

**Table 3.1:** The segment-localized molecular orbitals for a 3 unit cell oligomer of PPV. The segments are indicated in Fig. 3.3(a). Each number in the table represents the probability density of the orbital on that segment. The maximum probability for each molecular orbital is indicated in bold. Because the orbitals are written in the unhybridized atomic basis, the  $\sigma$  bonds between segments appears as an orbital with probability spread between the respective segments.

OCCUPIED						UNOCCUPIED													
	Seg1	Seg2	Seg3		Seg1	Seg2	Seg3		Seg1	Seg2	Seg3		Seg1	Seg2	Seg3				
1	$\sigma$	<b>1.00</b>	0.00	0.00	28	$\sigma$	0.00	<b>0.99</b>	0.01	54	$\sigma$	<b>0.50</b>	<b>0.50</b>	0.00	81	$\sigma$	0.00	<b>1.00</b>	0.00
2	$\sigma$	<b>1.00</b>	0.00	0.00	29	$\sigma$	0.00	<b>1.00</b>	0.00	55	$\pi$	<b>0.98</b>	0.02	0.00	82	$\sigma$	0.00	<b>1.00</b>	0.00
3	$\sigma$	<b>1.00</b>	0.00	0.00	30	$\sigma$	0.01	<b>0.99</b>	0.00	56	$\pi$	<b>1.00</b>	0.00	0.00	83	$\sigma$	0.00	<b>1.00</b>	0.00
4	$\sigma$	<b>1.00</b>	0.00	0.00	31	$\sigma$	0.00	<b>1.00</b>	0.00	57	$\pi$	<b>0.99</b>	0.01	0.00	84	$\sigma$	0.00	<b>1.00</b>	0.00
5	$\sigma$	<b>1.00</b>	0.00	0.00	32	$\sigma$	0.02	<b>0.95</b>	0.02	58	$\sigma$	<b>1.00</b>	0.00	0.00	85	$\sigma$	0.00	<b>1.00</b>	0.00
6	$\sigma$	<b>1.00</b>	0.00	0.00	33	$\pi$	0.00	<b>1.00</b>	0.00	59	$\pi$	<b>1.00</b>	0.00	0.00	86	$\sigma$	0.00	<b>1.00</b>	0.00
7	$\sigma$	<b>0.99</b>	0.01	0.00	34	$\sigma$	0.01	<b>0.99</b>	0.00	60	$\sigma$	<b>1.00</b>	0.00	0.00	87	$\sigma$	0.00	<b>1.00</b>	0.00
8	$\sigma$	<b>0.99</b>	0.01	0.00	35	$\pi$	0.01	<b>0.98</b>	0.01	61	$\sigma$	<b>1.00</b>	0.00	0.00	88	$\sigma$	0.00	<b>1.00</b>	0.00
9	$\sigma$	<b>1.00</b>	0.00	0.00	36	$\pi$	0.00	<b>1.00</b>	0.00	62	$\sigma$	<b>1.00</b>	0.00	0.00	89	$\sigma$	0.00	<b>1.00</b>	0.00
10	$\sigma$	<b>0.99</b>	0.01	0.00	37	$\sigma$	0.00	0.06	<b>0.94</b>	63	$\sigma$	<b>1.00</b>	0.00	0.00	90	$\sigma$	0.00	<b>1.00</b>	0.00
11	$\sigma$	<b>0.99</b>	0.01	0.00	38	$\pi$	0.02	<b>0.97</b>	0.02	64	$\sigma$	<b>1.00</b>	0.00	0.00	91	$\sigma$	0.00	<b>1.00</b>	0.00
12	$\sigma$	<b>1.00</b>	0.00	0.00	39	$\sigma$	0.40	<b>0.60</b>	0.00	65	$\sigma$	<b>1.00</b>	0.00	0.00	92	$\sigma$	0.00	<b>1.00</b>	0.00
13	$\sigma$	<b>1.00</b>	0.00	0.00	40	$\sigma$	0.00	0.00	<b>1.00</b>	66	$\sigma$	<b>1.00</b>	0.00	0.00	93	$\sigma$	0.00	0.01	<b>0.99</b>
14	$\pi$	<b>1.00</b>	0.00	0.00	41	$\sigma$	0.00	0.00	<b>1.00</b>	67	$\sigma$	<b>1.00</b>	0.00	0.00	94	$\pi$	0.00	0.02	<b>0.98</b>
15	$\sigma$	<b>0.99</b>	0.01	0.00	42	$\sigma$	0.00	0.01	<b>0.99</b>	68	$\sigma$	<b>1.00</b>	0.00	0.00	95	$\pi$	0.00	0.00	<b>1.00</b>
16	$\sigma$	<b>1.00</b>	0.00	0.00	43	$\sigma$	0.00	0.00	<b>1.00</b>	69	$\sigma$	<b>1.00</b>	0.00	0.00	96	$\pi$	0.00	0.00	<b>1.00</b>
17	$\pi$	<b>0.99</b>	0.01	0.00	44	$\sigma$	0.00	0.00	<b>1.00</b>	70	$\sigma$	<b>1.00</b>	0.00	0.00	97	$\sigma$	0.00	0.00	<b>1.00</b>
18	$\pi$	<b>1.00</b>	0.00	0.00	45	$\sigma$	0.00	0.04	<b>0.96</b>	71	$\sigma$	<b>1.00</b>	0.00	0.00	98	$\sigma$	0.00	0.00	<b>1.00</b>
19	$\sigma$	0.07	<b>0.93</b>	0.00	46	$\sigma$	0.00	0.00	<b>1.00</b>	72	$\sigma$	<b>1.00</b>	0.00	0.00	99	$\sigma$	0.00	0.00	<b>1.00</b>
20	$\pi$	<b>0.98</b>	0.02	0.00	47	$\sigma$	0.00	0.01	<b>0.99</b>	73	$\sigma$	<b>1.00</b>	0.00	0.00	100	$\sigma$	0.00	0.00	<b>1.00</b>
21	$\sigma$	0.00	<b>1.00</b>	0.00	48	$\sigma$	0.00	0.03	<b>0.97</b>	74	$\sigma$	0.00	<b>0.70</b>	0.30	101	$\sigma$	0.00	0.00	<b>1.00</b>
22	$\sigma$	0.00	<b>0.99</b>	0.00	49	$\sigma$	0.00	0.01	<b>0.99</b>	75	$\sigma$	0.01	<b>0.79</b>	0.20	102	$\sigma$	0.00	0.00	<b>1.00</b>
23	$\sigma$	0.00	<b>1.00</b>	0.00	50	$\pi$	0.00	0.01	<b>0.99</b>	76	$\pi$	0.02	<b>0.97</b>	0.02	103	$\sigma$	0.00	0.00	<b>1.00</b>
24	$\sigma$	0.01	<b>0.98</b>	0.01	51	$\pi$	0.00	0.00	<b>1.00</b>	77	$\pi$	0.00	<b>1.00</b>	0.00	104	$\sigma$	0.00	0.00	<b>1.00</b>
25	$\sigma$	0.00	<b>1.00</b>	0.00	52	$\pi$	0.00	0.02	<b>0.98</b>	78	$\pi$	0.01	<b>0.98</b>	0.01	105	$\sigma$	0.00	0.00	<b>1.00</b>
26	$\sigma$	0.00	<b>1.00</b>	0.00	53	$\sigma$	0.00	0.40	<b>0.60</b>	79	$\sigma$	0.00	<b>1.00</b>	0.00	106	$\sigma$	0.00	0.00	<b>1.00</b>
27	$\sigma$	0.03	<b>0.96</b>	0.01						80	$\pi$	0.00	<b>1.00</b>	0.00					



## 3.3 Results and Discussion

### 3.3.1 Formation of Localized Molecular Orbitals

This localized orbital technique was tested on a 3 unit cell oligomer of poly(*p*-phenylenevinylene) (PPV), *p*-nitrophenylacetic acid, and a simple Cys-His peptide. The structures of these systems are illustrated in Figure 3.3, along with the choice of molecular segments. The molecular geometries were optimized with AM1 theory.<sup>118</sup>

The probability densities per segment for both the occupied and unoccupied localized molecular orbitals are given in Tables 3.1, 3.2, and 3.3. These probabilities indicate that the molecular orbitals are over 79% localized on the target segments. Since we are reporting these wavefunction probabilities in the atomic basis rather than the hybrid basis, the sigma orbital between segments appears as a orbital with significant probability density on the adjoining segments. For example, see orbitals 39, 53, 54, and 74 in Table 3.1. The orbitals for PPV in Table 3.1 also maintain excellent  $\sigma/\pi$  separation, as expected for a planar molecule.

### 3.3.2 Truncation of Excited State Calculations

Configuration Interaction (CI) theory is used to calculate the electronic excited state energies. In S-CI theory, the excited state is written as a linear combination of all singly excited configurations. A singly excited configuration is obtained by removing an electron from a filled orbital, creating a hole, and placing it in an empty orbital, creating an electron.

The results of the CI calculations are invariant to the use of localized molecular orbitals. However, using localized molecular orbitals allows the electron and hole to be assigned to particular molecular segments and this leads to several interpretive benefits. For instance, the correlation between the electron and hole for the excited states can be illustrated, which shows the the location probability of the hole relative to the electron. Figure 3.4(a) represents such a depiction of the electron-hole correlation of an oligomer of 12 unit cells of PPV, whose molecular orbital localization is similar to the 2 unit cell system given in Table 3.1. Without segment-localized

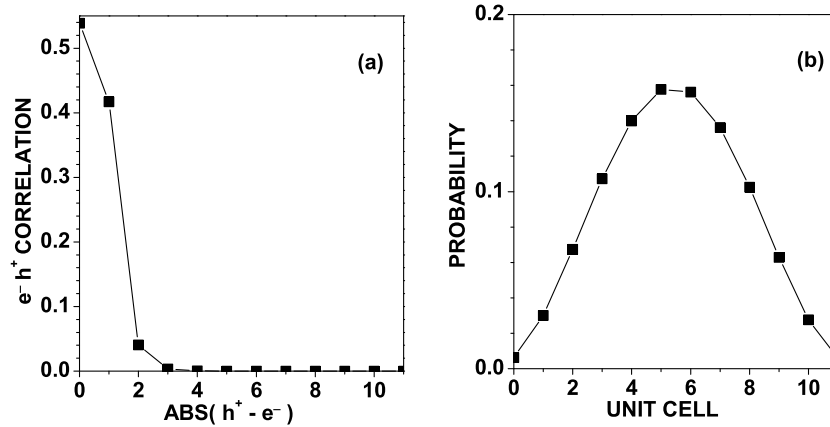


**Figure 3.4:** Two illustrations of the excited state behavior of the electron and hole for 12 unit cells of PPV that can be generated with the use of segment-localized orbitals; (a) the correlation of the electron and hole as a function of the distance between the electron and hole segments, and (b) the wavefunction probability of the most intense optical state ( $1^1B_u$ ) as a function of the unit cell location of the average position of the electron and hole.

molecular orbitals, the electron-hole correlation relative to the electron-hole separation could only be obtained by selecting a particular atomic orbital for the hole position, and looking at the wavefunction probability for the electron relative to that single atomic orbital.<sup>42</sup> A second depiction of the excited state can be generated by observing the wavefunction probability as a function of the unit cell location of the average separation between the electron and hole, as depicted in Figure 3.4(b). Also, since the electron and hole can be assigned to definite positions in the molecule, it is possible to incorporate dielectric screening of the electron-hole interaction into the calculation.<sup>88,89</sup> This screening is an important effect in conjugated polymers.

Localized orbitals also enable two approximations that lead to computational savings in CI calculations on large systems. First, the number of two electron matrix

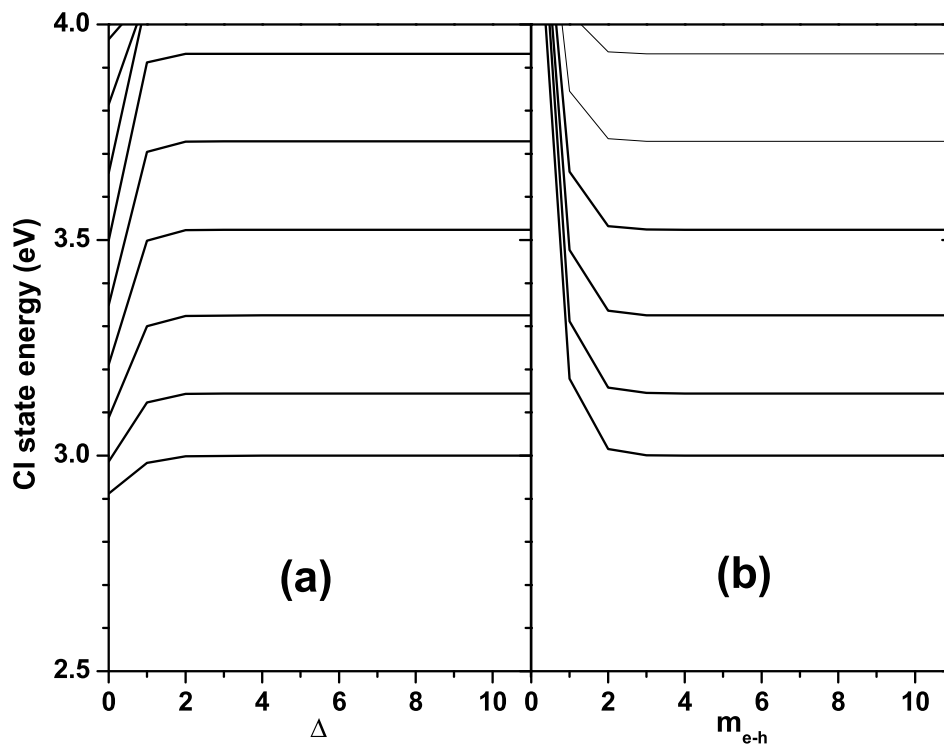


**Figure 3.5:** Excited state energies from INDO/S-CI calculations for a PPV chain of 12 unit cells as a function of (a) the truncation of two electron integrals,  $\Delta$ , and (b) limiting the number of single electron-hole configurations by constraining the segment distance the electron and hole can be apart,  $m_{e-h}$ . Only the  $\pi$  molecular orbitals have been included.

elements in Eq. 2.3 that are calculated and hence stored in the electronic structure calculations can be reduced. A differential overlap approximation can be invoked by assuming that the overlap between  $\psi_i^*(\mathbf{r}_1)$  and  $\psi_j(\mathbf{r}_1)$  is zero if orbitals  $i$  and  $j$  are on molecular segments that are separated by a distance greater than some cutoff parameter,  $\Delta$ . The same applies for orbitals  $\psi_k^*(\mathbf{r}_2)$  and  $\psi_l(\mathbf{r}_2)$ . Therefore, the two electron integrals in which  $ij$  and  $kl$  are on segments greater than a distance  $\Delta$  apart can be taken to be zero. A reasonable choice for  $\Delta$  can be determined by looking at the local character of the molecular orbitals, as in Tables 3.1, 3.2, and 3.3. Figure 3.5(a) shows the S-CI state energies as a function of  $\Delta$  for a PPV chain of 12 unit cells. These results show that the S-CI state energies begin to converge by about  $\Delta = 2$ , which is comparable to the local character of the molecular orbitals in PPV. This approximation enables calculations to be done more efficiently and allows them to be performed on larger systems, since fewer two electron integrals need to be calculated and stored.

The second approximation stems from Figure 3.4, which indicates that the electron and hole remain spatially near one another in the low energy excited states of a large system. Since configurations with large separations between the electron and hole do not contribute to the low-energy states, they can be removed from the basis set used for the CI calculation. Figure 3.5(b) shows the S-CI state energies for a PPV chain of 12 unit cells as a function of the maximum electron-hole pair separation included in the S-CI basis,  $m_{e-h}$ . These results show that the S-CI state energies converge by about  $m_{e-h} = 3$ . This reduces the number of basis functions used in the CI calculations and makes it possible to perform calculations on much larger systems. For instance, for a S-CI calculation on a PPV oligomer with 12 unit cells that includes all  $\pi$  molecular orbitals, using  $m_{e-h} \leq 3$  reduces the size of the basis from 962 to 674 functions.

### 3.4 Conclusion

This chapter presents a simple and robust technique for localizing both occupied and unoccupied molecular orbitals onto molecular segments. The technique combines

a projection methodology with a hybrid-orbital scheme that allows a molecule to be divided into segments without breaking sigma bonds. The results for the three test molecular systems indicate that this technique creates orbitals that are well-localized onto the target segments, such as the unit cells of a PPV oligomer. Whereas the projection method of Karplus<sup>62</sup> works only for pi-electron models, this method works with more complex Hamiltonians such as the INDO method, which includes sigma and pi electrons.

Because this technique can localize both the occupied and unoccupied orbitals effectively, it is well-suited for Configuration Interaction (CI) excited state calculations. These segment-localized molecular orbitals allow for approximations that improve the efficiency and enable calculations to be performed on larger systems. These approximations were shown to have little impact on the CI excited state energies, provided the cutoff parameters are chosen appropriately.

The use of localized molecular orbitals in CI calculations also leads to a number of interpretive advantages. These advantages are the subject of the next two chapters of this thesis.

### 3.5 Appendix: The Formation of Hybrid Orbitals

The hybrid orbitals on the atom dividing two molecular segments are chosen to lie along two bonds. One of these bonds is the bond between the molecular segments. The other bond is between the dividing atom and some other heavy atom. These two bonds are sufficient to determine the appropriate hybridization for the dividing atom. For instance, a bond angle of  $120^\circ$  indicates  $sp^2$  hybridization while a bond of  $180^\circ$  indicates  $sp$  hybridization.

Vectors corresponding to each of the two bonds are first defined as,

$$r_i = r_{\text{hybrid\_atom}} - r_{\text{bonded\_atom}_i}. \quad (3.3)$$

The hybrid orbitals will be defined to lie along these bonds. The axes, depicted in Figure 3.6, are defined as,

$$z' = \frac{1}{N} (r_1 \otimes r_2)$$

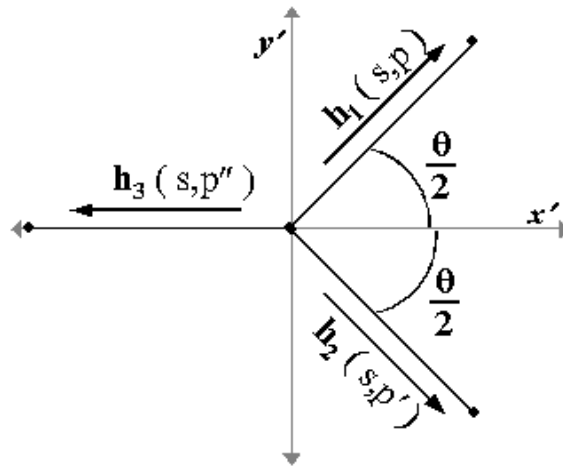


**Figure 3.6:** The hybrid orbital coordinate system, defined from the axes of the bonds with other heavy atoms.

$$\begin{aligned} x' &= \frac{1}{N} \left( \frac{r_1}{|r_1|} + \frac{r_2}{|r_2|} \right) \\ y' &= \frac{1}{N} (z' \otimes x'), \end{aligned} \quad (3.4)$$

where  $N$  is the normalization factor.

The  $sp$  and  $sp^2$  hybrid orbitals are formed by using the following formulas:<sup>119</sup>

$$h'_1 = a_1 s + b_1 \cos\left(\frac{\theta}{2}\right) p'_x + b_1 \sin\left(\frac{\theta}{2}\right) p'_y \quad (3.5)$$

$$h'_2 = a_1 s + b_1 \cos\left(\frac{\theta}{2}\right) p'_x - b_1 \sin\left(\frac{\theta}{2}\right) p'_y \quad (3.6)$$

$$h'_3 = a_2 s - b_2 p'_x \quad (3.7)$$

where  $a_1$ ,  $a_2$ ,  $b_1$ ,  $b_2$ , and  $\theta$  are defined to conserve orthonormalization:

$$\begin{aligned} a_1 &= \sqrt{\frac{\cos\theta}{\cos\theta-1}} & a_2 &= \sqrt{\frac{1+\cos\theta}{1-\cos\theta}} \\ b_1 &= \sqrt{1-a_1^2} & b_2 &= \sqrt{1-a_2^2} \\ \theta &= \arccos\left(\frac{r_1 \bullet r_2}{|r_1| |r_2|}\right) \end{aligned}$$

These equations can generate both  $sp$  and  $sp^2$  hybridization;  $sp$  orbitals are obtained when  $\theta = 180^\circ$  and  $sp^2$  are obtained when  $\theta = 120^\circ$ .

## Chapter 4

# Description of the Effective Particle Approach and Energy Landscapes

### 4.1 Introduction

Much of the qualitative understanding of the photophysics of conjugated polymers is rooted in an effective particle language. For instance, as described in Chapter 1, an electron and hole join to form an exciton in the light emitting diodes used to construct flat-screen displays. The exciton may then migrate through the material and encounter defects, or become trapped in low-energy regions, before decaying either radiatively or non-radiatively.

For the Hamiltonians used in this work (Section 2.3), the  $1^1B_u$  state of conjugated polymers contains an exciton in which the electron and hole are bound together with an average electron-hole separation of about 2.5 unit cells. The relative motion of the electron and hole defines the form of the exciton, and the overall “center-of-mass” motion defines its dynamics. The dynamics is simply the delocalization of the exciton over the entire polymer chain. The basis of the approach outlined in this chapter is to describe this exciton as an “effective particle” that moves on some energy landscape, which has a position-dependent “effective mass.” These energy and effective mass

landscapes are a useful construct for determining the effects of defects and non-uniform morphology on the photophysics, which will be shown in Chapters 5 and 6. The effective particles, energy landscapes, and effective masses are obtained with semi-empirical quantum chemistry.

The focus in this chapter is on the methodology behind forming these effective particles, and the interplay between the form of the effective particles and the dynamics of those particles. The results for polyacetylene suggest that the form of the lowest-energy exciton is only weakly dependent on the dynamics. It is therefore possible to first determine the effective mass and energy landscape of the particle, and then use this information to determine the dynamics.

This method was developed with organic semiconductors, such as conjugated polymers, in mind. Please note that this effective particle approach can be applied to study the photophysics of other systems as well. However, only applications to conjugated polymers will be presented in this work.

## 4.2 Methodology

### 4.2.1 Defining the Effective Particles

Excited states are calculated via the Configuration Interaction (CI) methods described in Section 2.4. In CI theory, a singly excited configuration is designated by removing an electron from one of the occupied molecular orbitals (thus creating a “hole”) and placing it into one of the unoccupied molecular orbitals, as depicted in Figure 2.1. A molecular position for the electron and hole can be defined with the use of localized molecular orbitals (Chapter 3). An excited state is represented by a weighted sum of all of the possible electron-hole configurations.

Effective particles are formed by creating a linear combination of basis functions, or a contracted function,<sup>58,59</sup> that represents an excitation localized on a particular molecular segment, as depicted in Fig. 4.1. Therefore, the overall number of basis functions is reduced. In operator notation, this effective particle is represented by,

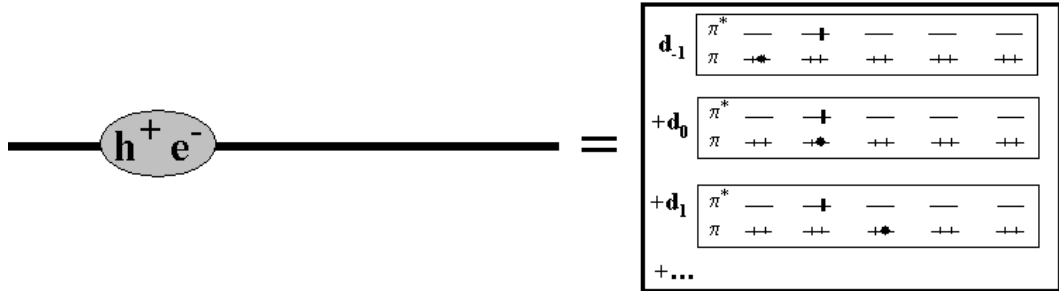


**Figure 4.1:** A depiction of an effective particle, which is made up of a linear combination of electron-hole pair configurations representing an excitation on a molecular segment. The effective particle convention in this depiction is defined according to the electron position.

$$\Omega_n^\dagger = \sum_{\Delta} d_{\Delta}^{(n)} a_{n+\Delta}^\dagger a_n, \quad (4.1)$$

where  $\Omega_n^\dagger$  is normalized and creates an effective particle centered on the  $n^{\text{th}}$  segment. The relative motion of the electron and hole is described by  $d_{\Delta}^{(n)}$ , and thus specifies the form of the effective particle. Note that the form may change with position.

There are several conventions for the effective particles that use different definitions for the center of an effective particle. In the  $e_{cent}^-$  and conventions, the center of the effective particle is defined by the location of the electron or hole, respectively. These two conventions are of use since they allow the behavior of either the electron or hole to be followed as it moves through the molecule. A disadvantage of these conventions is that they do not preserve electron-hole symmetry. To illustrate this, consider a configuration in which the electron is on segment  $n$  and the hole is on and the hole is on segment  $n' \neq n$ . In the  $e_{cent}^-$  convention, this configuration corresponds to an effective particle on segment  $n$ . If the electron and hole are interchanged, the center of the effective particle moves to segment  $n'$ . Interchange of the electron and hole can then effectively cause the effective particle to move. This is not consistent with electron-hole symmetry, which requires that exchange of an electron and hole change at most the phase of the effective particle.

The  $e^-h_{cent}^+$  convention preserves electron-hole symmetry by defining the center of the effective particle as the average position of the electron and hole. Although this  $e^-h_{cent}^+$  convention may seem, at first, to be the most natural, it leads to two complexities. The first is that the effective particle must contract as it approaches the end of the chain. The effects of this contraction will be discussed in detail in Section 4.4.1. The second complexity arises from configurations in which the center of the effective particle lies between two segments. For instance, when the electron is on segment  $n$  and the hole is on segment  $n + 1$ , the center is in-between segments,  $n + \frac{1}{2}$ . One possibility is to combine configurations centered at  $n$  and  $n + \frac{1}{2}$  into a single effective particle centered on segment  $n$ . However, this approach breaks reflection symmetry in oligomers. Consider, for instance, an oligomer with  $N$  identical segments, or unit cells. When the effective particle is on the first unit cell,  $n = 1$ , the effective particle is on the first unit cell,  $n = 1$ , the effective particle includes all electron-hole configurations with centers on  $n = 1$  or  $n = 1 + \frac{1}{2}$ . However, when the effective particle is on the last unit cell,  $n = N$ , the effective particle includes only electron-hole configurations with centers on  $n = N$ . So although the oligomer is symmetric, the effective particle is very different on the first and last unit cell. The  $e^-h_{cent}^+$  convention is therefore defined in a manner that preserves both electron-hole symmetry and reflection symmetry. In this convention, when the average position of the electron and hole lies between segments  $n$  and  $n + 1$ , the configuration is included in both the effective particle centered on  $n$  and that centered on  $n + 1$ . While this convention preserves both electron-hole and reflection symmetry, the inclusion of certain electron-hole configurations in two different effective particles causes the effective particles to overlap with one another, leading to non-orthogonal effective particles. Appendix 4.6 describes how this non-orthogonality is handled in generating energy and effective mass landscapes.

The above three conventions give different perspectives on the energetics and dynamics of the effective particles, each of which provides information on the photo-physics. Which convention is most useful depends on the system under investigation. For instance, the  $e_{cent}^-$  and  $h_{cent}^+$  conventions are useful for examining the tendency of the electron or hole to trap on certain regions of a polymer. The  $e^-h_{cent}^+$  conven-

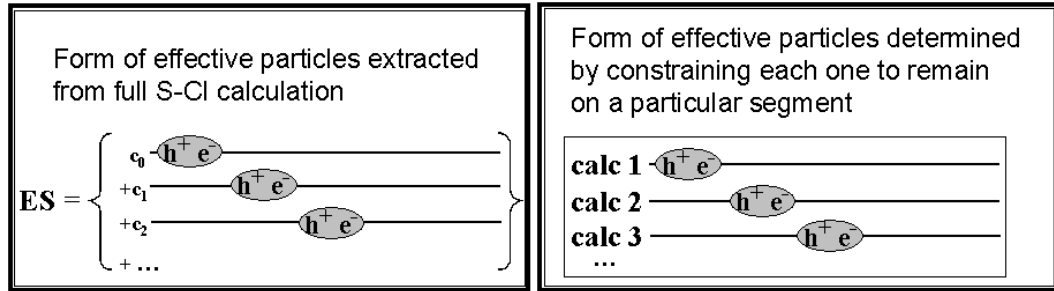


**Figure 4.2:** The two methods for establishing the form of the effective particles. The first method includes the effects of delocalization in its form, while the other does not.

tion is of use when it is important to preserve electron-hole symmetry. Most of the results presented in this work will be given for all three conventions for comparative purposes.

#### 4.2.2 Two Methods for Forming the Effective Particles

The benefits of the effective particle approach result from separating the chemical form of the effective particle from the delocalization, or dynamics, of that effective particle. In this context, the form of the effective particle relates to the motion of the electron and hole relative to one another, while the dynamics relates to the motion of the center of the effective particle. In the notation of Eq. 4.1, the form of the effective particle is set by the coefficients  $d_{\Delta}^{(n)}$ , while the dynamics is set by the amplitude with which the various locations for the effective particle  $\Omega_n$  contribute to the overall wavefunction of a particular state.

The form of the effective particles can be constructed in two ways, as depicted in Fig. 4.2. The first method extracts the form of the effective particle from the full S-CI wavefunction, so the form of these particles include the effects of the delocalization dynamics. The second method constructs effective particles frozen on a particular segment, and so the dynamics are turned off. By comparing the results of these two methods, the effects of delocalization on the form of the particles can be pursued.

To separate the form and the dynamics, Eq. 2.19 can be rewritten using the

operator notation of Eq. 4.1,

$$|\text{ES}\rangle = \sum_n c_n \Omega_n^\dagger |\text{HF}\rangle = \sum_n c_n \sum_\Delta d_\Delta^{(n)} a_{n+\Delta}^\dagger a_n |\text{HF}\rangle, \quad (4.2)$$

where  $d_\Delta^{(n)}$  specifies the form of the effective particle on the  $n^{\text{th}}$  molecular segment and  $c_n$  specifies the dynamics by giving the amplitude for finding the effective particle on the  $n^{\text{th}}$  segment.

In the first method for determining the form of the effective particle, a full S-CI calculation is performed and the resulting wavefunction for the excited state of interest is translated into the form of Eq. 4.2. Since the form of the particle is extracted from the full S-CI wavefunction, these results represent the form of the effective particle as it undergoes the dynamics associated with delocalization over the entire system.

In the second method for determining the form of the effective particle, the dynamics are turned off. These will be referred to as “frozen” effective particles. This is done by constraining the effective particle to remain on a particular molecular segment,

$$|\text{particle frozen on segment } n\rangle = \Omega_n^\dagger |\text{HF}\rangle = \sum_\Delta d_\Delta^{(n)} a_{n+\Delta}^\dagger a_n |\text{HF}\rangle. \quad (4.3)$$

The coefficients,  $d_\Delta^{(n)}$  are determined variationally. This variational calculation is equivalent to a S-CI calculation in a limited basis that contains only those electron-hole configurations that are centered on the  $n^{\text{th}}$  molecular segment. This procedure is performed for all values of the position,  $n$ , and the results give the form that the effective particle adopts when its center is frozen at each of these positions. Once the form of the effective particle is established, the dynamics, or  $c_n$ , can be determined using the variational form in Eq. 4.2.

A comparison of these two methods and the effects of the dynamics on the form of the effective particles is explored in Section 4.4.5.

### 4.2.3 Computational Benefits

Section 3.3.2 discussed the computational benefits of using a molecular site model, which is possible through the use of segment-localized molecular orbitals. These bene-

fits include truncation of the number of configurations included in the CI calculations, and a reduction of the two electron integrals that are calculated and hence stored. Both of these approximations allow calculations to be performed on large molecular systems.

An additional benefit to using the effective particle approach is that it causes a reduction in the basis set for a full dynamical calculation. This computational savings is because a number of basis functions are grouped into one contracted function, as depicted in Fig. 4.1. For instance, a full S-CI calculation on the  $\pi$  system of a polyacetylene chain of 20 unit cells has 400 basis functions. In Eq. 4.2, these are grouped into 20 contracted functions that describe the effective particle centered on each of the 20 unit cells. contracted functions are used to solve for the dynamics of the effective particle, the basis consists of only 20 functions. This reduces the total number of basis functions from 400 to 20. This computational savings is utilized in Chapter 7 in order to study exciton-exciton interactions in long polymer chains.

Computational savings can also be gained if it is possible to separate the form of the effective particles from their dynamics, as discussed in Section 4.2.2. For instance, a complete S-CI calculation with the PPP Hamiltonian on a polyene with  $N$  unit cells uses a basis set containing  $N^2$  functions. The computational effort involved in diagonalizing the Hamiltonian scales as the cube of the number of basis functions, or  $N^6$ . To take advantage of the decoupling of form and dynamics, we may first determine the form of the effective particle on each unit cell, using the variational form of Eq. 4.3. This requires  $N$  calculations, each of which requires  $N^3$  effort, for a total effort that scales as  $N^4$ . Once the form of the particles is known, the dynamics may be determined using the variational form in Eq. 4.2, which scales as  $N^3$ . Therefore, decoupling the determination of the form of the effective particle from the determination of its dynamics lowers the computational effort by a factor of  $N^2$ .

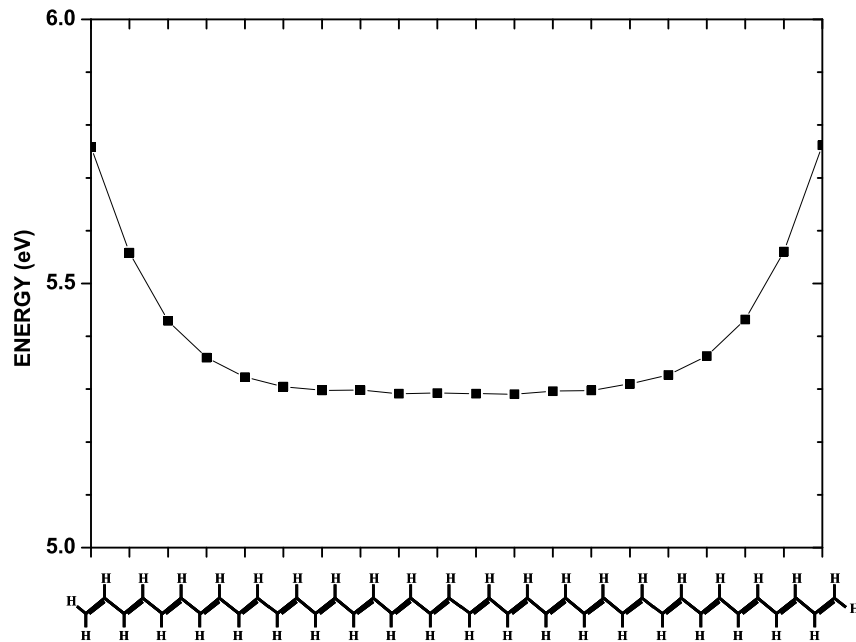


**Figure 4.3:** An energy landscape for a polyacetylene chain of 20 unit cells, extracted from the full S-CI solution of the INDO Hamiltonian within the  $e_{cent}^-$  convention. Each point on the graph represents the energy it takes to create an effective particle on that location in the molecule. No dielectric solvation was included. The  $1^1B_u$  state energy obtained from the full S-CI calculation is 2.7 eV.

## 4.3 Applications

### 4.3.1 Energy Landscapes

The form of the effective particle created by Eq. 4.1 is characterized through the Hamiltonian matrix elements. The diagonal elements,

$$E_n = \langle \text{HF} | \Omega_n \hat{H} \Omega_n^\dagger | \text{HF} \rangle \quad (4.4)$$

give the energy of the particle as a function of  $n$ , the location in the molecule. Fig. 4.3 is an example of an energy landscape for a polyacetylene chain of 20 unit cells. The x-axis gives the location of the center of the particle within the chain, and the y-axis gives the energy required to create an effective particle centered at that position. The lower the energy, the easier it is to create an effective particle at that position.

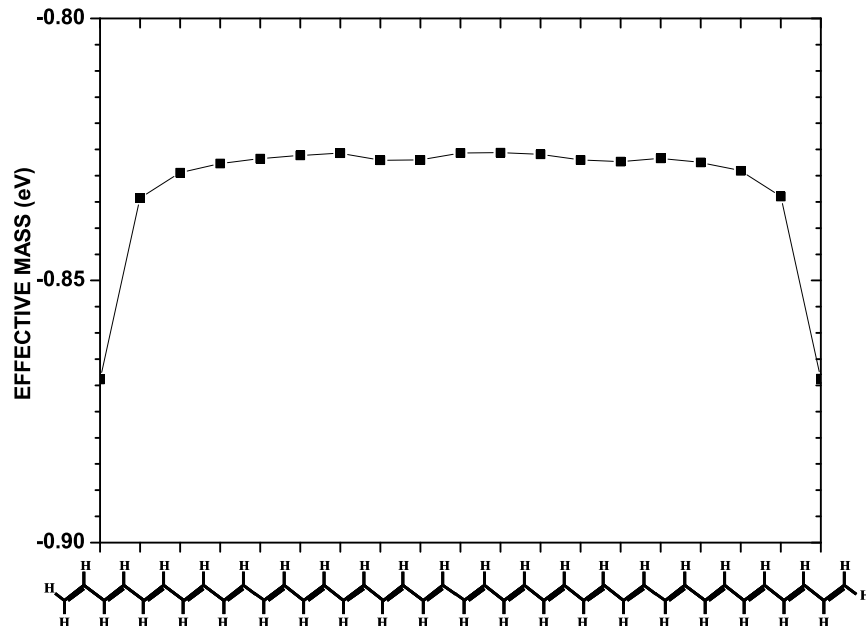


**Figure 4.4:** An effective mass landscape for a polyacetylene chain of 20 unit cells using INDO with the  $e_{cent}^-$  convention (see Fig. 4.3.1). Each point on the graph represents the transfer energy for the effective particle to move to an adjacent location in the molecule.

Fig. 4.3.1 shows that the effective particle, or exciton, prefers to be in the center of the chain. Other details about this energy landscape will be discussed later.

The delocalization energy can be determined by comparing the energy landscape with the state energy. The energies shown in the energy landscapes, such as in Fig. 4.3, represent the energy of a particle “frozen” on those sites. The difference between those energies and the corresponding CI excited state energy is then the delocalization energy. For the polyacetylene chain in Fig. 4.3, the delocalization energy is  $5.3 \text{ eV} - 2.7 \text{ eV} = 2.6 \text{ eV}$ .

### 4.3.2 Position-dependent Effective Masses

The off-diagonal Hamiltonian matrix elements between effective particles,

$$\beta_n^{(1)} = \langle \text{HF} | \Omega_{n+1} \hat{H} \Omega_n^\dagger | \text{HF} \rangle \quad (4.5)$$

specify the transfer amplitudes between segments, and thus determine the position-dependent effective mass of the particle. A larger magnitude indicates that it is easier to transfer the particle to the next segment, and thus that the effective mass is lighter. A position-dependent effective mass, or transfer amplitude, of zero means that there will be no transfer to the next segment, or that the particle has infinite mass. The effective mass landscapes give insight into the delocalization behavior of the effective particles. Fig. 4.4 is an example of the effective mass profile for a polyacetylene chain of 20 unit cells. This landscape shows that the transfer energy is relatively constant throughout the chain, but increases in absolute value at the ends. This increase in magnitude corresponds to a lowering of the effective mass and indicates that the particle moves faster towards the ends of the chain. (Note that the transfer matrix elements of Eq. 4.5 are less than zero, and so the magnitude *decreases* as you move up the y-axis of Fig. 4.4. This perspective is convenient since the effective mass then increases as you move up the y-axis and the landscape then corresponds to that of the effective mass.)

## 4.4 Results and Discussion

Most of the results presented in this Section show a comparison of the different center conventions for effective particles from Section 4.2.1. The results will also be given with and without the inclusion of the dielectric solvation described in Section 2.6. Unless indicated otherwise, all calculations were performed with the INDO Hamiltonian from Section 2.3.

### 4.4.1 Chain End Defects in Polyacetylene

This section examines the effects of the end of a chain on the effective particle in a polyacetylene oligomer with 20 unit cells. The energy and effective mass landscapes obtained with the PPP Hamiltonian are shown in Fig. 4.5 for all three conventions for the center of the effective particle, and both with and without inclusion of dielectric

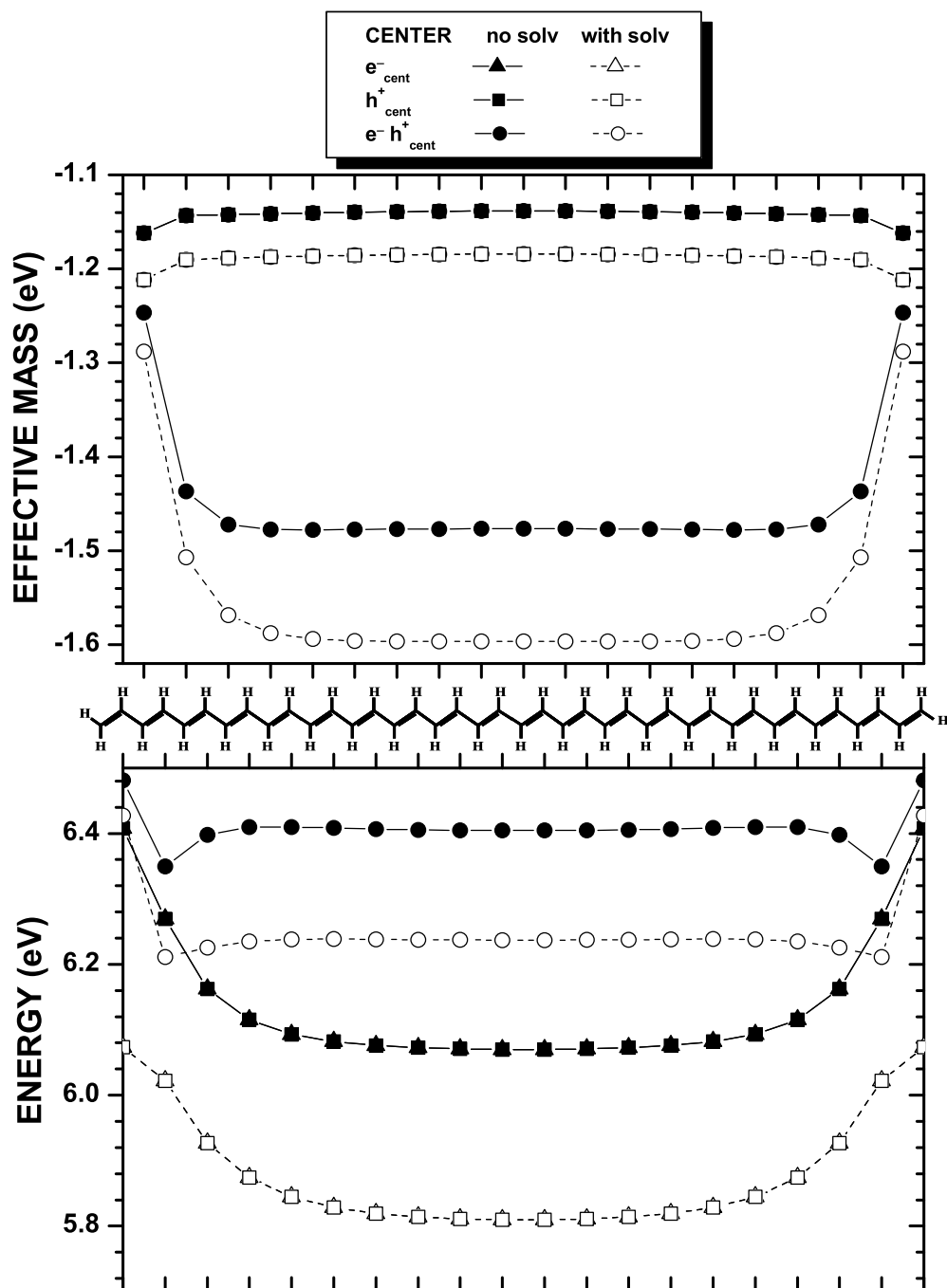


**Figure 4.5:** Energy landscapes and effective masses for 20 unit cells of polyacetylene with the PPP Hamiltonian both with (dotted lines) and without (solid lines) dielectric solvation included. The  $1^1B_u$  state energies obtained from the full S-CI calculations are 2.08 and 2.71 eV, respectively. Results are given for all effective particle center conventions.

solvation. Since the PPP Hamiltonian possesses particle-hole symmetry, the  $e_{cent}^-$  and  $h_{cent}^+$  conventions give identical results.

The energy landscapes obtained in the  $e_{cent}^-$  and  $h_{cent}^+$  are about 0.4 eV lower in energy than those obtained in the  $e^-h_{cent}^+$  convention. Since these conventions correspond to different analyses of the same wavefunction, this difference in energy for the stationary particles must be compensated by a corresponding change in the reduced masses. The  $e^-h_{cent}^+$  convention gives reduced masses that are about 20 to 30% lighter than those from the  $e_{cent}^-$  and  $h_{cent}^+$  conventions. This leads to a greater delocalization energy in the  $e^-h_{cent}^+$  convention that compensates for the higher energy landscape. The conventions also differ with regards to the effects of the chain end. In the  $e_{cent}^-$  and  $h_{cent}^+$  conventions, the chain end primarily alters the energy landscape: the energy rises by 0.34 eV at the end of the chain, while the reduced mass changes by only 0.02 eV. In the  $e^-h_{cent}^+$  convention, the chain end primarily alters the reduced mass: the energy oscillates by about 0.1 eV while the reduced mass gets heavier by 0.25 eV.

Dielectric interactions with the surroundings lower the  $1^1B_u$  state energy from 2.71 eV to 2.08 eV, corresponding to a dielectric stabilization energy of 0.63 eV. Fig. 4.5 shows that part of this stabilization arises from a lowering of the energy of the stationary effective particle, such that the energy landscapes drop by about 0.25 eV for the  $e_{cent}^-$  and  $h_{cent}^+$  conventions and 0.18 eV for the  $e^-h_{cent}^+$  convention. The remainder of the stabilization energy arises from a change in reduced mass such that the particle becomes lighter, or more strongly delocalized, in the dielectric.

In the  $e_{cent}^-$  and  $h_{cent}^+$  conventions, the energy rises as the effective particle approaches the end of the chain while the reduced mass stays relatively constant. In considering the effects of this energy rise on the particle, it is useful to consider the delocalization energy of the particle. The delocalization energy is the difference between the energy of the stationary effective particle, as given by the energy landscape, and the energy of the  $1^1B_u$  state, about 3.5 eV for this system. For all of the landscapes in Fig. 4.5, the rise in energy at the end of the chain is under 0.3 eV, less than 10% of the delocalization energy. This rationalizes the success of particle-in-a-box models for polyenes,<sup>83</sup> since these models treat the chain end as a hard-wall

potential.

Other details of these landscapes (including the end effects obtained with the INDO Hamiltonian) will be discussed in Section 4.4.4.

#### 4.4.2 Chain End Effects in PPV

Figures 4.6 and 4.7 show the energy landscapes for oligomers of PPV with 12 phenyl rings. The unit cell of PPV contains a phenyl ring and a vinyl group (see Fig. 1.3); however, most studies on oligomers use structures that are capped with a phenyl group. Figures 4.6 and 4.7 show landscapes for both types of termination. As expected, the differences occur primarily on the terminating group, with the phenyl cap having an energy that is 0.5-0.7 eV higher than that obtained for termination with a PPV unit cell. This energy difference is due to the smaller size of the phenyl cap relative to the PPV unit cell, which contains both a phenyl group and a vinylene group. However, the effective mass landscape remains about the same, indicating that the Hamiltonian coupling matrix element between the cap and the remainder of the oligomer is roughly the same for both caps. The  $1^1B_u$  state energy obtained from full S-CI calculations varies by less than 0.05 eV, indicating that the addition of a vinyl group has little effect on an oligomer of this length.

Other aspects of these energy and effective mass landscapes are discussed in Section 4.4.4.

#### 4.4.3 Chain Length Effects

The energy landscapes of various length oligomers of polyacetylene are shown in the bottom panel of Figure 4.8, both with and without inclusion of dielectric solvation. The corresponding  $1^1B_u$  state energies are given in Table 4.1. For isolated oligomers, the energy landscapes follow a smooth dependence on chain length after about 6 units cells, such that the energy landscape for the oligomer could be easily predicted from that of the long chain. For oligomers with 2 and 4 unit cells, the landscapes are considerably higher than those of longer oligomers. This can be rationalized in terms of these short oligomers being comparable in size to the effective particle. When dielectric

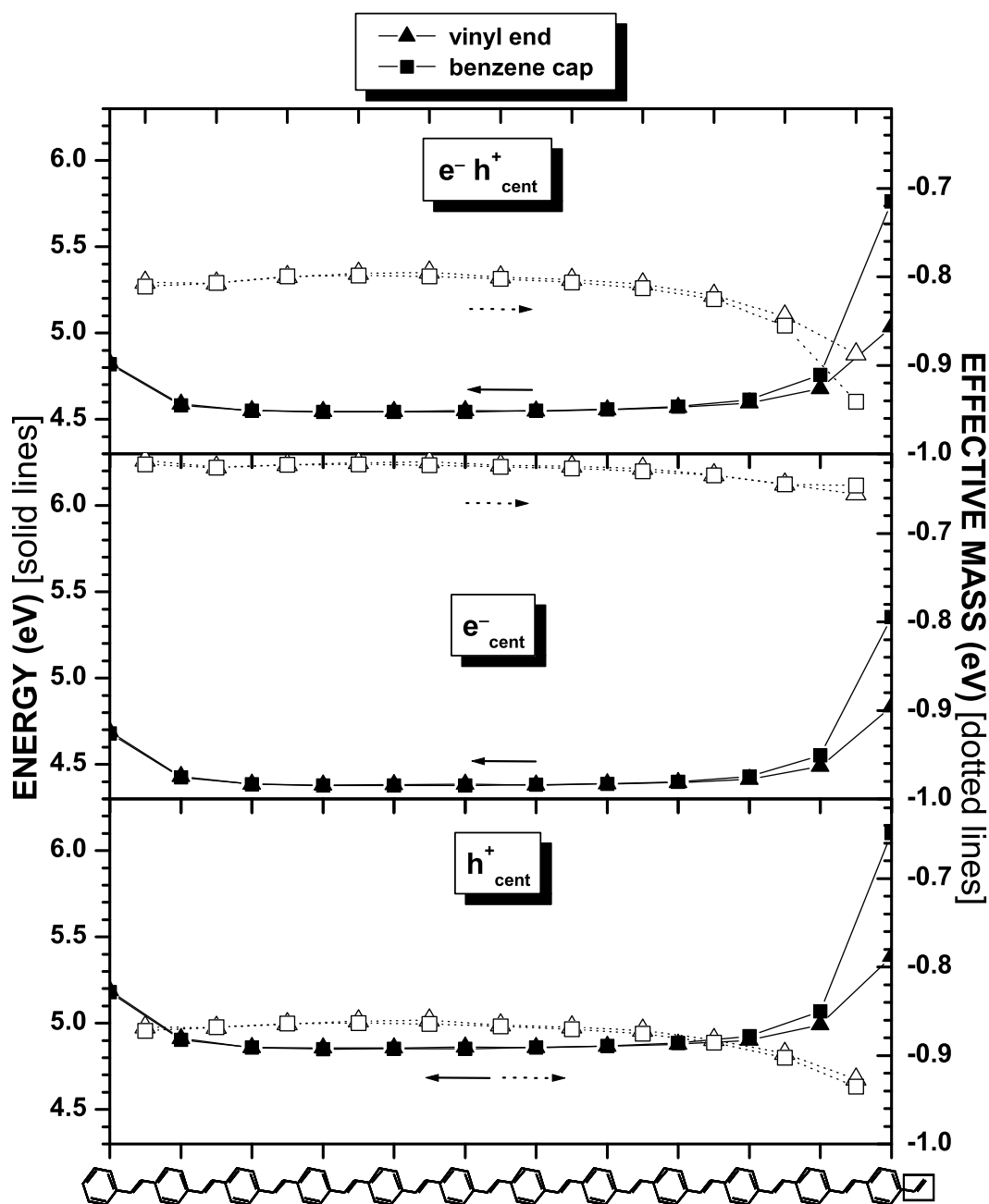


**Figure 4.6:** Energy (solid lines) and effective mass (dotted lines) landscapes for 12 unit cells of PPV with different groups at the end of the chain and for different effective particle center conventions. The  $1^1B_u$  state energy obtained from the full S-CI calculation for both structures is 3.00 eV. The INDO Hamiltonian was used. No dielectric solvation is included.

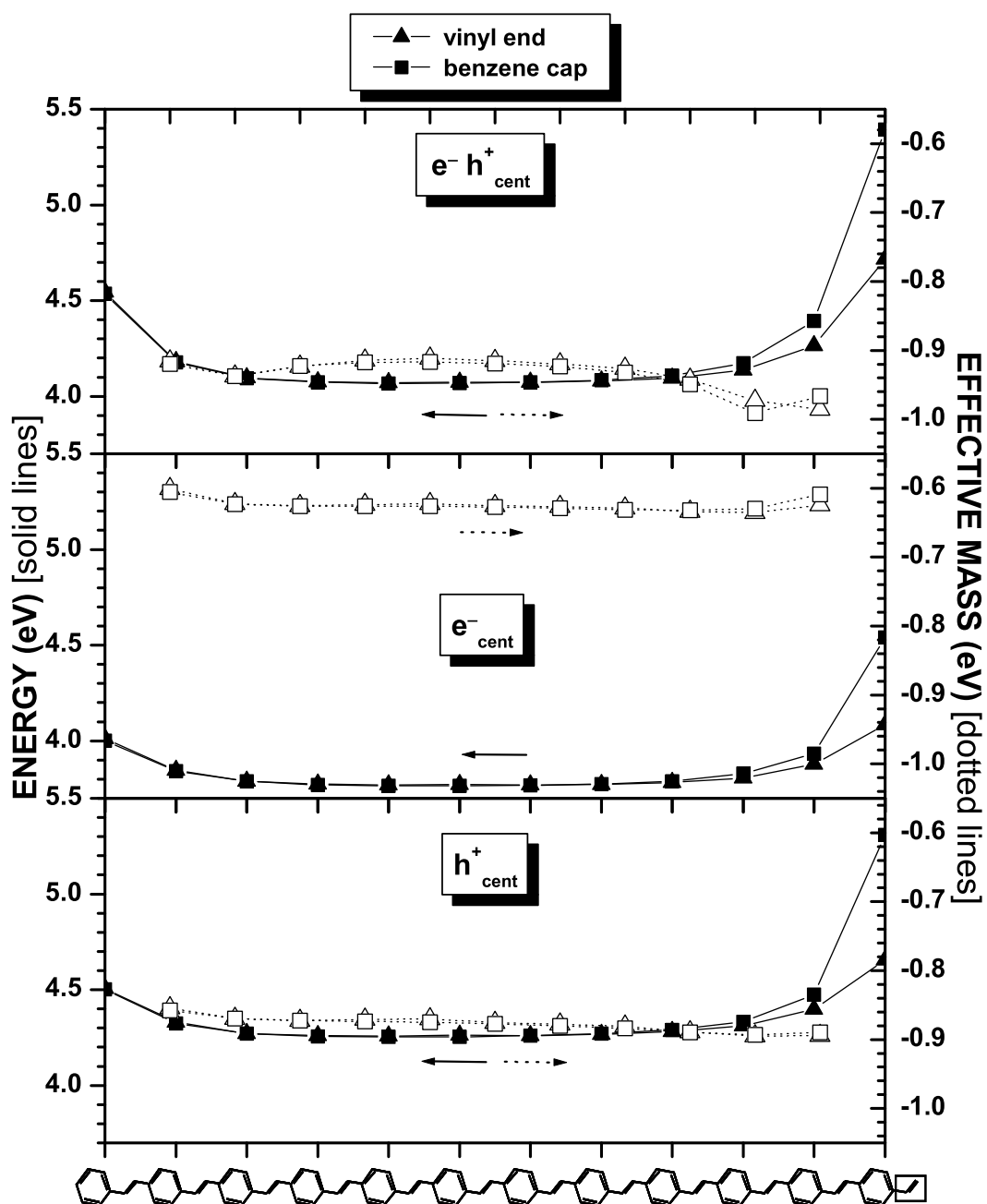


*Figure 4.7:* Same as Figure 4.6, but with dielectric solvation included. The  $1^1B_u$  state energy obtained from the full S-CI calculation for both structures is 2.39 eV.

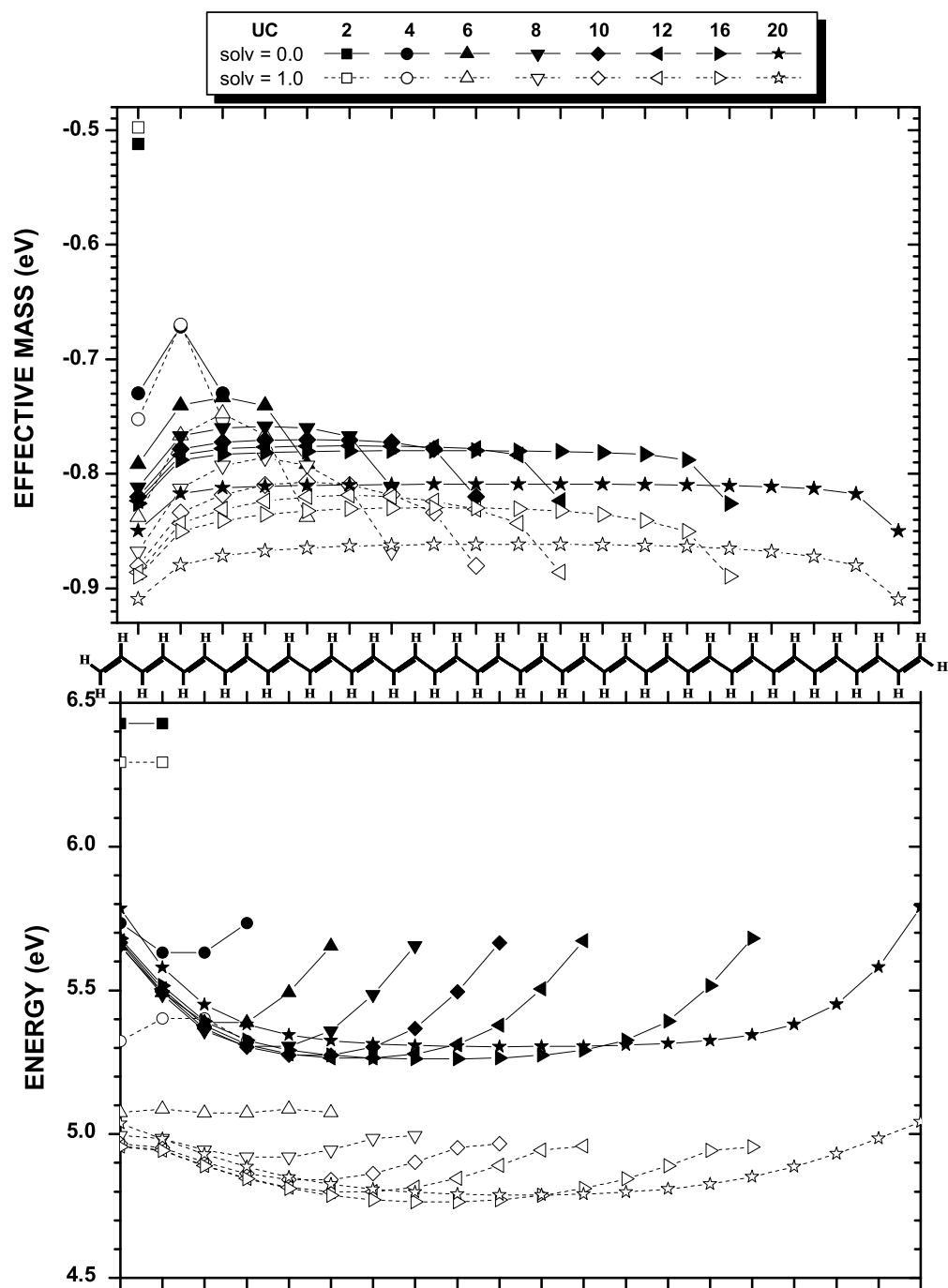


**Figure 4.8:** Energy landscapes (bottom) and effective masses (top) for polyacetylene with different chain lengths. The INDO Hamiltonian was used. The effective particles are  $e_{cent}^-$ ; the results are comparable for the other types of effective particle center conventions. The results are given without (solid lines) and with (dotted lines) dielectric solvation included. The  $1^1B_u$  state energies obtained from the full S-CI calculations are given in Table 4.1.

**Table 4.1:** The  $1^1B_u$  state energies (in eV) obtained from a full S-CI calculation for polyacetylene and PPV chains of various lengths in Figures 4.8 and 4.9.

		<b>N=2</b>	<b>N=4</b>	<b>N=6</b>	<b>N=8</b>	<b>N=10</b>	<b>N=12</b>	<b>N=16</b>	<b>N=20</b>
<b>polyacetylene</b>	solv = 0.00	5.92	4.28	3.64	3.32	3.13	3.02	2.88	2.77
	solv = 1.00	5.84	3.98	3.22	2.83	2.60	2.46	2.31	2.18
<b>PPV</b>	solv = 0.00	4.10	3.33	3.14	3.06	3.02	2.99		
	solv = 1.25	3.81	2.85	2.62	2.54	2.49	2.47		

solvation is included, the landscapes converge more slowly. Dielectric stabilization is much greater for configurations with large electron-hole pair separations, and this apparently leads to a somewhat slower convergence with respect to oligomer length.

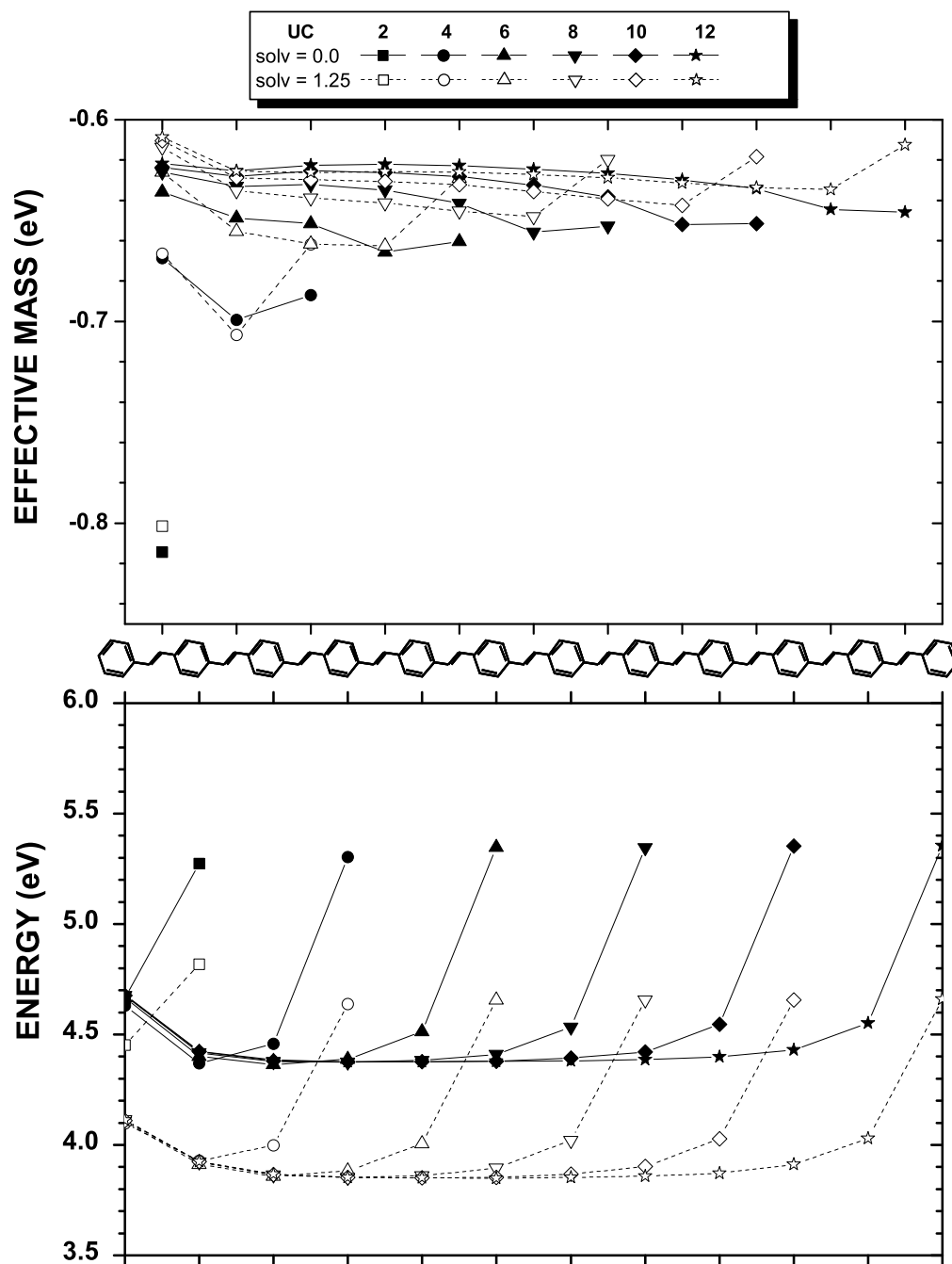
The effective mass landscapes for these oligomers are also shown in the top of Figure 4.8. For short oligomers, the effective mass is somewhat heavier than that predicted from long chains. Without dielectric solvation, the effective mass landscape converges onto that of the long chain by about 10 unit cells. With dielectric solvation, the convergence is a bit slower, and agrees with the long chain by about 16 unit cells.

Figure 4.9 shows the energy and effective mass landscapes for PPV. Unlike polyacetylene, the energy landscapes for all oligomers agree with those expected from the long-chain limit. This is the case both with and without inclusion of dielectric solvation. The effective mass does, however, become heavier as the oligomer increases in length, changing from -0.8 eV to -0.7 eV between 2 and 3 unit cells, and then slowly approaching the long chain limit of -0.62 eV.

#### 4.4.4 PPP vs INDO Hamiltonian for Polyacetylene

Section 2.3 describes the Hamiltonians most commonly used to study  $\pi$  electron systems. This section compares the energy and effective mass landscapes obtained from the PPP and INDO models of polyacetylene.

The energy landscapes, obtained without inclusion of dielectric solvation, are shown in Fig. 4.10. As explained in Section 2.4.2, the PPP Hamiltonian conserves electron-hole symmetry while INDO does not. As described in Section 2.4.2, the bandwidth is larger for the valence than conduction bands<sup>69,70</sup> in INDO theory of conjugated polymers. Since the band width is larger for the valence than conduction



**Figure 4.9:** Energy landscapes (bottom) and effective masses (top) for PPV with different chain lengths. The INDO Hamiltonian was used. The effective particles are  $e_{cent}^-$ ; the results are comparable for the other types of effective particle center conventions. The results are given without (solid lines) and with (dotted lines) dielectric solvation included. The  $1^1B_u$  state energies obtained from the full S-CI calculations are given in Table 4.1.

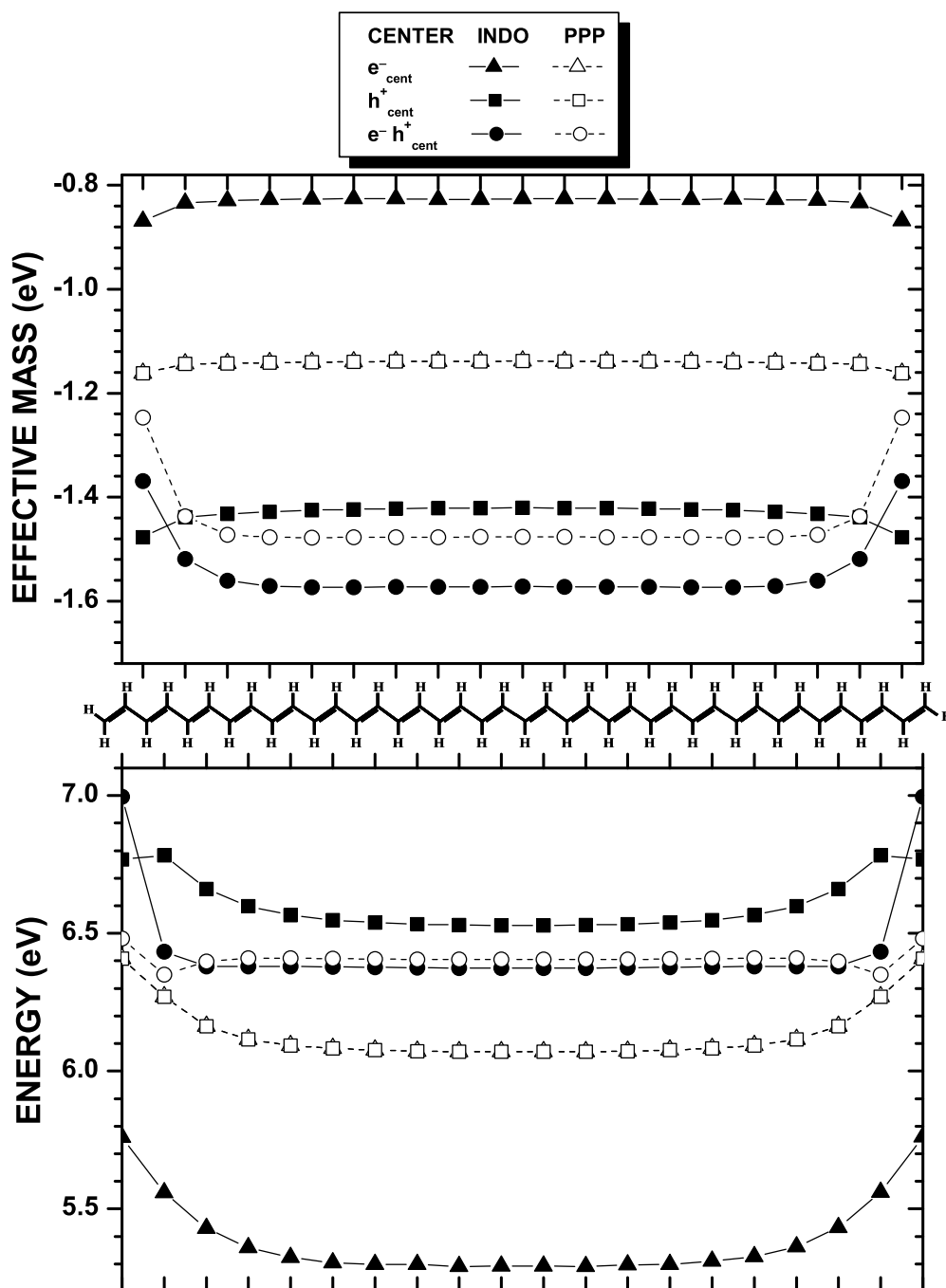


*Figure 4.10:* Energy and effective mass landscapes for 20 unit cells of polyacetylene using both the PPP (dotted lines) and INDO (solid lines) Hamiltonians and for different effective particle center conventions. The  $1^1B_u$  state energies obtained from the full S-CI calculations are 2.67 and 2.71 eV, respectively. The PPP curves are the same as those given in Figure 4.5. Dielectric solvation is not included.

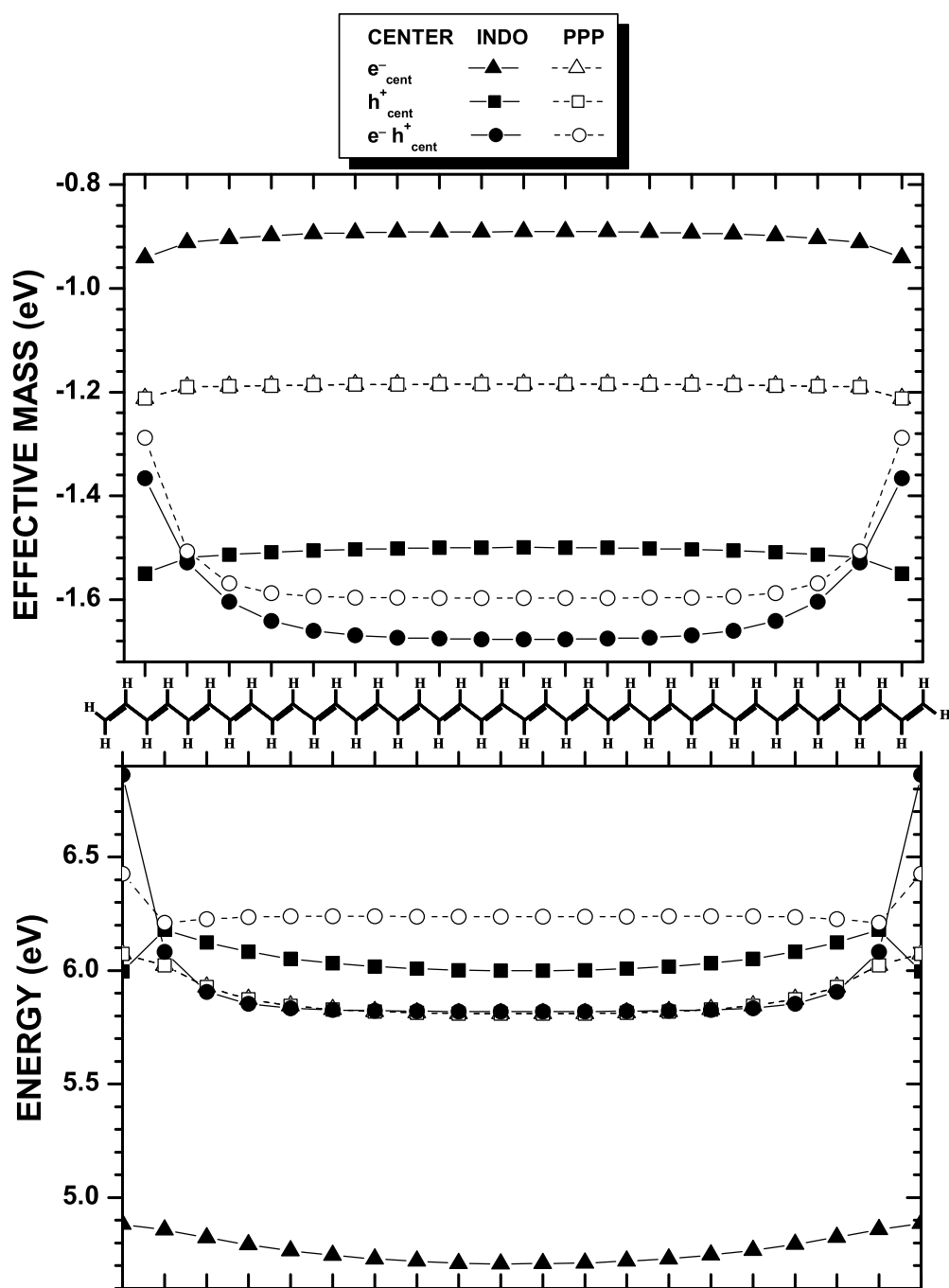


*Figure 4.11:* Same as Figure 4.10, but with dielectric solvation included. The  $1^1B_u$  state energies obtained from the full S-CI calculations are 2.32 for PPP and 2.08 eV for INDO.

band, the hole is lighter than the electron and the  $h_{cent}^+$  convention should give a lighter reduced mass than the  $e_{cent}^-$  convention. This is observed in Fig. 4.10, where the reduced mass for the  $e_{cent}^-$  convention is about 1.7 times larger than that for the  $h_{cent}^+$  convention. The reduced mass landscape for the PPP Hamiltonian lies approximately half way between the INDO landscapes. This suggests that when a model that possesses particle-hole symmetry, such as the PPP model, is parameterized to experiment, the effective mass of the particles is comparable to the average of the actual effective masses of the electron and hole. Since the  $h_{cent}^+$  convention leads to a lighter effective mass than the  $e_{cent}^-$  convention, it leads to a larger delocalization energy and the energy landscape is expected to lie above that from the  $e_{cent}^-$  convention. This is indeed the case in Fig. 4.10. The delocalization energies obtained from these energy landscapes are 3.73 and 2.46 eV for the  $h_{cent}^+$  and  $e_{cent}^-$  conventions, respectively. Similar results are obtained in Figure 4.11 with dielectric solvation included.

The  $e_{cent}^-$  and  $h_{cent}^+$  conventions also lead to somewhat different energy landscapes near the end of the chain. For the  $e_{cent}^-$  convention, the INDO landscape is similar to that from PPP theory, with the energy rising smoothly as the particle approaches the end of the chain. For the  $h_{cent}^+$  convention, the energy also rises as the particle approaches the chain end, but it then decreases on the last unit cell. This decrease in energy on the last unit cell is larger in a dielectric than it is for the bare chain. It is not clear what is causing this behavior.

Since the  $e^-h_{cent}^+$  convention preserves electron-hole symmetry, the INDO and PPP Hamiltonians are expected to yield similar landscapes within this convention. Figures 4.10 and 4.11 do show similar behaviors, although there are some differences between the results obtained with the two Hamiltonians. Although the effective mass landscapes behave similarly at the end of the chain, the energy rises much more sharply in the INDO landscape than in the PPP landscape. The effective mass is also somewhat lighter for INDO theory than PPP theory. Finally, the dielectric effects on the energy landscape are 0.5 eV larger for INDO theory than PPP theory, which is reflected in the  $1^1B_u$  state energies. The  $1^1B_u$  state energies from the PPP and INDO models are 2.67 and 2.71 eV, respectively, for the bare chains and 2.32 and 2.08 eV, respectively, when dielectric solvation is included. All of these differences

can be attributed to the larger average electron-hole separation obtained from INDO theory, as discussed in Section 2.4.2. According to Fig. 2.2, the most probable location of an electron and hole relative to one another is on the same site for the PPP model, but on adjacent sites in the INDO model. This larger separation between the electron and hole in INDO theory is consistent with the pronounced chain-end effects, lighter effective mass, and larger dielectric stabilization energies from INDO.

The remainder of the energy and effective mass landscapes presented in this work are calculated using the INDO Hamiltonian and, unless otherwise noted, the CI calculations include only the  $\pi$  molecular orbitals.

#### 4.4.5 Test of the Separation of the Form of the Effective Particle and Its Dynamics

##### Polyacetylene

This section compares the form of the effective particles obtained from the two methods discussed in Section 4.2.2. The square symbols of Figures 4.12 and 4.13 were obtained by decomposing the full S-CI wavefunction into the form of Eq. 4.2. Since the effective particle is extracted from the full wavefunction, this procedure yields the form of the “effective particle in motion,” or the form of the effective particle as it undergoes delocalization dynamics. The triangle symbols of Figures 4.12 and 4.13 were obtained by using Eq. 4.3 to determine the form of the effective particle on each unit cell. This procedure yields the form of the “frozen effective particle”, or the form the effective particle adopts when its center is constrained to a particular molecular segment. The resulting forms for the particles were then used to evaluate the energy and effective mass matrix elements of Eqs. 4.4 and 4.5.

For the  $e_{cent}^-$  and  $h_{cent}^+$  conventions in Fig. 4.12, the energy landscapes obtained for the “effective particle in motion” and “frozen effective particle” agree to within about 0.09 eV. This is excellent agreement compared to, for instance, the delocalization energy of 2.4 eV for the  $e_{cent}^-$  and 3.4 eV for the  $h_{cent}^+$  conventions. Also, the effective mass landscapes only differ by 5.1% and 9.1% respectively. Inclusion of dielectric

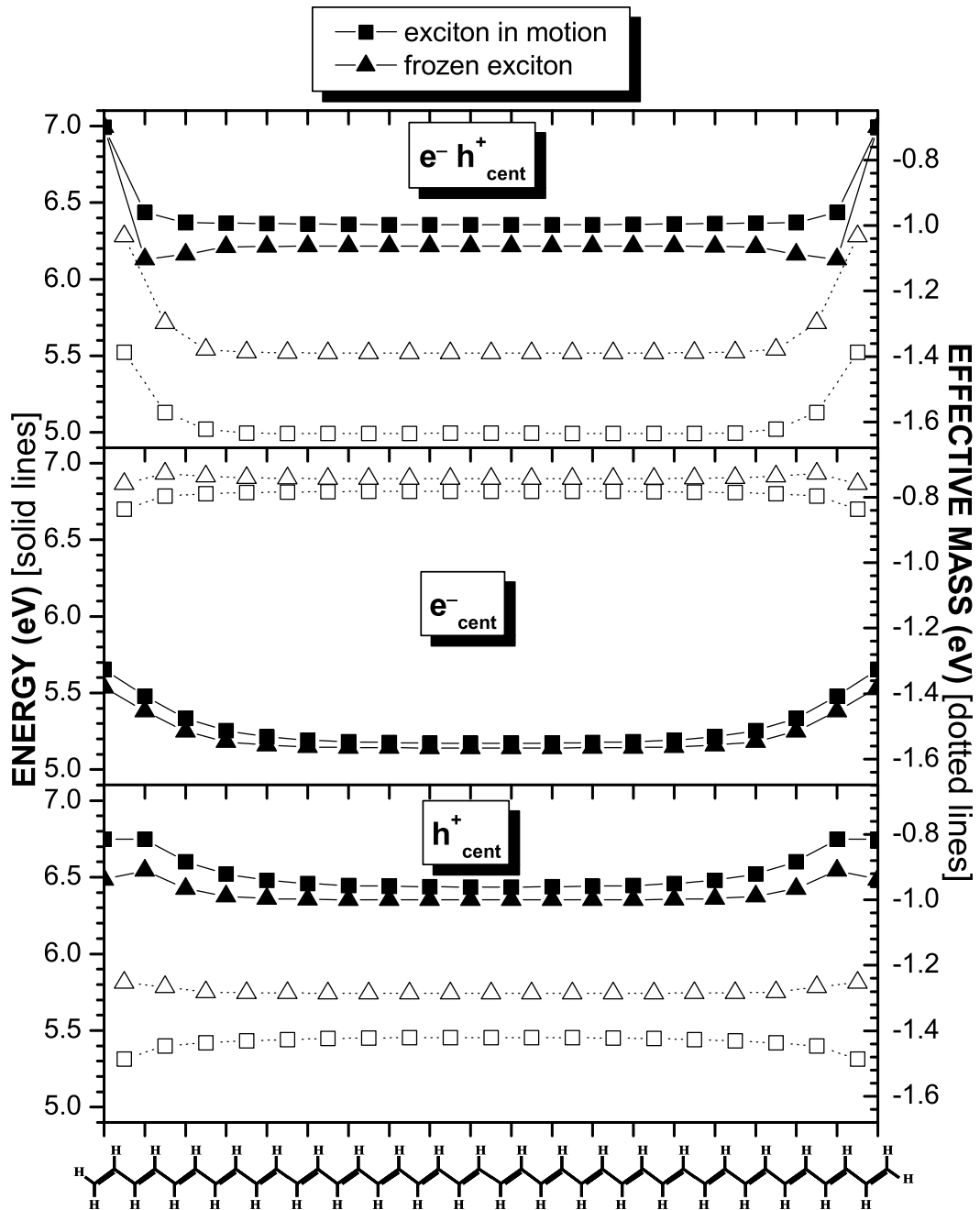


**Figure 4.12:** Energy (solid lines) and effective mass (dotted lines) landscapes for 20 unit cells of polyacetylene for different particle center conventions using the INDO Hamiltonian. The form of the effective particles was calculated in two ways, as depicted in Fig. 4.2. The first method includes the effects of the delocalization dynamics (square symbols), and the second method has the dynamics turned off (triangle symbols). No dielectric solvation is included. The  $1^1B_u$  state energy obtained from the full S-CI calculations is 2.71 eV and the  $1^1B_u$  state energies obtained from the frozen calculations are 3.18, 2.77, and 2.94 eV for the  $e^-h_{cent}^+$ ,  $e_{cent}^-$ , and  $h_{cent}^+$  effective particles, respectively. The square symbol curves are the same as those given in Figure 4.10.

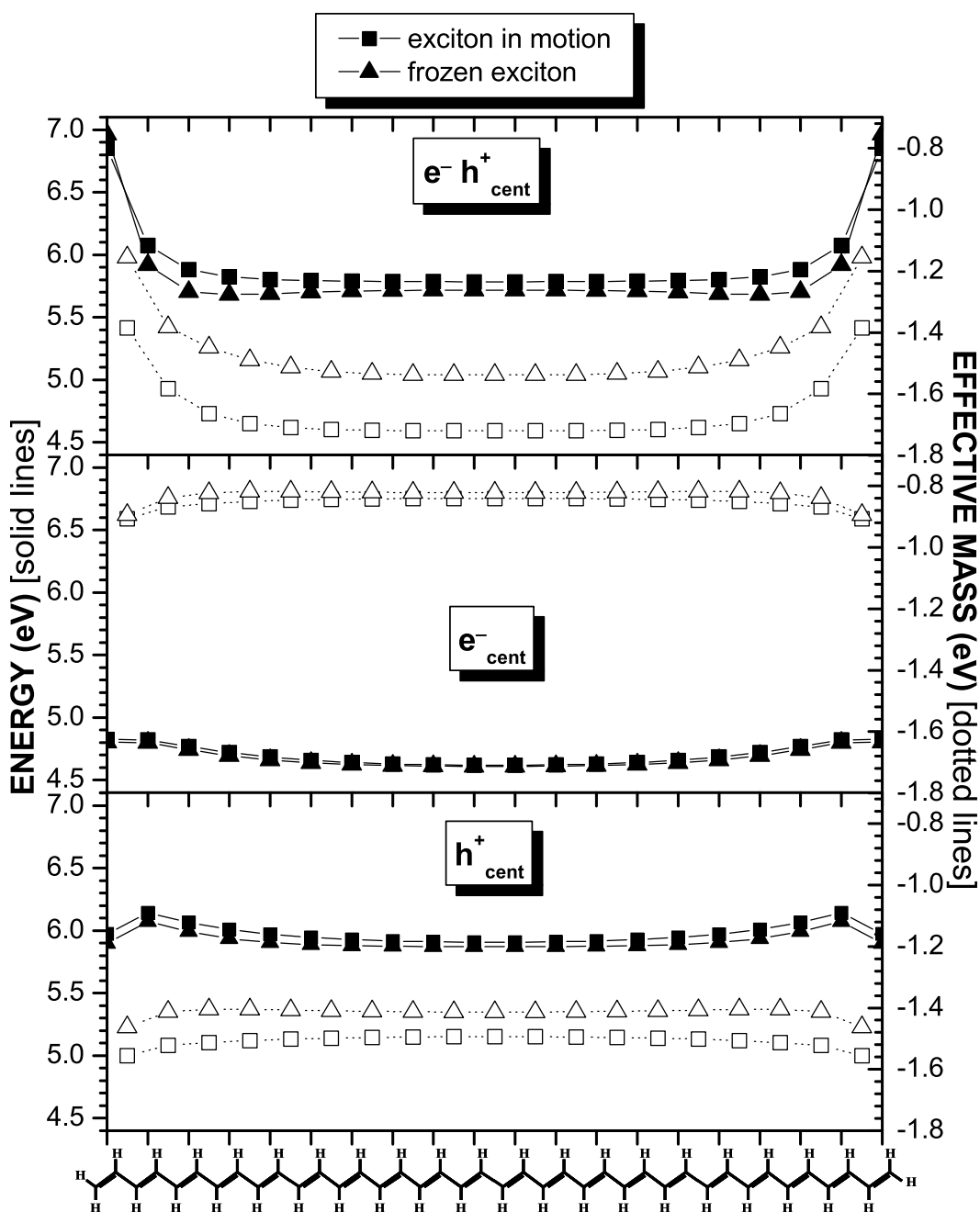


**Figure 4.13:** Same as Figure 4.12, but with dielectric solvation included. The  $1^1B_u$  state energy obtained from the full S-CI calculations is 2.08 eV and the  $1^1B_u$  state energies obtained from the frozen calculations are 2.52, 2.20, and 2.10 eV for the  $e^-h_{cent}^+$ ,  $e_{cent}^-$ , and  $h_{cent}^+$  effective particles, respectively. The square symbol curves are the same as those given in Figure 4.11.

solvation in Fig. 4.13 yields somewhat better agreement between the “effective particle in motion” and “frozen effective particle” landscapes. Therefore, although dynamics has a significant effect on the state energy, it has a relatively minor effect on the form of the  $e_{cent}^-$  and  $h_{cent}^+$  effective particles themselves. These results strongly suggest that it is possible to separate the form of the effective particles from their dynamics. Section 4.2.3 argued that computational savings of a factor of 400 could be obtained by first determining the form the effective particle adopts when it is centered on each unit cell, and then solving for the dynamics of this particle. The use of this procedure on the unsolvated systems yields 2.77 and 2.94 eV for the  $1^1B_u$  state energy within the  $e_{cent}^-$  and  $h_{cent}^+$  effective particles, respectively. This is in quite good agreement with the state energy of 2.71 eV obtained from a full S-CI calculation. For this case, the computational savings come with little loss in accuracy.

However, for the  $e^-h_{cent}^+$  convention in Figs. 4.12 and 4.13, the agreement between the “effective particle in motion” and “frozen effective particle” landscapes is not quite as good as for the other conventions. While the energy landscape values only differ by about 0.06-0.13 eV, the effective mass landscape values vary by 14.7-18.0%. The procedure of Section 4.2.3 that leads to computational savings of a factor of 400 introduces substantially more error for the  $e^-h_{cent}^+$  convention than for the  $e_{cent}^-$  or  $h_{cent}^+$  conventions considered above. For the  $e_{cent}^-$  convention, the  $1^1B_u$  state energy obtained with the computationally cheaper method is 3.18 eV, without dielectric solvation and 2.54 eV with dielectric solvation. These are to be compared to the full S-CI results of 2.71 eV. and 2.08 eV respectively.

Similar results for the energy and effective mass landscapes are obtained with the PPP Hamiltonian, given in Figures 4.14 and 4.15.

## PPV

Although calculations similar to those of the previous section may be possible on other molecular systems, such as PPV, the frozen effective particle calculations become more complex and have not yet been implemented. In solid state physics terminology, polyacetylene only has one  $\pi$  valence and one  $\pi^*$  conduction band, while

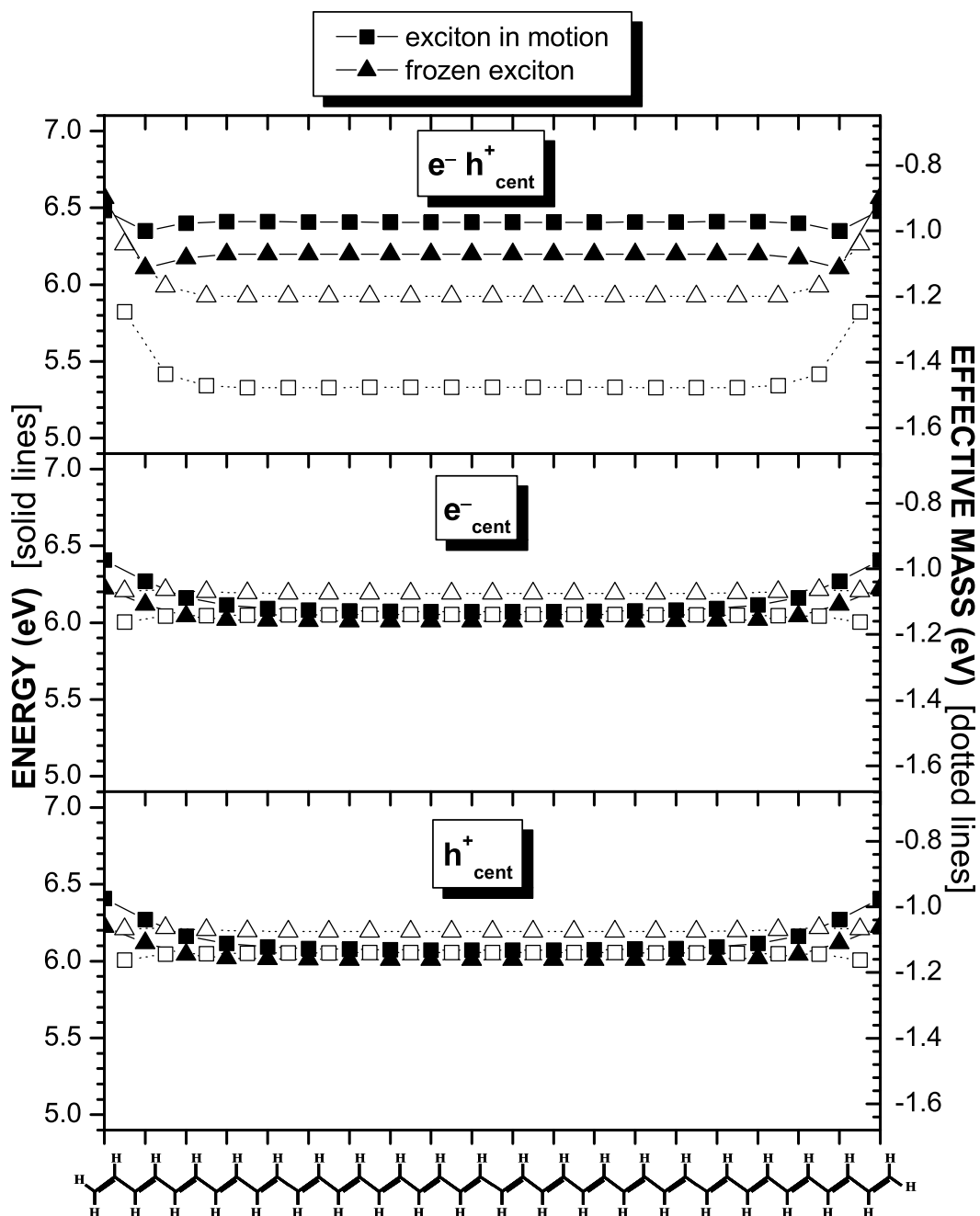


Figure 4.14: Same as Figure 4.12, but with the PPP Hamiltonian.

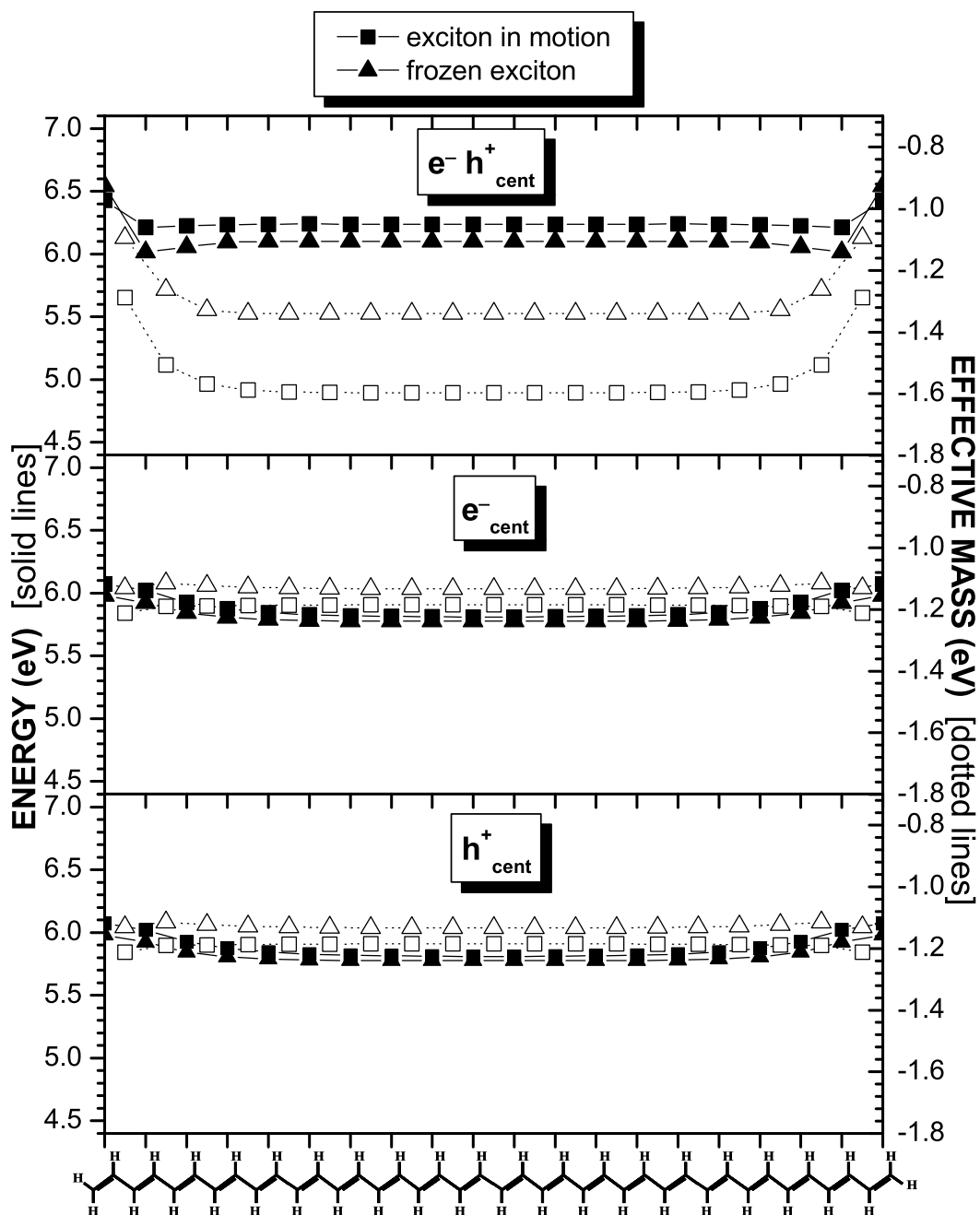


Figure 4.15: Same as Figure 4.13, but with the PPP Hamiltonian.

PPV has four  $\pi$  valence and bands and four  $\pi^*$  conduction bands. (The total number of  $\pi$  bands is equal to the number of  $sp^2$  hybridized carbons per unit cell.) While the form of the electrons and holes in polyacetylene are set by symmetry, the form of the electrons and holes in PPV are influenced by the coupling between unit cells. For instance, in the limit of decoupled phenyl rings, the highest valence and lowest conduction bands of PPV become degenerate with the localized (flat) bands of PPV.<sup>69,70</sup> Use of the “frozen particle” approach described above, especially in the  $e_{cent}^-$  or  $h_{cent}^+$  conventions, freezes not only the effective particle but also the electron or hole. This leads to an incorrect description of the electron or hole; in particular, it uses the electron or hole corresponding to the flat bands of PPV. It should be relatively straightforward to modify the above model such that the form used for the electron or hole corresponds to the electron or hole “in motion,” and this modification will not significantly impact the predicted computational savings. However, this is left for the subject of future studies.

## 4.5 Conclusion

A method was developed that can extract the contributions of select molecular structure components from excited state calculations. This approach describes an excitation as an effective particle by grouping CI electron-hole configurations that are centered about a particular unit cell into a single contracted function. The center of these localized effective particles can be defined according to position of the electron, position of the hole, or the average position of the electron and hole.

The form of the effective particles can be determined in two ways. The first method extracts the form from a full CI calculation, which gives the form of the particle while it is in motion. The second method constructs effective particles “frozen” on a particular segment. The difference between these two methods is that the former method includes the effects of the dynamics in the form of the particle, whereas the latter does not. A comparison of these two methods reveals the extent to which the form of the effective particles depends on the dynamics. For polyacetylene, the

form and the dynamics can be separated with little loss of accuracy, which can yield substantial computational savings.

The interpretive advantages of using the effective particle approach with electronic structure calculations were also demonstrated. The effective particle approach yields useful information on the nature of the excited states, such as the energy landscape and effective mass of the excitation. A variety of details about this effective particle approach and the information gained from the energy and effective mass landscapes were explored, such as chain length effects, chain-end defects, inclusion of dielectric solvation, and Hamiltonian differences. Further applications are the subject of the remainder of this thesis.

## 4.6 Appendix

This appendix shows how the energy and effective mass landscapes are calculated for  $e^-h_{cent}^+$  effective particles. The energy landscape and position-dependent effective mass values are stored as matrix  $\mathbf{M}$  during the calculations, where elements  $M_{ii}$  represent the energy landscape values according to Eq. 4.4, and the elements  $M_{ij}$  correspond to the transfer energy between segment  $i$  and  $j$  of Eq. 4.5. The overlap of the effective particles is also calculated and stored in a matrix,  $\mathbf{S}$ .

Since the energy values stored in  $\mathbf{M}$  were calculated using non-orthogonal particles,  $\mathbf{M}$  must be transformed. This transformation is done via the inverse square root of the overlap matrix, which is Löwdin symmetric orthogonalization<sup>117</sup> (see Eq. 3.2),

$$\mathbf{M}' = \mathbf{S}^{-1/2}\mathbf{M}(\mathbf{S}^{-1/2})^T. \quad (4.6)$$

The mathematical procedure to find the inverse square root of a matrix (or in general, apply any function to a matrix), is as follows:<sup>78</sup>

1. Diagonalize  $\mathbf{S}$  to form  $\mathbf{s}$ .
2. Take the inverse square root of each of the eigenvalues to form  $\mathbf{s}^{-1/2}$ .

3. “Undiagonalize”  $\mathbf{s}^{-1/2}$  by performing a unitary transformation using the eigenfunctions obtained from the diagonalization in Step 1.

The diagonal elements of  $\mathbf{M}'$  give the energy landscape, and the off-diagonal elements give the effective masses.

# Chapter 5

## Application to Chemical Defects

### 5.1 Introduction

Chemical defects in conjugated polymers have a strong impact on the photophysics of these materials. For instance, a *meta*-linkage defect in poly-(*p*-phenylenevinylene) (PPV) can increase the photoluminescence quantum efficiencies by interfering with the  $\pi$  delocalization, which alters the effective conjugation length. Synthetic chemists have utilized the benefits of *meta*-linkages by intentionally incorporating these defects into the polymers either as a copolymer unit or randomly.<sup>73–75</sup> Other chemical defects, such as *cis*-linkages,<sup>120</sup> and nonconjugated spacer units have been used to control the effective conjugation length and hence exciton confinement.<sup>121</sup>

Some chemical defects decrease quantum efficiencies. For instance, the quenching of luminescence in some PPV samples has been attributed to carbonyl defects.<sup>18–25</sup> Carbonyl defects occur in conjugated polymers through photooxidation and degradation of the material.<sup>19</sup> Experimental analysis of these structures have found that the oxygen attacks the vinylene bonds in PPV, to create two chains terminated with an aldehyde group.<sup>19</sup> Rothberg has suggested that the fluorescence is quenched due to electron-withdrawing character of the carbonyl oxygen, which leads to dissociation of the exciton on the carbonyl group.<sup>19</sup>

Although quantum chemistry is a useful tool for understanding the photophysics of conjugated polymers, it is difficult to elucidate from traditional calculations how

the structure of the molecular system, and the inclusion of chemical defects, affects its properties. With the effective particle method described in Chapter 4, such insight can be gained. The effective particle approach yields information about how defined components of the system, such as functional groups or monomer units, contribute to the electronic excitations. This approach describes an excitation as an effective particle that moves on some energy landscape, and that possesses a position-dependent effective mass. The effects of the molecular structure on the excited state properties can be determined by examining these landscapes.

This chapter utilizes the energy landscapes and position-dependent effective masses obtained from the effective particle approach to investigate how chemical defects affect the photophysics of conjugated polymers. Polyacetylene is studied as a model system for  $\pi$ -conjugated polymers. Results are also presented for a luminescent polymer, PPV. These results show how the carbonyl acts as an electron-withdrawing group, and that the charge separation of a disassociating exciton is stabilized by the inclusion of fast dielectric screening effects. These results also show how a *meta*-linkage defect serves to break conjugation in a 12-ring oligomer of PPV.

## 5.2 Methodology

This chapter examines the effects of a carbonyl defect on a 20 unit cell oligomer of polyacetylene and a 12 unit cell oligomer of PPV. The ground state geometries of these polymers, whose unit cell structures are depicted in Figure 1.3, were optimized with the implementation of the PM3 Hamiltonian<sup>122</sup> in MOPAC, with no geometric constraints. For the carbonyl defect structures, the aldehyde group was placed on the last unit cell in order to match experimental structural characterizations of the defects.<sup>19</sup> A PPV oligomer with a vinyl end group is used (refer to Section 4.4.2) for comparative purposes. The optimized geometries indicate that the carbonyl lies in the same plane as the polymer backbone for both polyacetylene and PPV.

The excited electronic states were obtained using S-CI theory and the INDO Hamiltonian (see Sections 2.3.3 and 2.2). Localized molecular orbitals were obtained using the method described in Chapter 3, with the molecular segments defined ac-

ording to unit cells. Singles Configuration Interaction (S-CI) theory (Section 2.4) was used to calculate the excited electronic states. Only the  $\pi$  and nonbonding molecular orbitals were included in the S-CI calculations, and no limit on the number of electron hole configurations,  $m_{e-h}$ , was utilized. The calculation of the two electron integrals was limited to  $\Delta \leq 4$  for the PPV calculations (Section 3.3.2). Calculations were also performed with the inclusion of the fast dielectric screening of the electron and hole (Section 2.6), which simulates the effects of interchain interactions on the electronic excited states. The solvation model was scaled by 1.25 for meta-linkage PPV in order to obtain a  $1^1B_u$  state energy of 2.5 eV, which is comparable to experimental observations, and was scaled by 1.75 eV for the carbonyl calculations. The effective particle approach described in Chapter 4 was utilized to derive energy and effective mass landscapes. All three conventions for the center of effective particle were used.

## 5.3 Results and Discussion

### 5.3.1 Polyacetylene with Carbonyl Defect

A polyacetylene oligomer with 20 unit cells and a terminal aldehyde group was used as a general model of  $\pi$ -conjugated polymers in order to investigate how a carbonyl defect affects the photophysics. Figure 5.1 compares the S-CI excited state energy levels and their corresponding transition moments from the  $1^1A_g$  ground state; the solid lines represent the excited state energies for a regular polyacetylene chain, and the dotted lines are for the polymer terminating with an aldehyde group. (As described in Section 1.1.1, the  $1^1B_u$  state is defined as the excited state that has the largest transition moment from the ground state.) For the unsolvated calculations, the energies and transition moments change very little with the inclusion of the carbonyl. Inclusion of dielectric solvation leads to an overall drop in energy for all of the excited states. In addition, effects of the carbonyl on the excited state energies is slightly larger than then seen without solvation, but the difference is negligible for the  $1^1B_u$  state.

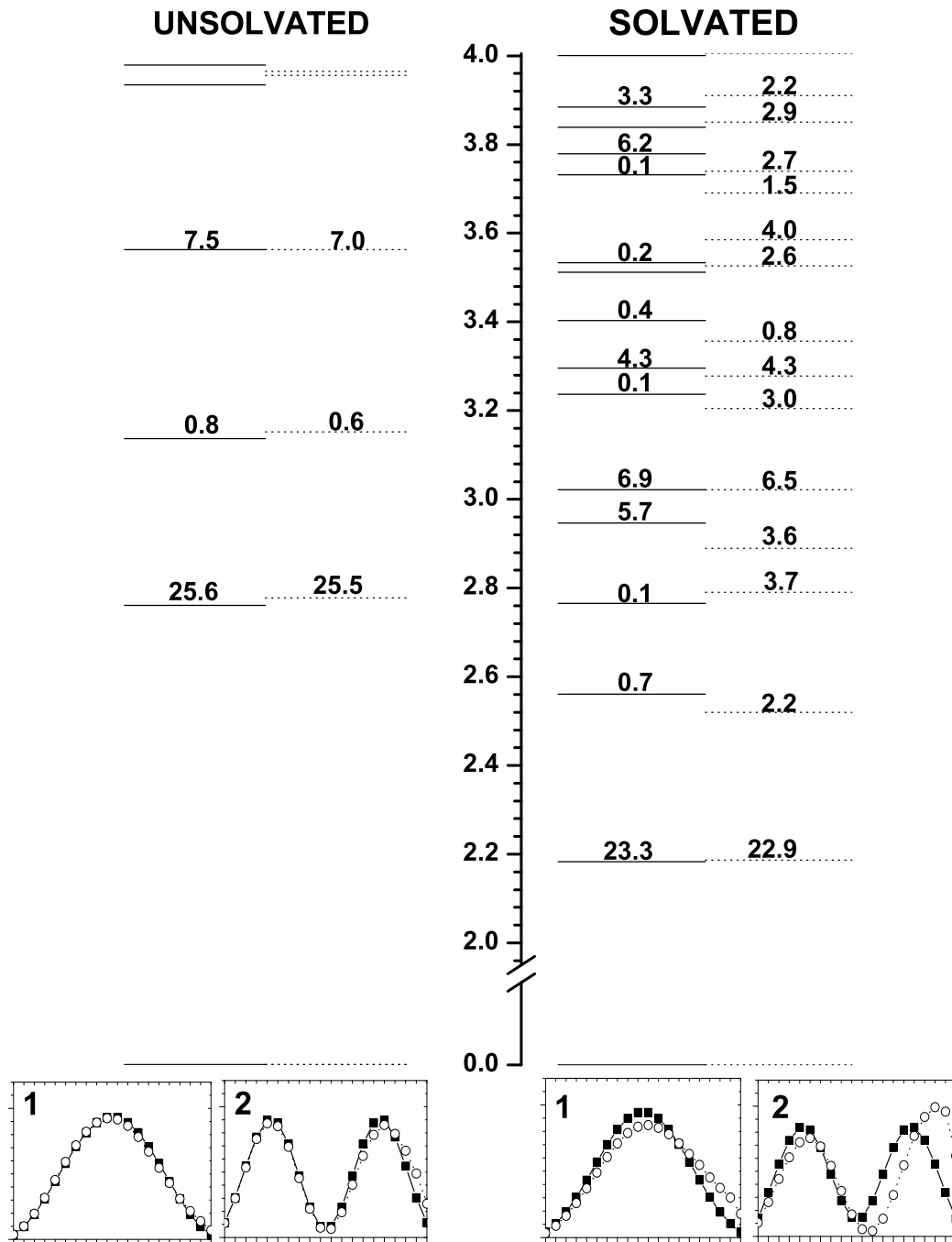


**Figure 5.1:** Excited state energy levels with and without dielectric solvation for 20 unit cells of polyacetylene with (dotted lines) and without (solid lines) a carbonyl defect at the end of the chain. The numbers indicate the oscillator strength to that state. The probability densities per unit cell for  $e_{cent}^-$  effective particles for the lowest two excited states, labelled 1 and 2, are shown at the bottom. The filled squares are for a regular polyene and the open circles are for a polyene with a carbonyl defect.

A standard quantum chemistry calculation would yield the energy levels and transition moments of Figure 5.1 for a chain without inclusion of dielectric solvation. It is not evident from these results how the carbonyl alters the photophysics of the system. In particular, it is not clear what effect the carbonyl defect has on the exciton in the  $1^1B_u$  state. However, an interpretive model can provide insight into the connection between the structure of the system and its function, which will now be demonstrated using the effective particle approach.

Figure 5.2 gives the unsolvated energy landscapes (solid lines) and position-dependent effective masses (dotted lines) for a 20 unit cell oligomer of polyacetylene with and without the terminal aldehyde group, using all three conventions for the center of the effective particle. As explained in Section 4.2.1, the  $e_{cent}^-$  ( $h_{cent}^+$ ) convention follows the behavior of an electron (hole) as it moves through the material, while the  $e^-h_{cent}^+$  effective particle follows the electron and hole as they move together. For the  $h_{cent}^+$  effective particles in Figure 5.2, the energy landscape drastically increases by 2.09 eV on the carbonyl unit cell, and the effective mass becomes heavier by 0.35 eV. This indicates that the hole prefers to avoid the carbonyl. The opposite is seen for the  $e_{cent}^-$  effective particles. Since a carbonyl group has electron-withdrawing character, the electron is expected to be drawn towards the carbonyl, which is apparent from the 0.18 eV decrease in the energy landscape and the effective mass becoming lighter by 0.22 eV. For the  $e^-h_{cent}^+$  effective particles, the energy landscape increases by 0.45 eV at the carbonyl, and the effective mass become lighter by 0.09 eV. Since  $e^-h_{cent}^+$  effective particles force the electron and hole to be together, these results indicate that it is more difficult to create both the electron and hole on the carbonyl together. Apparently, the repulsion of the hole from the carbonyl offsets the attraction of the electron when both must travel together.

As discussed in Section 3.3.2, one of the benefits of using a site model derived from segment-localized molecular orbitals is the ability to view the probability density for finding the effective particle at a particular position. The inset graphs in Figure 5.2 show the probability densities per unit cell for the  $1^1B_u$  state, without inclusion of dielectric solvation. These graphs indicate that there is a negligible increase in the wavefunction probability near the carbonyl defect.

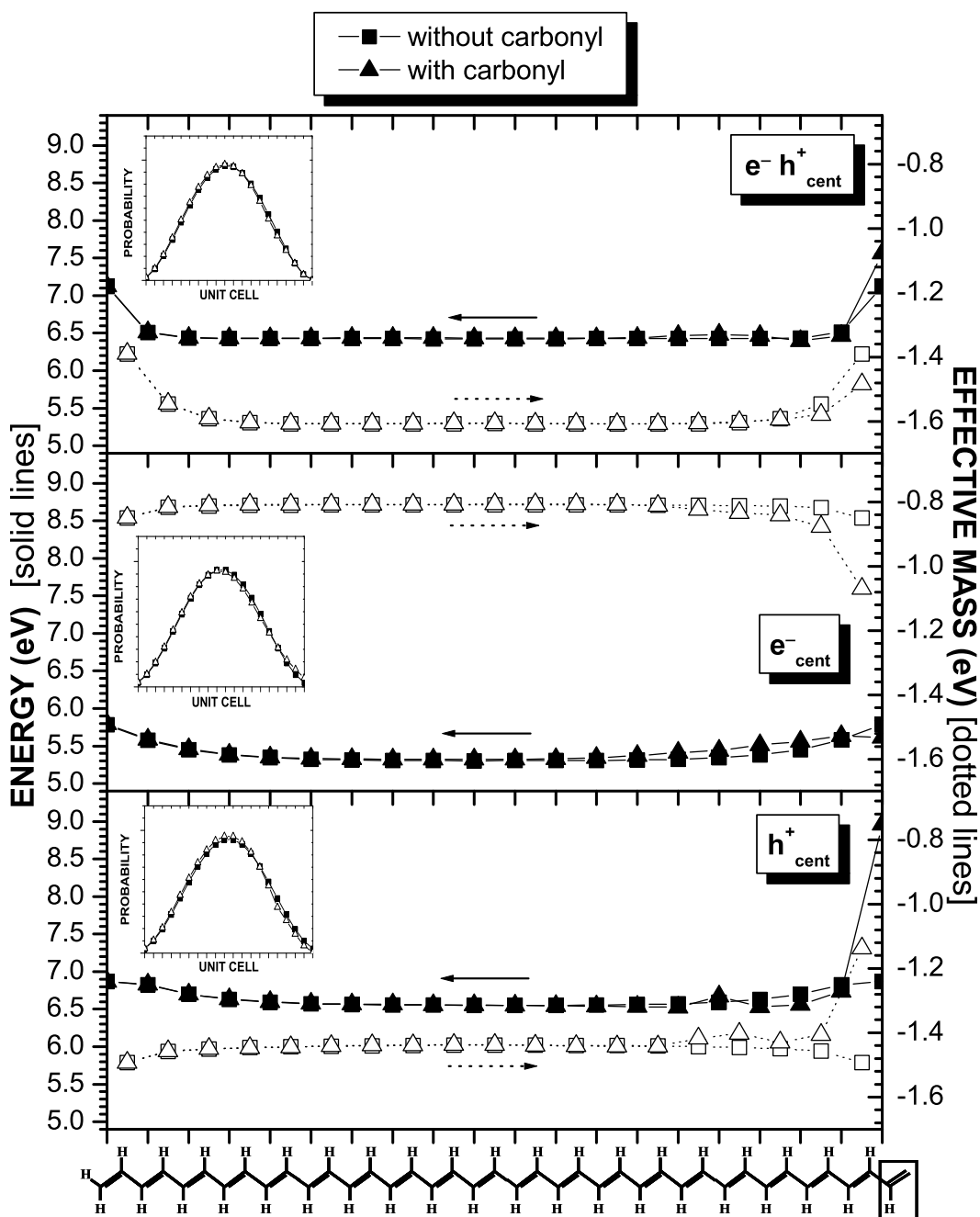


**Figure 5.2:** Energy landscapes (solid lines) and effective masses (dotted lines) without dielectric solvation for 20 unit cells of polyacetylene with (triangles) and without (squares) a carbonyl defect at the end of the chain. The inset graphs correspond to the probability density per unit cell for the  $1^1B_u$  state. The  $1^1B_u$  state energies and dipole moments are given in Table 5.1.

**Table 5.1:** The  $1^1B_u$  state energies (eV) and dipole moments (D) obtained from a full S-CI calculation for polyacetylene and PPV chains with and without chemical defects, corresponding to the curves in Figures 5.2, 5.3, 5.6, 5.7, and 5.10.

	NO SOLVATION			SOLVATION		
	$1^1B_u$ energy	GS dipole	$1^1B_u$ dipole	$1^1B_u$ energy	GS dipole	$1^1B_u$ dipole
<b>polyacetylene</b>	2.78	0.20	0.20	2.18	0.20	0.27
with carbonyl defect	2.80	7.12	9.65	2.19	7.12	17.01
<b>PPV</b> (solv = 1.25)	3.05	0.11	0.12	2.53	0.11	1.23
PPV (solv = 1.75)				2.23	0.11	0.43
with carbonyl defect	3.05	5.44	5.83	2.23	5.44	11.39
with <i>meta</i> -linkage defect	3.11	0.07	0.04	2.60	0.07	0.42

The results obtained with the inclusion of dielectric solvation are given in Figure 5.3. For the  $h_{cent}^+$  effective particles, the solvation leads to a slightly larger increase in the energy landscape on the carbonyl defect, and a somewhat larger increase in effective mass. For the  $e^-h_{cent}^+$  effective particles, the energy landscape increase at the carbonyl defect is slightly less than that for the unsolvated case, and the effective mass difference remains the same. However, solvation causes a drastic change in the  $e_{cent}^-$  effective particle results. For these effective particles, the energy landscape decreases by 0.54 eV on the carbonyl defect, which is three times more than that seen for the unsolvated case. The inset graph for the  $e_{cent}^-$  effective particles also shows a shift of the probability density towards the carbonyl side of the oligomer. This indicates that the electron is drawn towards the carbonyl when dielectric solvation is included.

The dipole moments for both the ground state and the  $1^1B_u$  excited state are listed in Table 5.1. (The small dipole moments in the regular polyacetylene oligomer result from slight asymmetry in the AM1 optimized geometry.) The carbonyl defect leads to 7.1 D dipole moment in the ground state. Without dielectric solvation, the change in dipole moment on excitation to the  $1^1B_u$  state is only about 2.5 D, but this increases to 9.9 D in the dielectric. This large change in the dipole moment indicates that the inclusion of dielectric solvation stabilizes a greater charge separation between the electron and hole.

This conclusion is also apparent by looking at the electron-hole correlation as a function of the unit cell position. Figure 5.4 gives the correlation of the hole position

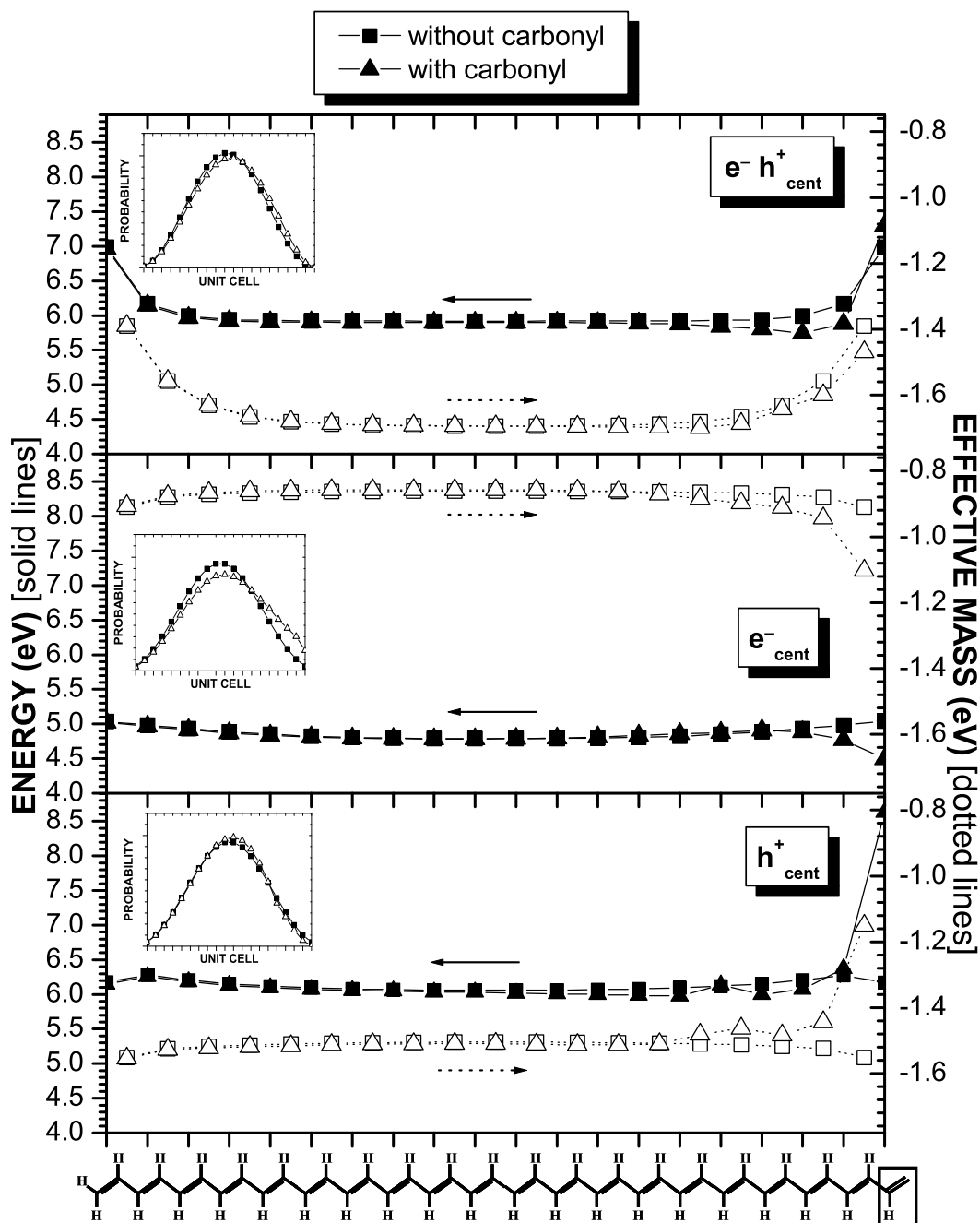


**Figure 5.3:** Same as Figure 5.2, except with dielectric solvation included. The  $1^1B_u$  state energy obtained from the full S-CI calculation for polyacetylene is 2.18 eV, and is 2.19 eV with the carbonyl defect.

relative to the unit cell location of the electron. Each curve in Figure 5.4 corresponds to a different location of the electron, and the curve indicates the degree to which the hole is bound to the electron at that position. (The correlation is analogous to the size of the effective particle.) For a polyacetylene chain with no defect and no dielectric solvation, the electron and hole prefer to be one unit cell apart, with the maximum separation being approximately 4 unit cells. The electron-hole separation increases slightly at the ends of the chain due to chain-end effects (see Section 4.4.1). With the inclusion of solvation, the maximum electron-hole separation increases slightly, especially at the ends of the chain. The inclusion of a carbonyl defect causes a greater separation between the electron and hole, and this separation is significantly greater in the calculations that include dielectric solvation. When the electron is on the carbonyl defect, the hole prefers to be *at least* 3 unit cells away from the electron, and this charge separation is stabilized by the inclusion of the dielectric screening. These results show that, when dielectric solvation is included, the carbonyl defect serves as an attractor for the electron, and that when the electron is on the carbonyl defect, the hole is about 3 unit cells away. This is in qualitative agreement with Rothberg's suggestion that the carbonyl defect quenches fluorescence by serving as an electron trap.<sup>19</sup> However, our results do not indicate that the trapping ability of the carbonyl defect is sufficient to dissociate the exciton.

### 5.3.2 PPV with Carbonyl Defect

In order to further investigate the effects of carbonyl defects on a luminescent conjugated polymer, this section presents results for a PPV oligomer with 12 unit cells. The results are shown in Figs. 5.5-5.7. The results are qualitatively similar to those obtained for the polyacetylene oligomer, except that the electron trapping ability of the carbonyl appears to be somewhat weaker in PPV than in polyacetylene. For instance, the solvated energy landscape for the  $h_{cent}^+$  effective particles in Figure 5.7 only rises by 0.58 eV at the carbonyl defect, and the particle gets slightly lighter. (Calculations were also performed with the benzene and vinyl groups being in their own unit cells, and this increase in delocalization was shown to be due to the

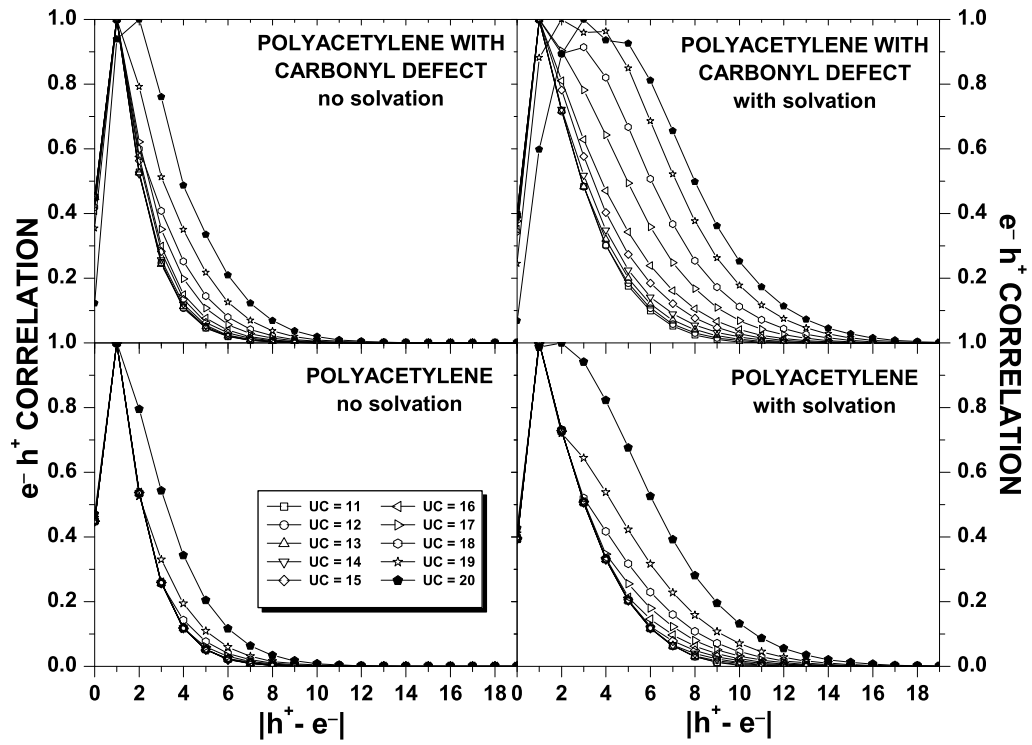


**Figure 5.4:** The normalized electron-hole correlations per unit cell for 20 unit cells of polyacetylene with (top) and without (bottom) a carbonyl defect at the end of the chain, for  $e_{cent}^-$  effective particles. Only the correlations for the half of the chain containing the carbonyl defect are included. Each curve in Figure 5.4 corresponds to a different location of the electron, and the width of the curve indicates the degree to which the hole is bound to the electron at that position. The electron-hole correlation for the defect unit cell is indicated with filled-in symbols.

benzene ring, not the carbonyl. The effective particle got heavier on the carbonyl in these calculations.) For the  $e_{cent}^-$  effective particles, the energy landscape value drops 0.16 eV more at the carbonyl defect than it did for polyacetylene, with only a slight change in the effective mass. The inset graphs in Figure 5.7 show that the probability density is shifting towards the carbonyl a bit, although not as much as that seen for polyacetylene. Finally, a large change in the solvated excited state dipole is observed in Table 5.1, which indicates that the electron and hole are more separated and less bound. This decrease in the bound character of the electron and hole can also be seen in the correlation functions in Figure 5.8.

### 5.3.3 PPV with *meta*-linkage Defect

The inclusion of a *meta*-linkage defect within a PPV chain of 12 benzene rings was also investigated using the effective particle approach. The energy landscapes and position-dependent effective masses are given in Figure 5.10. These results include dielectric solvation; the unsolvated results are qualitatively similar. The  $1^1B_u$  excited state energies and dipole moments are given in Table 5.1. The slight increase in the  $1^1B_u$  state energy relative to a regular PPV oligomer indicates that the excited states are sensitive to this geometric defect. Similar results are obtained for all three conventions for the effective particle center shown in Figure 5.10. The energy landscapes show that the *meta*-linkage serves a break in conjugation, both by raising the energy of the effective particle on the defect and by leading to an increase in effective mass near the particle. The increase in effective mass corresponds to a weaker electronic coupling across the defect. The landscapes seen on either side of the defect are in good agreement with those predicted for a PPV oligomer with 6 unit cells. The inset graphs show that the probability density is distributed between the wells, with more probability been seen in the well at right, which is longer in length by one unit cell. These results demonstrate that the effective particle method can give quantitative information on the manner in which a defect such as *meta*-linkage breaks conjugation in conjugated polymers.

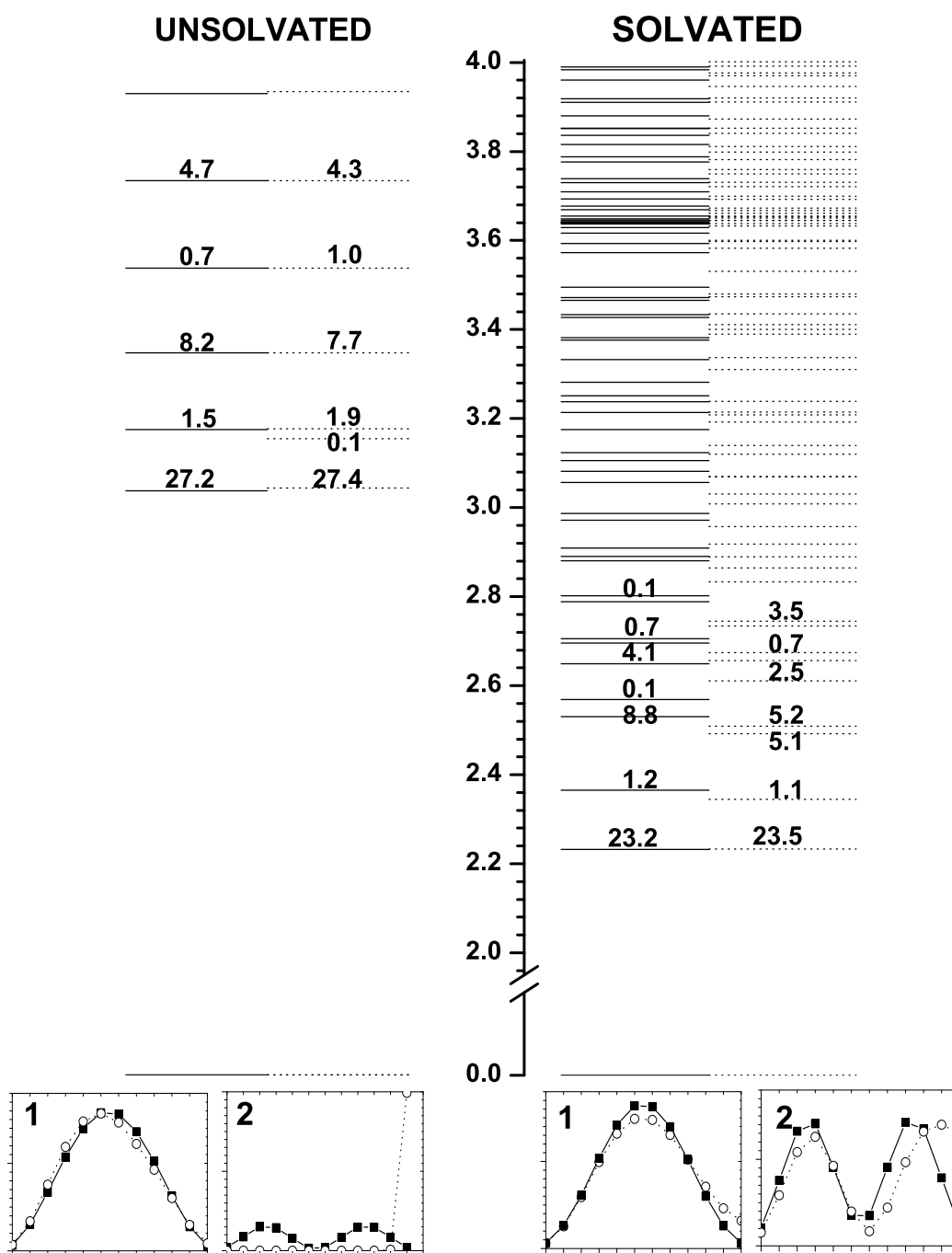


**Figure 5.5:** Excited state energy levels with and without dielectric solvation for 12 unit cells of PPV with (dotted lines) and without (solid lines) a carbonyl defect at the end of the chain. The numbers indicate the oscillator strength to that state. The wavefunction probability per unit cell for  $e_{cent}^-$  effective particles for the lowest two excited states are also indicated.

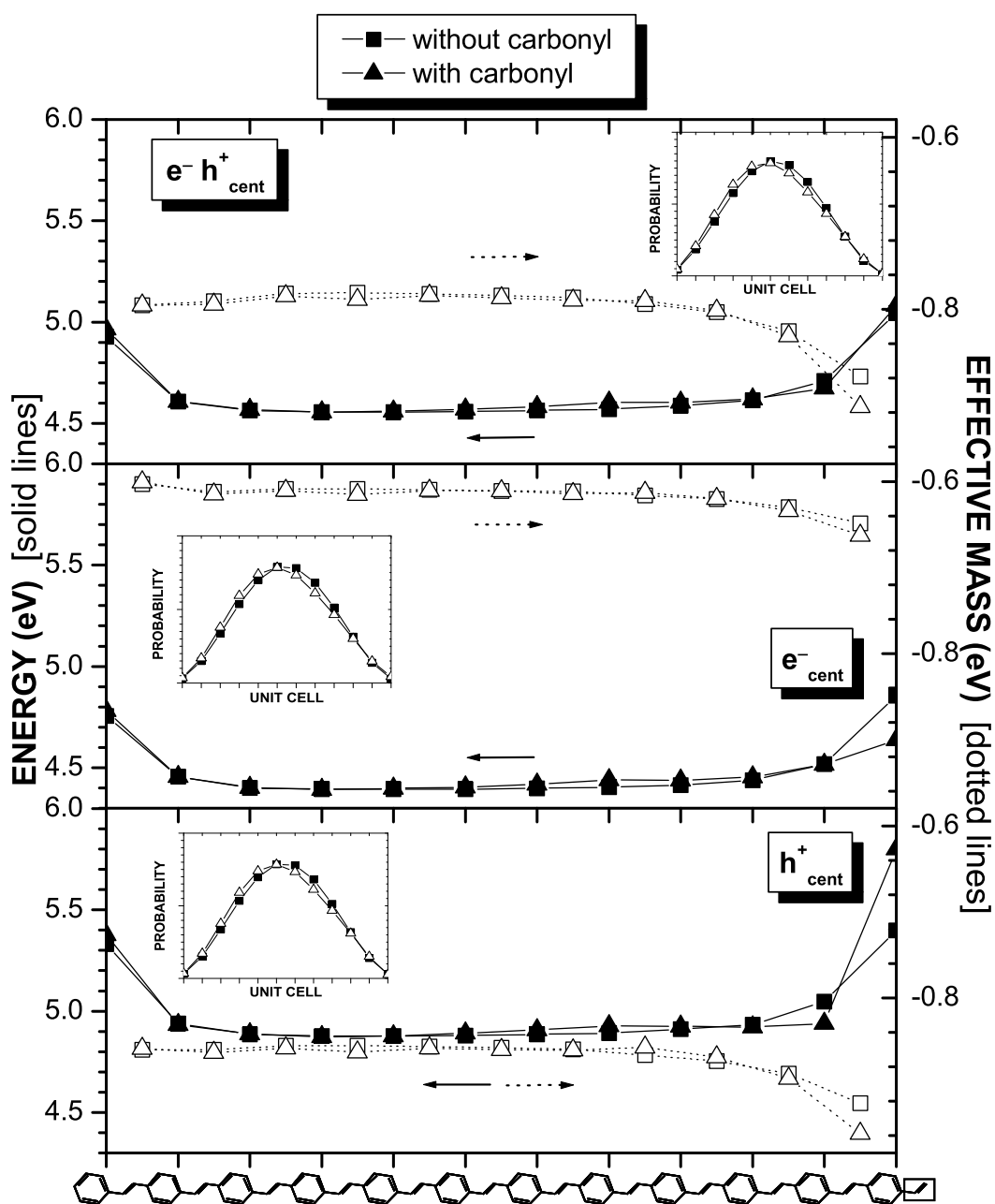


**Figure 5.6:** Energy landscapes (solid lines) and effective masses (dotted lines) without dielectric solvation for 12 unit cells of PPV with (triangles) and without (squares) a carbonyl defect at the end of the chain. The inset graphs correspond to the wavefunction probability per unit cell for the  $1^1B_u$  state. The  $1^1B_u$  state energies and dipole moments are given in Table 5.1.

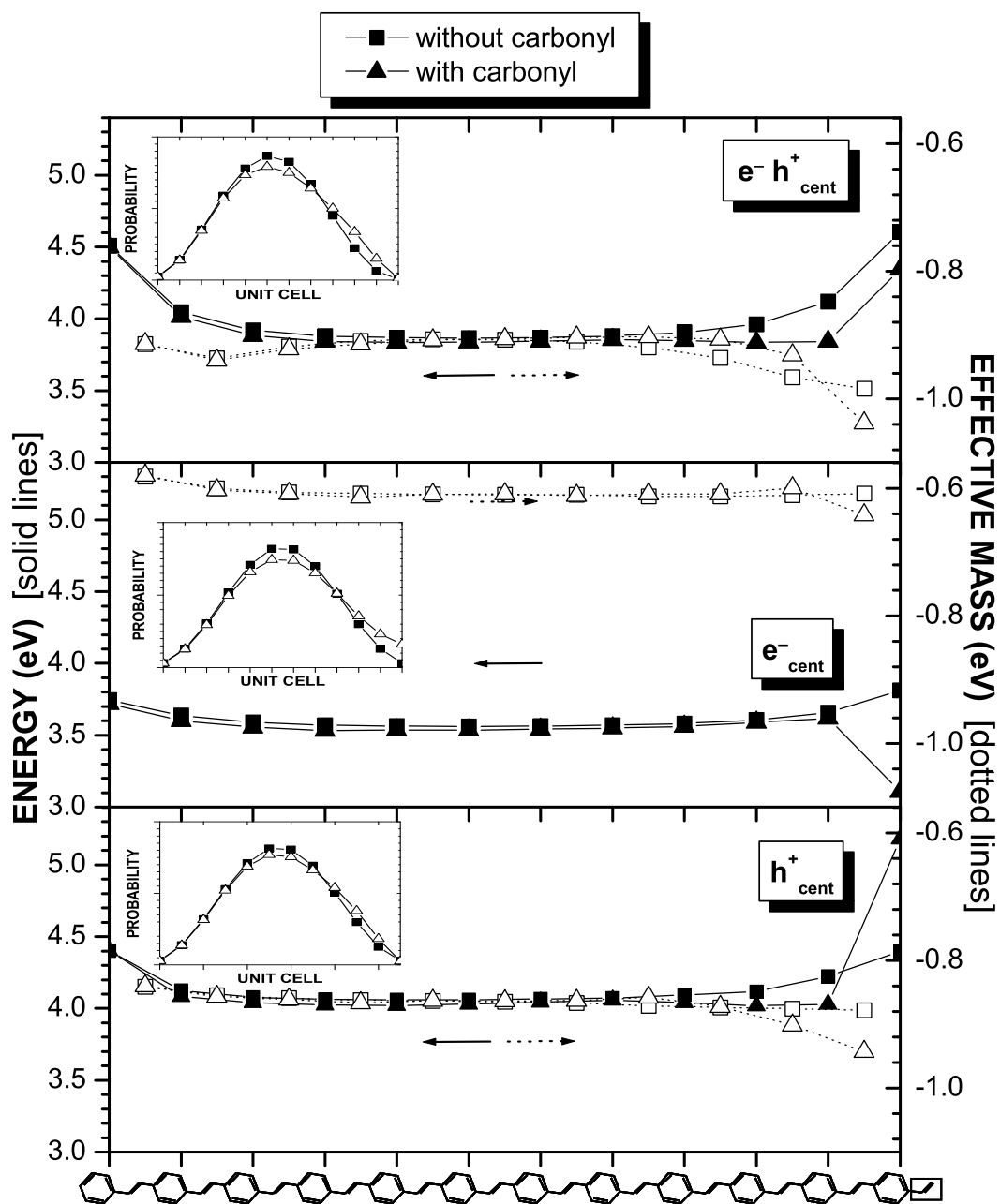
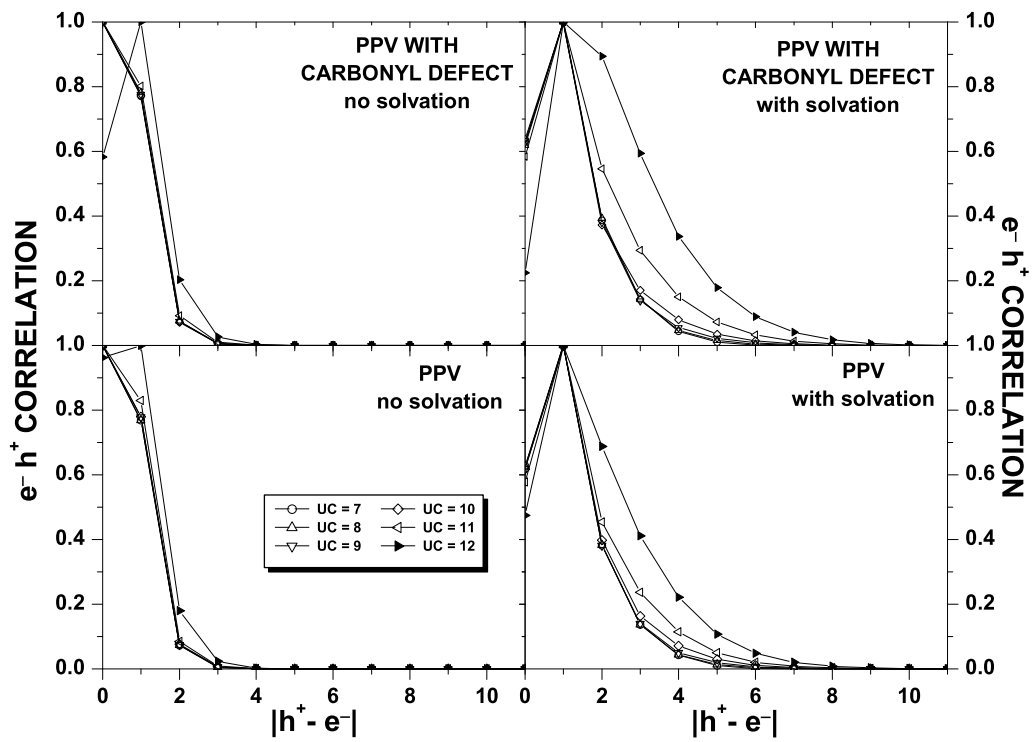
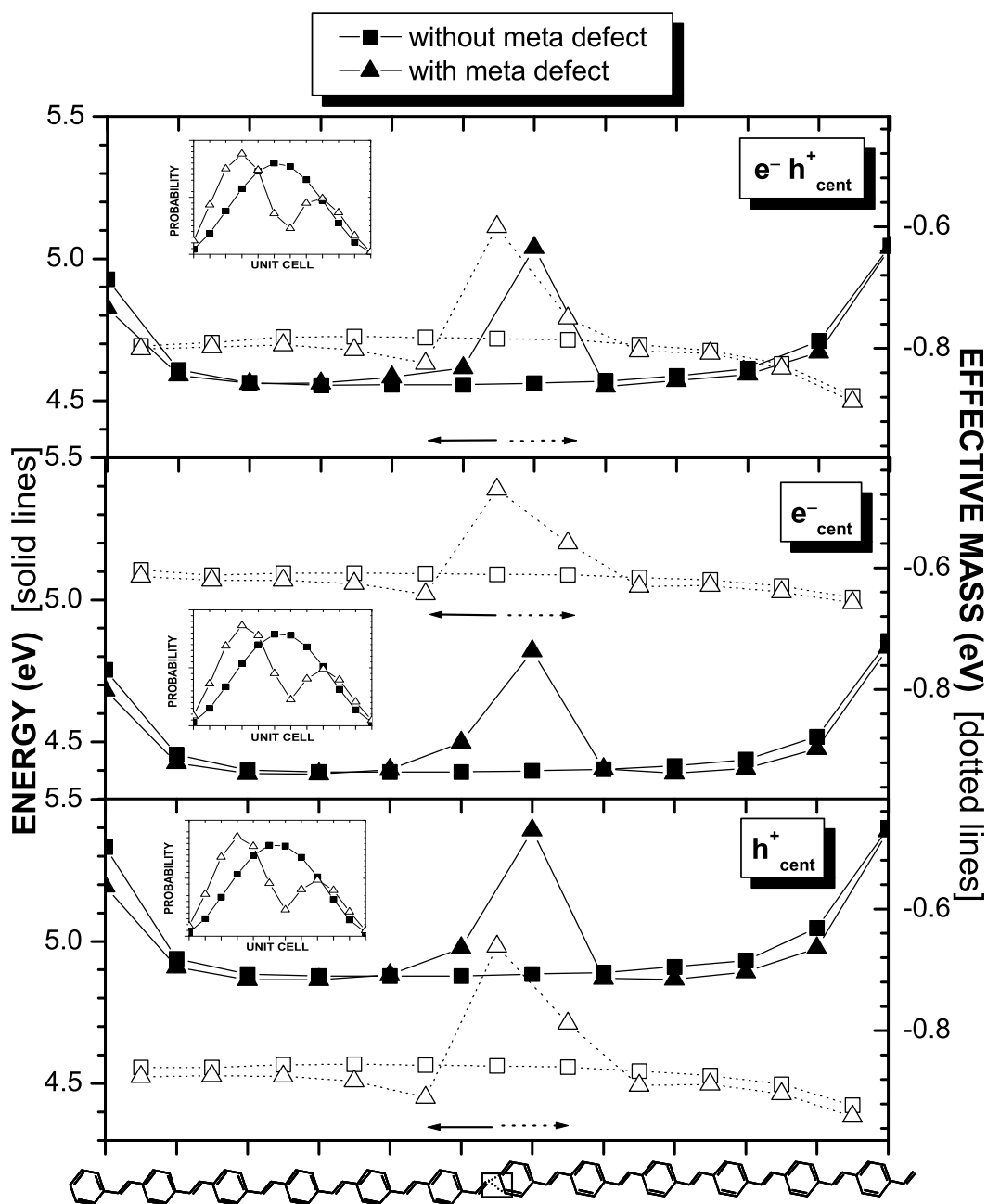


Figure 5.7: Same as Figure 5.6, except with dielectric solvation included.



**Figure 5.8:** The normalized electron-hole correlations per unit cell for 12 unit cells of PPV with (top) and without (bottom) a carbonyl defect at the end of the chain for  $e_{cent}^-$  effective particles. Only the correlations for the second half of the chain is included. The electron-hole correlation for the defect unit cell is indicated with filled-in symbols.



**Figure 5.9:** Energy landscapes (solid lines) and effective masses (dotted lines) for 12 unit cells of PPV with (triangles) and without (squares) a *meta*-linkage defect at the center of the chain. Dielectric solvation is not included. The stars show the landscapes obtained for a regular PPV oligomer with 6 unit cells. The inset graphs show the probability density per unit cell for the  $1^1B_u$  state for PPV with (hollow triangles) and without (solid squares) a *meta*-linkage defect. The  $1^1B_u$  state energies and dipole moments are given in Table 5.1.

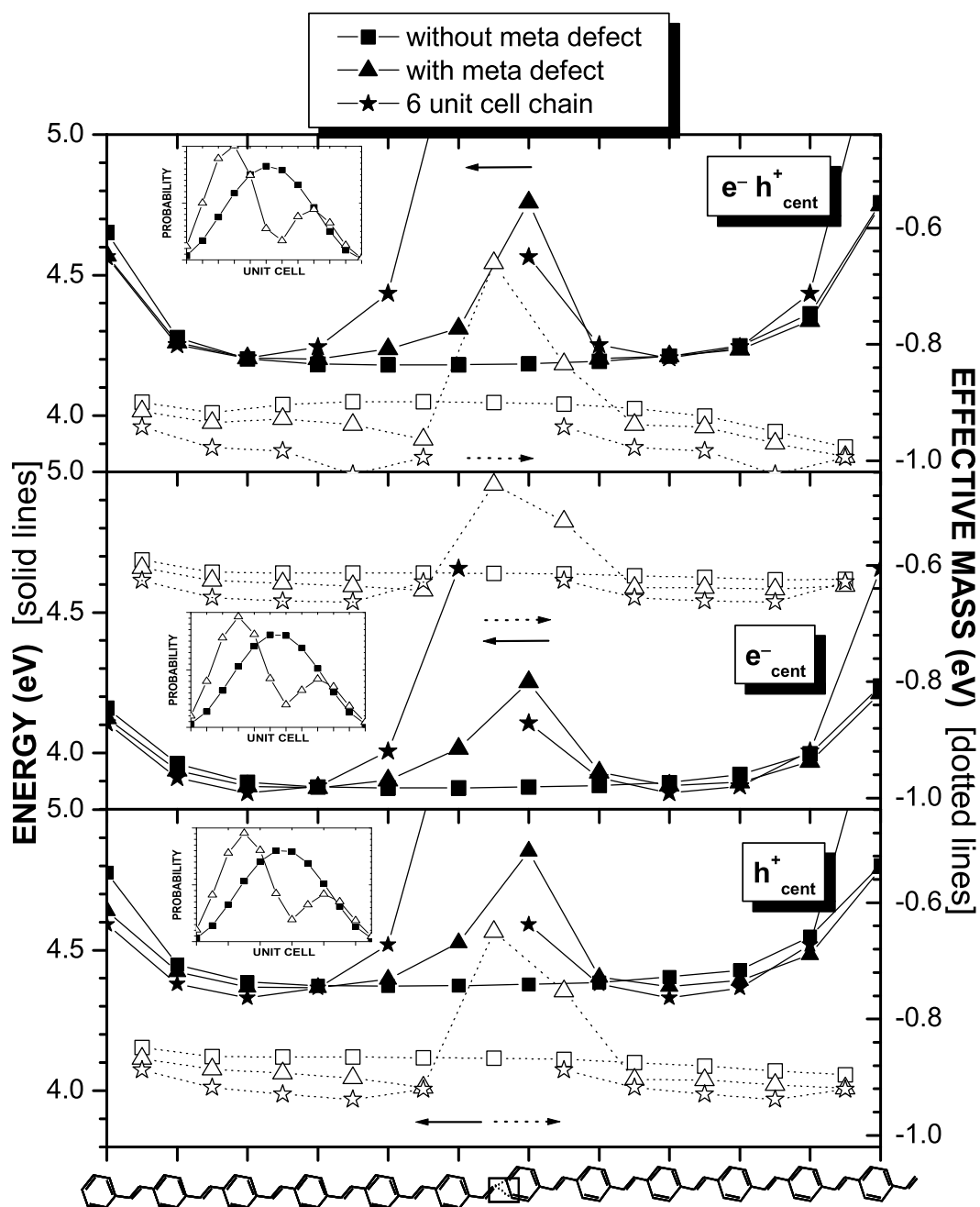


*Figure 5.10:* Same as Figure 5.9, but with dielectric solvation included. The results are qualitatively similar.

## 5.4 Conclusion

These calculations provide insight into how a chemical defect affects the photophysics of conjugated polymers. It was shown that a carbonyl defect acts as an electron-withdrawing trap, and that it plays a role in reducing the bound character of the exciton. This decrease in the bound character of the exciton can be seen by looking at the electron-hole correlation of the effective particle on each unit cell, and by the increase in the  $1^1B_u$  state dipole moment. This charge separation between the electron and hole is stabilized with the inclusion of dielectric screening. The decrease in the bound character of the exciton can lead to a reduction in the luminescence quantum yield. The presence of *meta*-linkage was shown to cause a break in the  $\pi$  conjugation, and the wavefunction probability density indicates that the exciton prefers to be on the longer segment. These results quantify the manner in which a *meta*-linkage breaks conjugation in PPV, and may be used in creating a site-model for materials with such defects.

## Chapter 6

# Application to Conformational Disorder

### 6.1 Introduction

The photophysics of conjugated polymers depend not only on the chromophores in the polymer backbone, but also on the morphology of the material. The effects of the morphology on the photophysics are often described in terms of an effective conjugation length, or set of effective conjugation lengths, present in the material.<sup>29,32,35-39,123</sup> One approach to estimating the effective conjugation length is to compare the optical absorption spectrum of oligomers with that observed for polymers. For a perfectly ordered polymer chain, the energy of the  $1^1B_u$  state, the lowest allowed one-photon state, should red-shift with increasing chain length in a manner that is inversely proportional to the length of the oligomer. However, the experimental absorption spectra typically saturate as the length of the chain is increased, and the point at which this saturation occurs may be taken as the effective conjugation length.<sup>124</sup>

The inhomogeneous broadening observed in optical absorption and emission spectra is also typically viewed as arising from a distribution of effective conjugation lengths in the sample.<sup>38,76</sup> For instance, a joint experimental and theoretical study on polyacetylene and  $\beta$ -carotene<sup>77</sup> expressed the observed inhomogeneously broadened

linear absorption spectra as a superposition of spectra for shorter conjugated segments, and found that the spectrum was dominated by the shorter segments. It has also been observed that the average conjugation length increases as the temperature decreases, which has been attributed to a decrease in the amount of chain torsion with decreasing temperature.<sup>77,125</sup> Similarly, spectral diffusion in conjugated polymers is often interpreted in terms of effective conjugation lengths, such that the red shift of the luminescence arises from exciton migration to segments with increasingly longer effective conjugation lengths.<sup>29,35,36,38,126–130</sup>

In terms of materials optimization, manipulation of the effective conjugation length can allow the luminescence properties of a material to be fine-tuned. This can be achieved synthetically by, for instance, intentionally including chemical defects such as a *meta*-linkage,<sup>73–75</sup> *cis*-linkages,<sup>120</sup> or nonconjugated spacers.<sup>121</sup>

Although the effective conjugation length is a useful qualitative concept, the precise connection between the molecular structure of the material and the effective conjugation length remains elusive. Most models attribute the loss of conjugation to torsional rotations that decrease the  $\pi$  overlap between unit cells. For instance, Bitner *et al.* used a Monte Carlo technique to generate an ensemble of structures for long chains of PPV.<sup>125,131–134</sup> The distribution of effective conjugation lengths was then generated by assuming that the conjugation was broken whenever the torsional angle between nearest-neighbor phenylene units was greater than some cut-off angle. Given the continuous distribution of torsional angles, it is not clear that use of a cut-off correctly captures the relation between the structure and the photophysically observed effective conjugation length.

This chapter illustrates how the effective particle approach developed in Chapter 4 may be used to quantify the connection between molecular structure and effective conjugation length. The bridge between structure and conjugation length is provided by the energy and effective mass landscapes, since these relate the structure of the polymer to the dynamics of the exciton present in the excited state. The results are given for a PPV oligomer with 8 unit cells, 4 of which are perfectly planar and 4 of which are nonplanar. The results indicate that relatively moderate torsional angles are sufficient to localize the exciton on the planar segment.

## 6.2 Methodology

The PPV oligomer used to investigate the effects of torsional disorder is shown at the bottom of Fig. 6.2. The oligomer has 8 phenylene groups, with the first four held planar and the second four held at varying degrees of nonplanarity according to the torsional angles shown Fig. 6.2. The structures are optimized using the PM3 Hamiltonian<sup>122</sup> in MOPAC, with constraints applied to the dihedral angles between nearest neighbor phenylene units. Structures were generated with  $\theta$  of Fig. 6.2 varying from 0 to 60°, in increments of 5° to 30°, and then in increments of 10°. Structures were also generated for the 4 unit cell oligomers corresponding to the left and right halves of the system.

Excited-state electronic structure calculations were performed with the INDO Hamiltonian (Section 2.3.3). Localized molecular orbitals were obtained using the method described in Chapter 3, with the molecular segments defined as the unit cells of the oligomer. Direct-CI,<sup>135</sup> which was recently implemented in our code,<sup>136</sup> enables excitations among all  $\sigma$  and  $\pi$  valence molecular orbitals to be efficiently included in the calculations, and was used to calculate the  $1^1B_u$  excited electronic state. No dielectric solvation was included. The effective particle approach described in Chapter 4 was used to generate energy and effective mass landscapes, using only  $e_{cent}^-$  for the center of the effective particle.

## 6.3 Results and Discussion

For the 8 unit cell oligomer of PPV depicted at the bottom of Figure 6.2, the heat of formation obtained from MOPAC as a function of the dihedral angle,  $\theta$ , is given in Figure 6.1. The conformations that lie below  $kT$  at room temperature (0.6 kcal/mol, 0.025 eV) are also indicated. These results indicate that significant torsional disorder (ie,  $\theta \leq 15^\circ$ ) is expected for PPV in solution at room temperature. Although the conformation energies shown in Figure 6.1 will be dominated by the packing forces and chain entanglement in the solid state, significant torsional disorder seems likely for amorphous samples.

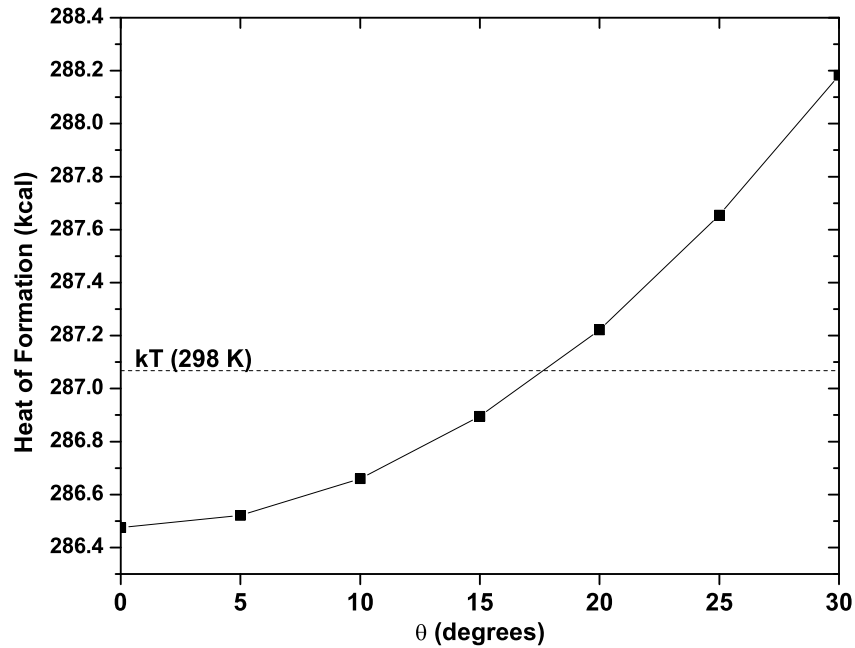


**Figure 6.1:** The heat of formation vs. the torsion angle, obtained from a MOPAC calculation.

Fig. 6.2 shows the energy landscapes for the PPV oligomers using  $e_{cent}^-$  effective particles. The energy landscape is higher on the disordered side of the chain, and increases with increasing torsional angle. The effective mass landscapes in Fig. 6.3 indicate that the effective particle becomes heavier in the disordered region, as expected since the  $\pi$  overlap between unit cells decreases with  $\theta$ . Comparison with the landscapes obtained for oligomers with 4 unit cells indicates that the landscape of the 8 unit cell oligomer is qualitatively similar to that expected from piecing together two oligomers. The significant jump between  $30^\circ$  and  $40^\circ$  in both Figures 6.2 and 6.3 indicate that a torsional rotation of this magnitude causes the effective particle to prefer to be located on the flatter segment. The localization of these effective particles is exemplified in Figure 6.4, which shows the probability density for the the center of the effective particle as a function of its unit cell location. These results indicate that the wavefunction becomes localized on the planar region of the oligomer when  $\theta \geq 40^\circ$ .

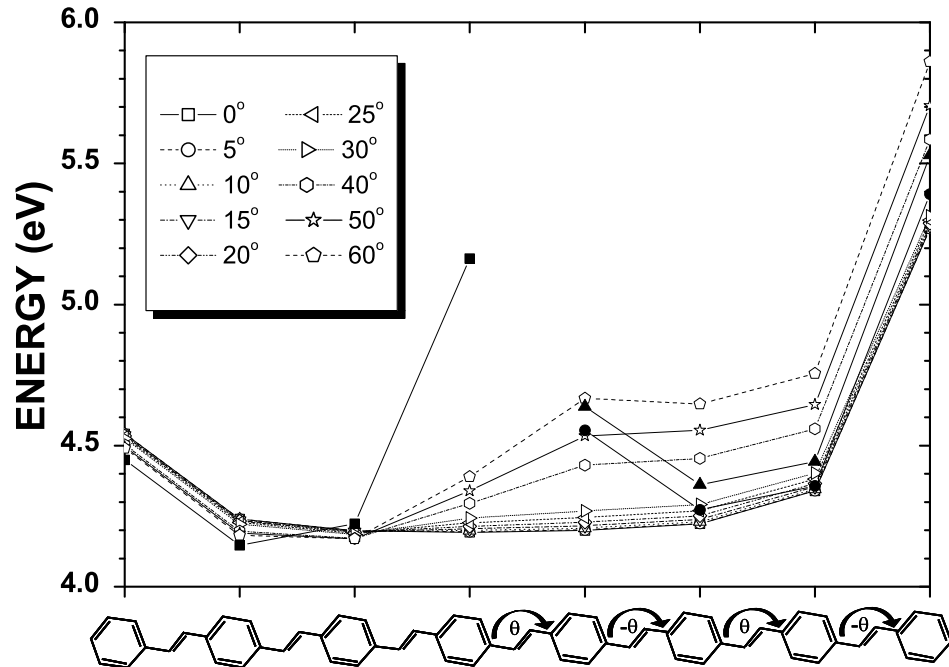


**Figure 6.2:** Energy landscapes for the  $1^1B_u$  state using  $e_{cent}^-$  effective particles of a 8 unit cell PPV oligomer, which is depicted at the bottom of the figure. The torsional angle,  $\theta$  is increased from  $0^\circ$  to  $60^\circ$ . The filled-in symbols give the landscapes for a planar 4 unit cell oligomer (left) and a 4 unit cell oligomer with torsional angles of  $40^\circ$  and  $60^\circ$  (right). Dielectric solvation is not included. The  $1^1B_u$  state energies are given in Table 6.1.

**Table 6.1:** The  $1^1B_u$  state energies (in eV) obtained from a full S-CI calculation for the 8 unit cell PPV oligomer of Fig. 6.2 and for the 4 unit cell oligomer obtained from the right side of the structure shown in Fig. 6.2.

	$\theta = 0$	$\theta = 5$	$\theta = 10$	$\theta = 15$	$\theta = 20$	$\theta = 25$	$\theta = 30$	$\theta = 40$	$\theta = 50$	$\theta = 60$
4 unit cells	3.116							3.381		3.545
8 unit cells	2.910	2.911	2.915	2.922	2.931	2.942	2.956	3.015	3.034	3.048

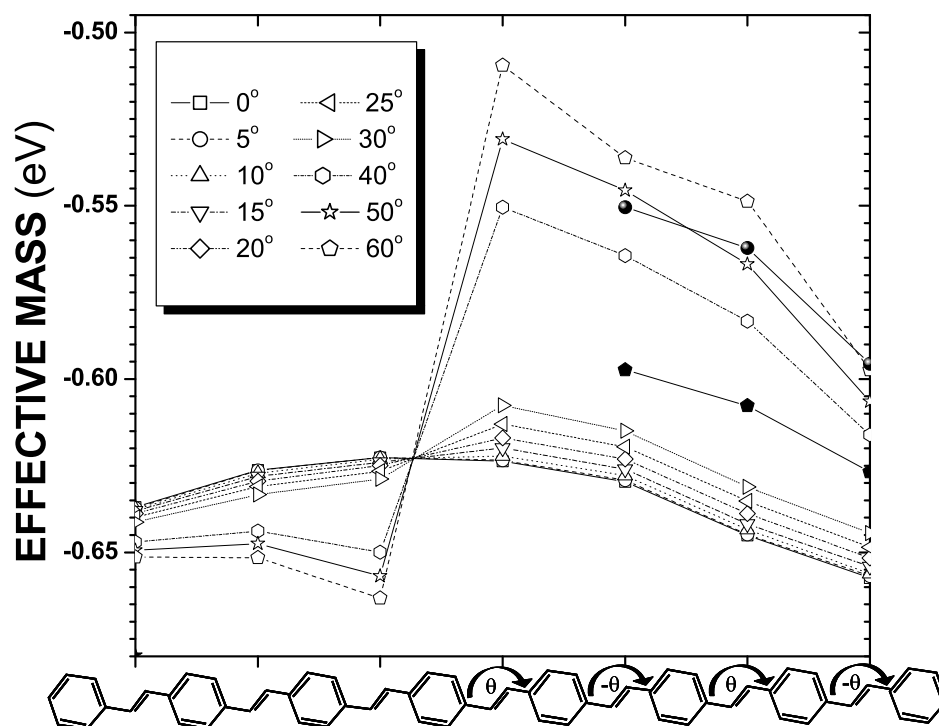


*Figure 6.3:* The effective mass landscapes for the system of Figure 6.2, using equivalent notation.

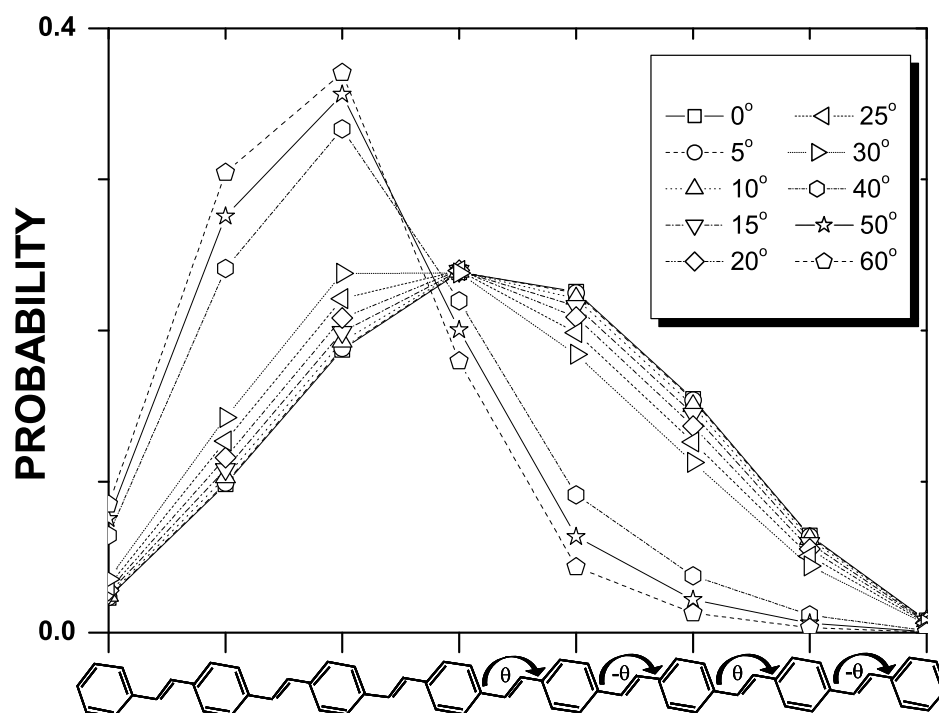


**Figure 6.4:** The probability density for the center of the  $e_{cent}^-$  effective particle as a function of the unit cell location of the effective particle center.

Comparison of the  $1^1B_u$  state energies of Table 6.1 with the heats of formation in Fig. 6.1 reveal that the torsional potential is much stiffer in the excited state than in the ground state. In Fig. 6.1, distorting the polymer with a torsional angle of  $10^\circ$  raises the energy of the ground electronic state by only about 0.18 kcal/mole (0.008 eV), whereas the excitation energy is increased by 0.12 kcal/mole (0.005 eV). This leads to a somewhat stiffer torsional potential in the excited state, implying that creation of the excited state will tend to planarize the oligomer in solution.

## 6.4 Conclusion

The results presented in this chapter illustrate the use of the effective particle methodology to quantify the connection between the structure of a conjugated polymer system and the resulting photophysics. The studies reveal that relatively moderate torsional distortions, on the order of  $35^\circ$  to  $40^\circ$ , have fairly large effects on the energy and reduced mass landscapes for the  $1^1B_u$  state. These torsions have little effect on the energy of the ground and excited  $1^1B_u$  electronic states, but a stiffening of the torsional potential in the excited state is seen. This torsional potential stiffening in the  $1^1B_u$  should lead to a planarization of the excited state and make a significant contribution to the observed Stokes shift in solution.

The results presented here illustrate that a site model is possible for disordered conjugated polymers, and provides a means to extract the parameters for such a model from quantum chemical calculations. For instance, the energy and effective mass landscapes of Figs. 6.2 and 6.3 show how the site energies and Hamiltonian coupling matrix elements change with torsional angle in PPV. The observed agreement between the landscape of an 8 unit cell oligomer and its constituent 4 unit cell oligomers suggests that these parameters are transferable to arbitrary length systems. It should be possible to use such site models to make quantitative predictions regarding how the effective conjugation length, as observed in photophysical experiments, is related to the underlying chemical structure of the material. Such models are, however, left to future work.

# Chapter 7

## Application to Exciton-Exciton Interactions

### 7.1 Introduction

The photophysical and semiconducting properties of conjugated polymers enable the construction of devices such as light-emitting diodes<sup>1-4</sup> and solid-state lasers.<sup>6-10</sup> But despite this functional similarity between organic and inorganic semiconductors, there are some significant differences in the details of the photophysics. Of particular interest is the effective strength of Coulomb interactions between an electron and hole. Such interactions can lead to the formation of bound electron-hole pair states, or excitons. In conjugated polymers, estimates of the exciton binding energy range from 0.2 and 0.9 eV, much larger than the 10s of meV seen in inorganic semiconductors. So, unlike inorganic semiconductors, excitons play an important role in the room temperature photophysics of conjugated polymers. For instance, the  $1^1B_u$  state of conjugated polymers is the lowest energy exciton state, and this state carries most of the one photon intensity out of the electronic ground state. Here, we examine the nature of the interaction between excitons and, in particular, whether such interactions can lead to binding between two excitons to form a biexciton state. These interactions may be especially important in applications that rely on high exciton densities such as solid-state lasers.<sup>6-10</sup>

Coherent many-particle states, such as biexciton states, are known to exist in inorganic semiconductors.<sup>137</sup> Although biexciton states have been observed in molecular aggregates<sup>138</sup> and charge transfer crystals,<sup>139</sup> their existence in other organic semiconductors remains uncertain.<sup>140</sup> Several researchers have speculated that certain spectral features of conjugated polymers such as PPV are due to biexcitons.<sup>3,25,47,140–145</sup> For instance, the photoinduced absorption seen in PPV at 1.4 eV has been attributed to biexcitons,<sup>145</sup> although the biexciton binding energy implied by this assignment was observed to be unreasonably large.<sup>47,144,146</sup> Calculations performed on oligomers<sup>47,85,144,145,147–157</sup> suggest that biexcitons can exist in conjugated polymer chains. Since such calculations are difficult to perform on long polymer chains, results from oligomers are typically extrapolated to the long chain limit. While extrapolation typically yields an accurate depiction of the infinite chain for low lying excitations, this procedure can be problematic for high energy excitations.<sup>158</sup>

Because of chain length limitations and issues with size consistency,<sup>151</sup> our goal was to develop a size-consistent technique that could be applied to long polymer chains in order to study high energy exciton-exciton interactions, including spectral signatures of biexcitons. This is accomplished by using the scattering formalism described in Section 7.2. The Pariser-Parr-Pople (PPP) model of polyacetylene is used as a simple two-band model that captures the essentials of conjugated polymers. A Frenkel exciton model<sup>159–162</sup> is used as a benchmark for comparison, since the characterization of the biexciton within this model is fairly straightforward. Section 7.3 presents results obtained for oligomers, and for long chains with periodic boundary conditions. The excited-state absorption spectrum from the  $1^1B_u$  exciton state is calculated and examined for signatures of biexciton formation. No such signatures are found in the long-chain limit of the PPP model. The significance of these findings is discussed in Section 7.4.

## 7.2 Formalism

Much of the formalism used here was originally developed for nonresonant nonlinear optics, and a detailed justification of the approach and demonstration of its

size consistency is given in Ref. 58. Here, we briefly describe the method and provide details on its application to the calculation of excited-state absorption spectra.

The calculations are performed on the Pariser-Parr-Pople (PPP)<sup>163,164</sup> model of polyacetylene. The molecular geometry is fixed, which prevents formation of solitons and makes this a simple two-band model that captures the salient features of conjugated polymers.

We used periodic boundary conditions in order to study the limit of a long polymer chain. The Hartree-Fock band structure and Wannier functions are obtained as described in Ref. 58 and Chapter 2. The Hartree-Fock solution yields one valence and one conduction band, and their corresponding Wannier functions.

### 7.2.1 Scattering Formalism

To obtain a size-consistent and computationally tractable description of the two-photon excited states, we employ the scattering formalism described in Ref. 58. This is an equation-of-motion approach (see Section 2.4.1), where the ground state is the Hartree-Fock ground state, the one-photon states are obtained from S-CI theory, and the two-photon states are described by SD-EOM theory.

The use of S-CI for the one-photon states and SD-EOM for the two-photon states gives a balanced description, such that states containing two excitons are treated with an accuracy that is equivalent to that used for the one-photon states. This balance is, for instance, necessary to obtain a size consistent description of two-photon optical processes.<sup>58</sup> SD-EOM theory used in conjunction with this scattering formalism may not be adequate for more complex states such as the  $2^1A_g$ .

This need for a balanced description of the one and two photon states also influences the design of the contracted basis set in Section 7.2.3. The use of SD-EOM and the contracted basis set in these calculations are based on the idea that a biexciton is composed of two excitons. If the nature of the biexciton is sufficiently different, then a higher level of theory is necessary. The next higher level of theory in this scattering framework would be to use SD-EOM for the one-photon states, and perhaps SDTQ-EOM for the two-photon states. However, it is unknown whether the inclu-

sion of quadruples breaks size consistency. Also, quadruple CI scales as  $N^{16}$ , which limits the calculations to small systems. The scattering formalism presented here is meant to model the behavior two excitons in the limit of long polymer chains in a size-consistent and computationally plausible manner.

The excited-state absorption from the  $1^1B_u$  state is calculated using,<sup>165</sup>

$$\chi^{(1)}(\omega) = \sum_a \frac{2 |\mu_{ba}|^2 E_{ab}}{E_{ab}^2 - (\omega + i\Gamma)^2}, \quad (7.1)$$

where  $b$  is the  $1^1B_u$  state obtained from S-CI theory,  $a$  is summed over all states obtained from the SD-EOM calculation, and  $\Gamma$  sets the linewidth. For the spectra shown in this report,  $\Gamma$  is set to a small value (0.01 eV) to allow all excited states to be resolved.

## 7.2.2 Frenkel Scattering Calculations

In order to interpret the spectra that we obtained from the PPP model (Section 2.3.2), we adopted the method that Spano and coworkers developed for the investigation of exciton-exciton interactions in Frenkel exciton systems.<sup>159-162</sup> An operator that creates a Frenkel exciton on the  $n$ th unit cell is defined as,

$$\hat{F}_n^\dagger = \frac{1}{\sqrt{2}} [a_n^\dagger b_n^\dagger + \bar{a}_n^\dagger \bar{b}_n^\dagger], \quad (7.2)$$

where  $a_n^\dagger$  creates a hole and  $b_n^\dagger$  creates an electron on the  $n^{\text{th}}$  unit cell. The Frenkel Hamiltonian can then be written,

$$\hat{H} = \sum_n \omega \hat{F}_n^\dagger \hat{F}_n - \sum_{n=1}^{N-1} J(\hat{F}_n^\dagger \hat{F}_{n+1} + c.c.) - \sum_{n,m} \frac{E_{\text{exc-exc}}}{|n-m|^3} (\hat{F}_n^\dagger \hat{F}_m^\dagger \hat{F}_m \hat{F}_n), \quad (7.3)$$

where  $\omega$  sets the energy required to create a Frenkel exciton,  $J$  is the nearest neighbor hopping,  $E_{\text{exc-exc}}$  sets the strength of the dipole-dipole like interactions between excitons, and c.c. indicates complex conjugation. This model was parameterized to correspond to the PPP model by setting  $\omega = 6.0$  eV and  $J = 1.75$  eV. The value for  $J$  was chosen based on the bandwidth of the exciton in our previous calculations,<sup>59</sup> (also refer to Section 4.4.5) where the form of the exciton and its motion were segregated.

The energy of this “frozen” exciton was found to be 6.0 eV from these calculations, which gives a bandwidth of 7 eV and  $J = 1.75$  eV. Also note that biexciton formation should depend only on the dimensionless parameter  $E_{\text{exc-exc}}/J$ , which we confirmed by varying  $J$  in the calculations.

### 7.2.3 Contracted Scattering Calculations

In the scattering formalism of Section 7.2.1, S-CI theory is used for the one-photon states and SD-EOM theory is used for the two photon states. With periodic boundary conditions, the number of single electron-hole pair excitations scales as the number of unit cells,  $N$ , and so a complete set of all single excitations is included in both the S-CI and SD-EOM calculations. However, the number of double excitations grows as the third power of the number of unit cells.<sup>1</sup> To make the SD-EOM calculations tractable on long polymer chains, we use the contracted basis functions described in detail in Ref. 58 and Chapter 4 and summarized briefly here. This basis set implements a scattering approach for studying states containing two interacting excitons. We begin by defining an operator that creates a  $1^1B_u$  exciton on the  $n^{\text{th}}$  unit cell,

$$\hat{B}_n^{(K)\dagger} = \frac{1}{\sqrt{2}} \sum_{\delta=-m_{e-h}}^{m_{e-h}} c_{\delta}^{(K)} \left[ a_{n+x_c+\delta/2}^{\dagger} b_{n+x_c-\delta/2}^{\dagger} + \bar{a}_{n+x_c+\delta/2}^{\dagger} \bar{b}_{n+x_c-\delta/2}^{\dagger} \right], \quad (7.4)$$

where  $a_n^{\dagger}$  creates a hole on the  $n^{\text{th}}$  unit cell, and  $b_n^{\dagger}$  creates an electron on the  $n^{\text{th}}$  unit cell. Bars are used to indicate  $\beta$  as opposed to  $\alpha$  electron spin. (This equation is analogous to the finite chain form in Eq. 4.1.) The term in brackets creates a singlet-coupled electron-hole pair separated by  $\delta$  unit cells and centered on the  $n^{\text{th}}$  unit cell if  $\delta$  is even and centered between the  $n^{\text{th}}$  and  $(n+1)^{\text{th}}$  unit cell if  $\delta$  is odd ( $x_c$  is zero if  $\delta$  is even and  $1/2$  if  $\delta$  is odd). The coefficients,  $c_{\delta}^{(K)}$  are determined through an S-CI calculation, with the  $(K)$  superscript indicating that the form of the  $1^1B_u$  exciton depends on the crystal momentum  $K$ . Due to the binding between the electron and hole in an exciton,  $c_{\delta}^{(K)}$  becomes small at large  $|\delta|$ . A local approximation can be

---

<sup>1</sup>Such large basis sets could be handled by direct CI methods, if the goal was to calculate a few low-lying states. However, the goal here is to calculate high-energy states that carry two-photon intensity and direct methods are not readily available.

implemented by setting  $c_\delta^{(K)} = 0$  for  $|\delta| > m_{e-h}$ , as indicated by the limits on the summation in Eq. (7.4).

$\hat{B}_n^{(K)\dagger}$  then corresponds to the creation operator,  $\Omega_n^{(K)\dagger}$  of Eq. (2.21), for a  $1^1B_u$  exciton. The  $1^1B_u$  state arises from the delocalization of this “effective particle”<sup>58,59</sup> as in Eq. (2.21),

$$|1^1B_u\rangle = \frac{1}{\sqrt{N}} \sum_{n=1}^N e^{i(\frac{2\pi}{N})Kn} B_n^{(K)\dagger} |\text{HF}\rangle. \quad (7.5)$$

Here, it will be useful to include basis functions that describe the presence of two excitons on the polymer chain,

$$|2\text{-exciton } \Delta\rangle = \frac{1}{\sqrt{N}} \sum_{n=1}^N \left[ e^{i(\frac{2\pi}{N})(K+K')n} \times \hat{B}_n^{(K)\dagger} \hat{B}_{n+\Delta}^{(K')\dagger} \right] |\text{HF}\rangle, \quad (7.6)$$

which has the form of Eq. (2.21) with  $\Omega_n^{(K)\dagger}$  creating two excitons, one centered on the  $n^{\text{th}}$  unit cell and one centered on the  $(n+\Delta)^{\text{th}}$  unit cell. This basis function describes two excitons separated by  $\Delta$  unit cells and delocalized with a crystal momentum that is the sum of that of the individual excitons,  $K + K'$ .

Eq. (7.6) is referred to as a contracted many-body basis function since it consists of a linear combination of a number of primitive electron-hole excitations. The coefficients of the linear combination are determined during construction of the basis set, via the S-CI calculation of  $c_\delta^{(K)}$  of Eq. (7.4), and are not altered when using this basis set to obtain a variational solution of the Schrodinger equation. The use of contracted functions substantially reduces the number of variational parameters, making it possible to affect a complete diagonalization of the Hamiltonian within the basis.

A scattering formalism is obtained by allowing interactions to alter the form of the excitons when the distance between the excitons is less than or equal to  $n_{\text{scat}}$  unit cells. Therefore,  $n_{\text{scat}}$  sets the size of the scattering region. To describe the excitons outside of the scattering region, the basis set includes the  $|2\text{-exciton } \Delta\rangle$  functions of Eq. (7.6), with  $\Delta = (n_{\text{scat}} + 1) \dots (N - 1)$ . Within the scattering region, we use a more complete basis of primitive electron-hole excitations. This is done by first constructing a primitive basis consisting of all single and double electron-hole pair excitations consistent with a maximum electron-hole pair separation of  $m_{e-h}$ . All

primitives that are already present in the contracted functions ( $|2\text{-exciton } \Delta\rangle$ );  $\Delta = (n_{\text{scat}} + 1) \dots N - 1$ ) are then removed, and the remaining primitive functions provide a basis that describes the excitons within the scattering region. Note that this basis includes interactions between excitons outside the scattering region, and so it simply prevents such interactions from altering the form of the excitons.

When  $n_{\text{scat}} = 0$ , the excited states are written in terms of single excitations and the contracted functions of Eq. (7.6) that describe two excitons separated by various distances. No primitive double electron-hole pair functions are included and thus the interactions between excitons are not allowed to alter their form. This case is then analogous to Frenkel exciton theory, except that the PPP Hamiltonian is used to explicitly calculate the interaction between the excitons. This exciton-exciton interaction is likely to be significantly more complicated than the form used for the Frenkel excitons in Section 7.2.2. For instance, the nature of the Pauli repulsion between excitons may be quite different. For Frenkel excitons, Pauli exclusion prevents the creation of two excitons on one unit cell. In the PPP model, the excitons are extended and, in creating the two-exciton contracted functions, the presence of the electron-hole pair in the first exciton restricts the possible locations of the electron-hole pair in the second exciton. The resulting Pauli exclusion interaction is most likely a repulsive interaction with a longer range than the hard-wall exclusion interactions between Frenkel excitons. If the  $n_{\text{scat}} = 0$  calculations agree with the results obtained with a larger  $n_{\text{scat}}$ , then a Frenkel exciton model could be expected to capture the essentials of this system, although perhaps with a rather complex exciton-exciton interaction potential. To the extent that the  $n_{\text{scat}} = 0$  calculation differs from the converged  $n_{\text{scat}}$  result, the Frenkel exciton approximation is not reliable in these systems.

### 7.3 Results and Discussion

Our main intention for this research was to determine whether spectral signatures of biexcitons exist in the long chain limit. All spectra presented in this section represent absorption from the  $1^1B_u$  state to high-energy two-photon states as described in Section 7.2.1. A peak at or near  $2 \times E_{1^1B_u}$  should appear in each spectrum, repre-

senting two non-interacting excitons. A spectral signature of a biexciton state is the appearance of a state at an energy below  $2 \times E_{1^1B_u}$  whose wavefunction is characteristic of a bound state.

### 7.3.1 Frenkel Excitons

The Frenkel exciton model described in Section 7.2.2 is used as a point of comparison for the PPP Hamiltonian calculations by varying the strength of interactions between the excitons,  $E_{\text{exc-exc}}$  in Eq. (7.3). Calculations were performed on a chain with 71 unit cells and periodic boundary conditions. The calculations indicate that for  $E_{\text{exc-exc}}$  greater than about 3 eV, or  $E_{\text{exc-exc}}/J = 1.7$ , a biexciton state breaks off from the two-exciton continuum. Fig. 7.1 shows the excited state absorption spectra for a range of  $E_{\text{exc-exc}}$ . For all  $E_{\text{exc-exc}}$ , transitions are observed to states at and above  $2 \times E_{1^1B_u}$ . For  $E_{\text{exc-exc}}$  greater than 3 eV, the formation of the biexciton is observed spectrally as a peak below  $2 \times E_{1^1B_u}$ .

Fig. 7.2 shows the analysis of the excited state wavefunctions for the states observed in the spectra for  $E_{\text{exc-exc}} = 2.0$  and 4.5 eV in Fig. 7.1. For  $E_{\text{exc-exc}} = 2.0$  eV, which does not give rise to biexcitons, all wavefunctions are delocalized and the number of nodes increases smoothly with energy. The energy of these states corresponds to a least-squares fit of the particle-in-a-box form expected for unbound excitons ( $E = 2.46 \text{ eV} + 0.021 \text{ eV } n^2$ ;  $n = 1 \dots 5$ ). In the infinite chain limit, the box size becomes infinite, and therefore these states will all collapse onto 2.46 eV, such that the energy required to create an additional exciton is essentially identical to the 2.5 eV required to create the first exciton. For  $E_{\text{exc-exc}} = 4.5$  eV, a biexciton state occurs at 2.09 eV and the wavefunction indicates binding between the excitons with an average separation of about two to three unit cells. For the higher-energy states, the wavefunction is delocalized over the entire chain, with the 2.50 eV state having two nodes ( $m_{\text{exc-exc}} = 0$  and 3) and the number of nodes increases smoothly with increasing state energy. These higher energy levels fit a particle-in-a-box form ( $E = 2.46 \text{ eV} + 0.026 \text{ eV } n^2$ ) with  $n = 1$  being the 2.50 eV state. Just as for

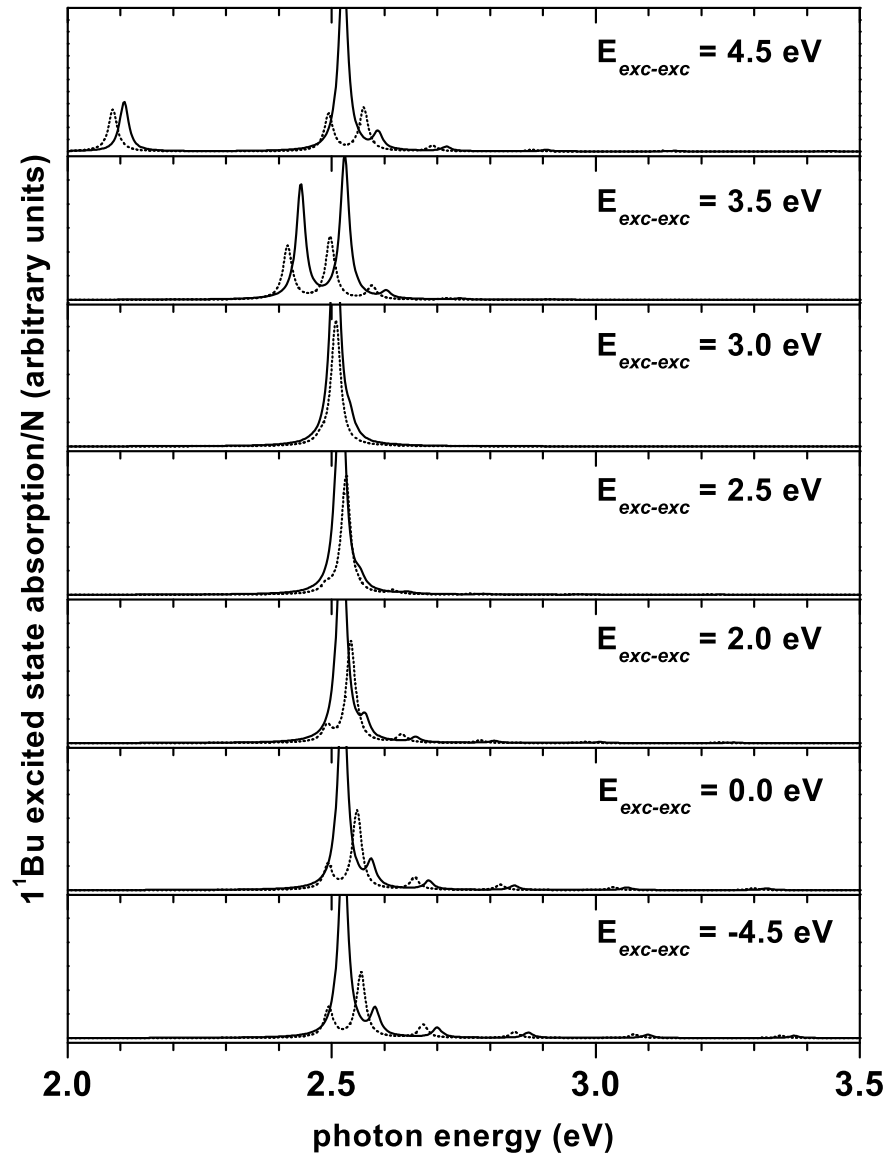


**Figure 7.1:** Excited-state absorption from the  $1^1B_u$  one-exciton state, for long chain Frenkel excitons with various  $E_{\text{exc-exc}}$ , using periodic boundary conditions and  $N = 71$ . The dotted line is  $K = 0$ , and the solid line is  $K = 2$ . The units of intensity are the same for all panels.

$E_{\text{exc-exc}} = 2.0$  eV, these states all converge onto 2.46 eV in the limit of an infinite chain.

Similar results are obtained from Frenkel exciton calculations on finite linear chains. Fig. 7.3 shows the  $1^1B_u$  excited state absorption spectra for various chain lengths with and without biexciton formation,  $E_{\text{exc-exc}} = 4.5$  eV and 2.0 eV, respectively. For  $E_{\text{exc-exc}} = 2.0$  eV, an intense transition to a state containing two unbound excitons approaches  $2 \times E_{1^1B_u}$  from above. A number of states are also observed at higher energy, with intensity patterns that are not easily interpreted. For instance, these states do not fit the particle-in-a-box model used above for periodic boundary condition calculations on  $N = 71$  chains. These complications likely arise from a complex interplay of finite-chain boundary conditions and the exciton-exciton potential. For  $E_{\text{exc-exc}} = 4.5$  eV, the lowest energy transition shown corresponds to a biexciton, as confirmed by analysis of the wavefunction. The energy of the biexciton state is relatively independent of chain length. Comparison of the  $E_{\text{exc-exc}} = 2.0$  and 4.5 eV spectra reveals that the biexciton state is borrowing its intensity from the unbound two-exciton state. On short polyenes,  $N = 9$  in Fig. 7.3, the biexciton carries essentially all of the intensity and the relative intensity to the two-exciton state increases rapidly with chain length. Just as for  $E_{\text{exc-exc}} = 2.0$  eV, the unbound two-exciton state approaches  $2 \times E_{1^1B_u}$  from above, but the  $E_{\text{exc-exc}} = 4.5$  eV results show a much stronger dependence on chain length.

In comparing intensities, it is important to note that the intensities of the bound and free exciton states should scale differently with chain length in the long-chain limit.<sup>157</sup> The transition from a state with one exciton to a state with two unbound excitons corresponds to creation of an additional free exciton. Since there are  $N - 1$  locations for this second exciton on a chain with  $N$  unit cells, the intensity should scale as  $N$  in the long chain limit. This is not the case for the bound biexciton state, where the second exciton must be created next to the first exciton and so the number of possible locations is independent of chain length. (In effect, the biexciton acts a single effective particle and the transition corresponds to a conversion of the exciton into a biexciton, as opposed to the creation of an additional effective particle.) The transition from the  $1^1B_u$  state to the biexciton state thus has an intensity that is

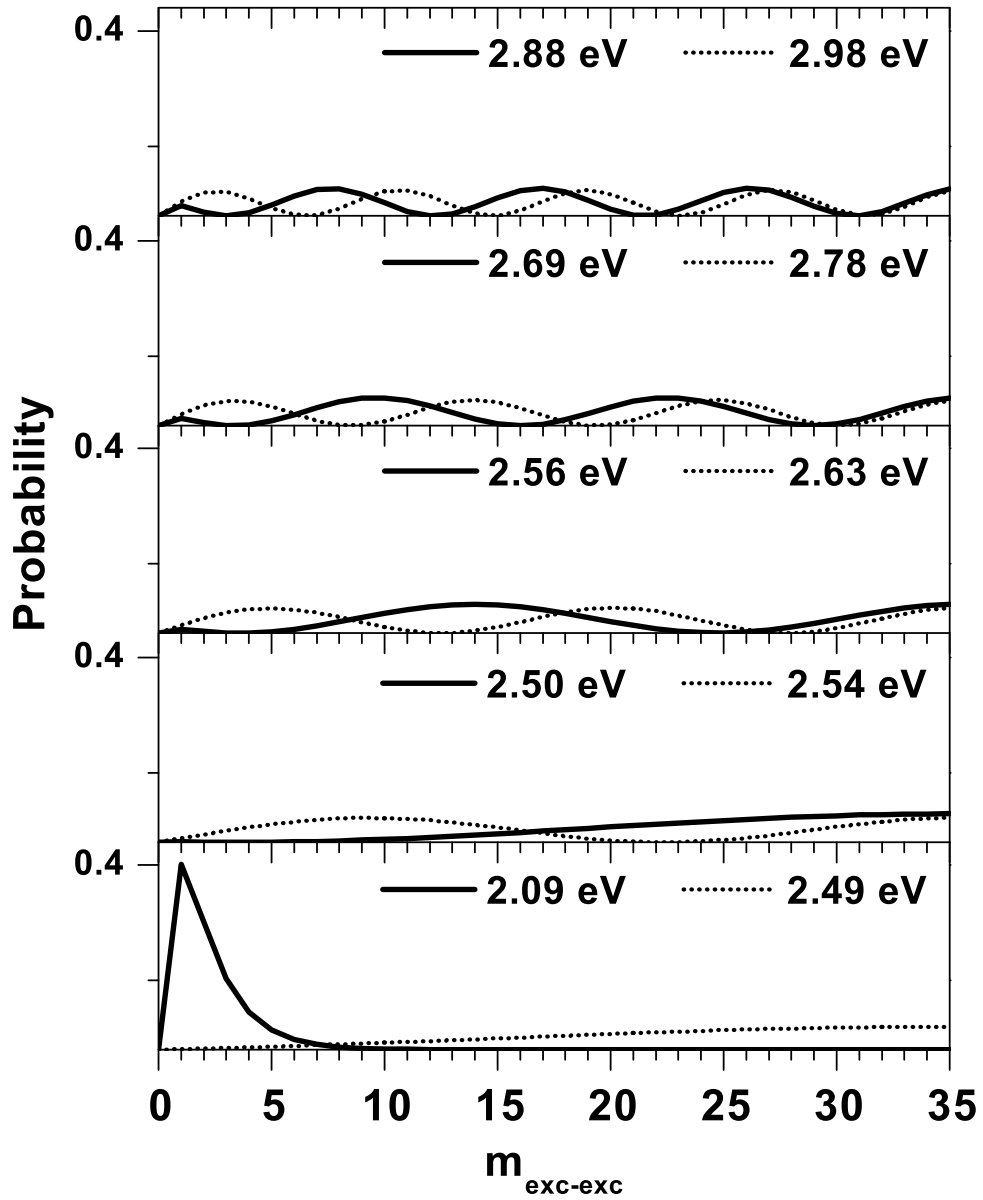


**Figure 7.2:** Analysis of the wavefunctions for the states giving rise to the transitions in the spectra in Fig. 7.1 for  $E_{\text{exc-exc}} = 4.5$  (solid line) and 2.0 (dotted line). The  $K = 2$  wavefunctions have the same form as  $K = 0$ . The probability density is shown as a function of exciton-exciton separation,  $m_{\text{exc-exc}}$ .

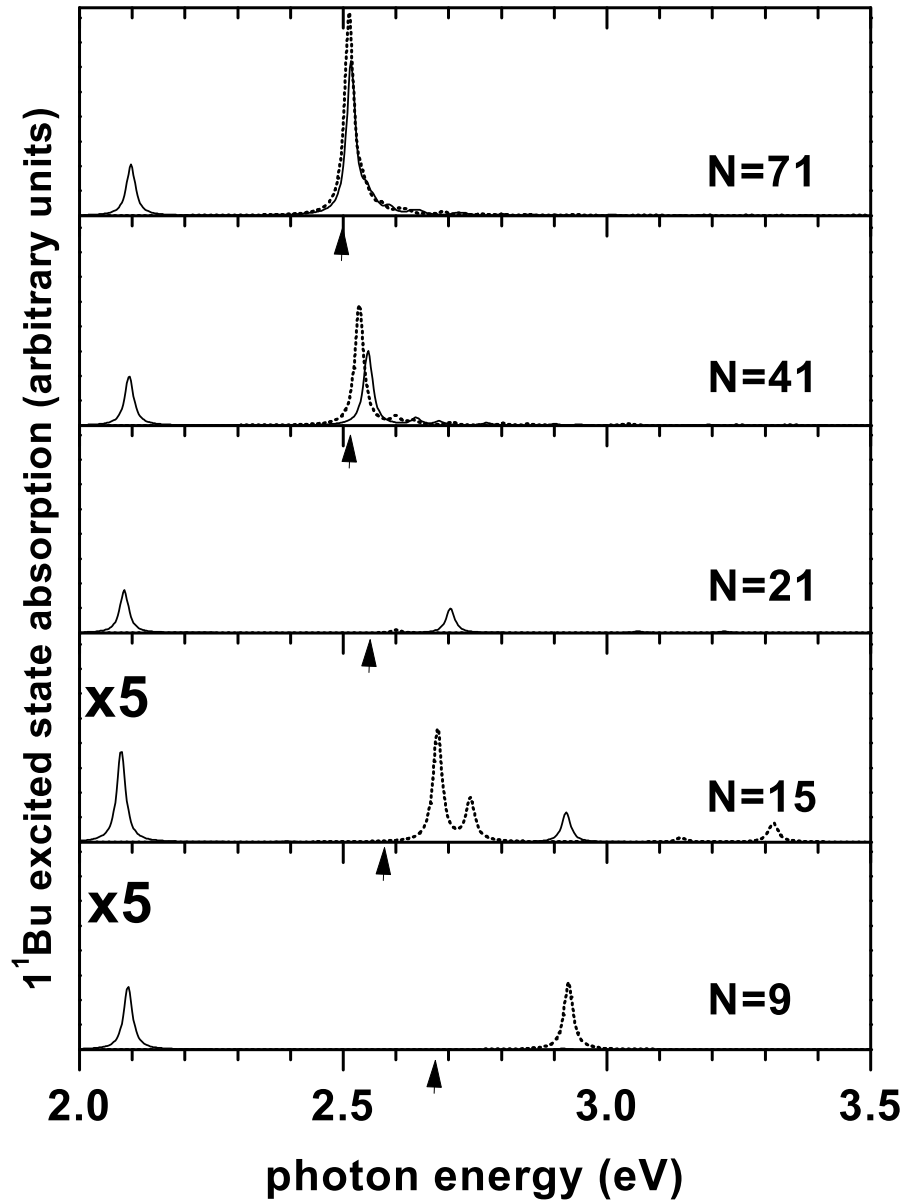


**Figure 7.3:** Excited-state absorption from the  $1^1B_u$  state, for a Frenkel exciton system with  $E_{\text{exc-exc}} = 4.5$  (solid line) and  $2.0$  (dotted line) and  $N$  unit cells. The  $1^1B_u$  state energies are indicated by arrows. To allow comparison with chain length, the scale of the axes is the same for all panels, such that a constant height indicates the intensity is linearly dependent on chain length.

independent of chain length in the long-chain limit. The spectra in Fig. 7.3 indicate that the biexciton carries significant intensity relative to  $2 \times E_{1^1B_u}$  on short chains, and the intensity saturates by about 21 unit cells. The transitions above  $2 \times E_{1^1B_u}$  are weak on short chains, and the intensity increases rapidly with chain length. On chains with greater than about 41 unit cells, the intensity begins to scale as  $N$ , as expected in the long chain limit.

The Frenkel exciton results of Fig. 7.1 allow us to examine the implications of using periodic boundary conditions within a well-understood model. This insight is useful since we must use periodic boundary conditions in order to investigate the long-chain limit of the PPP Hamiltonian. Fig. 7.1 shows a rather substantial difference between the  $K = 0$  and  $K = 2$  spectra, particularly in the region near  $2 \times E_{1^1B_u}$ . The splitting between the  $K = 0$  and  $K = 2$  transitions for the biexciton transition are as expected for a system in which the biexciton states form a band with a minimum at  $K = 0$ . However, in the vicinity of  $2 \times E_{1^1B_u}$ , the  $K = 0$  and  $K = 2$  spectra show differences that are not as easily rationalized. For instance, it is not clear why the lowest two peaks near  $2 \times E_{1^1B_u}$  carry very different intensities for the  $K = 0$  versus  $K = 2$  spectra. Similar effects are observed in the PPP results of Section 7.2.3, and we take their presence within the Frenkel exciton model as evidence that this spectral feature is not indicative of complex exciton-exciton interactions. In particular, large difference between the  $K = 0$  and  $K = 2$  spectra are observed even for Frenkel excitons with no interactions ( $E_{exc-exc} = 0$ ) and with repulsive interactions ( $E_{exc-exc} = -4.5$  eV). Also note that these are small splittings in a spectral region that will be dominated by one-photon absorption, and so are of no apparent experimental interest.

In summary, the results for Frenkel excitons indicate that excited-state absorption provides a good probe of biexciton formation. The biexciton appears as an intense transition below  $2 \times E_{1^1B_u}$  and exhibits only weak chain-length dependencies.

### 7.3.2 PPP Oligomers

Fig. 7.4 shows excited-state absorption spectra for polyenes with between 4 and 9 unit cells. These were obtained using the scattering methodology of Section 7.2.1

with complete S-CI and SD-EOM basis sets. Comparison of these spectra in the region near  $2 \times E_{1^1B_u}$  with that obtained for Frenkel excitons reveals a somewhat different behavior. Just as for Frenkel excitons, the most intense transition approaches  $2 \times E_{1^1B_u}$  from above, but here it drops below  $2 \times E_{1^1B_u}$  for chains with 7 or more unit cells. In addition, the states closest to  $2 \times E_{1^1B_u}$  have nearly 50% single electron-hole pair character. A state is observed below  $2 \times E_{1^1B_u}$  with greater than 80% double electron-hole pair character. While this is suggestive of a biexciton, its energy is dropping rapidly with chain length, unlike the Frenkel exciton model. The following calculations on long chains provide more insight into the behavior and stability of biexciton states.

### 7.3.3 Long PPP Chains

In this section, we consider solutions of the PPP Hamiltonian on long chains of polyacetylene, using periodic boundary conditions and the scattering basis set of Section 7.2.3. In this basis,  $n_{\text{scat}}$  sets the size of the scattering region within which exciton-exciton interactions are allowed to alter the form of the excitons. The one-photon states in these calculations are calculated differently than the finite chain calculation presented above, which will give a slight difference in the  $1^1B_u$  energies indicated in the spectra. These calculations represent the one-photon states under periodic boundary conditions as an “effective particle” depicted by Eq. 7.5, and a local approximation of  $m_{e-h} = 5$  has been implemented. In contrast, the one-photon states in Section 7.3.2 are represented by a complete S-CI basis.

The convergence of the calculations with respect to the size of the scattering region,  $n_{\text{scat}}$ , is depicted in Fig. 7.5. The spectra are well-converged by  $n_{\text{scat}} = 9$ . Although the higher energy transitions move about slightly in energy between  $n_{\text{scat}} = 5$  and 9, their intensities and relative positions are well-established. The additional peaks around 2.3 eV in the  $n_{\text{scat}} = 2$  spectrum occur from a dark state that mixes strongly with the background single electron-hole pair configurations. These peaks disappear in D-EOM calculations, which do not include single electron-hole pair configurations in the calculation of the two-photon states. The results obtained for  $n_{\text{scat}} = 0$

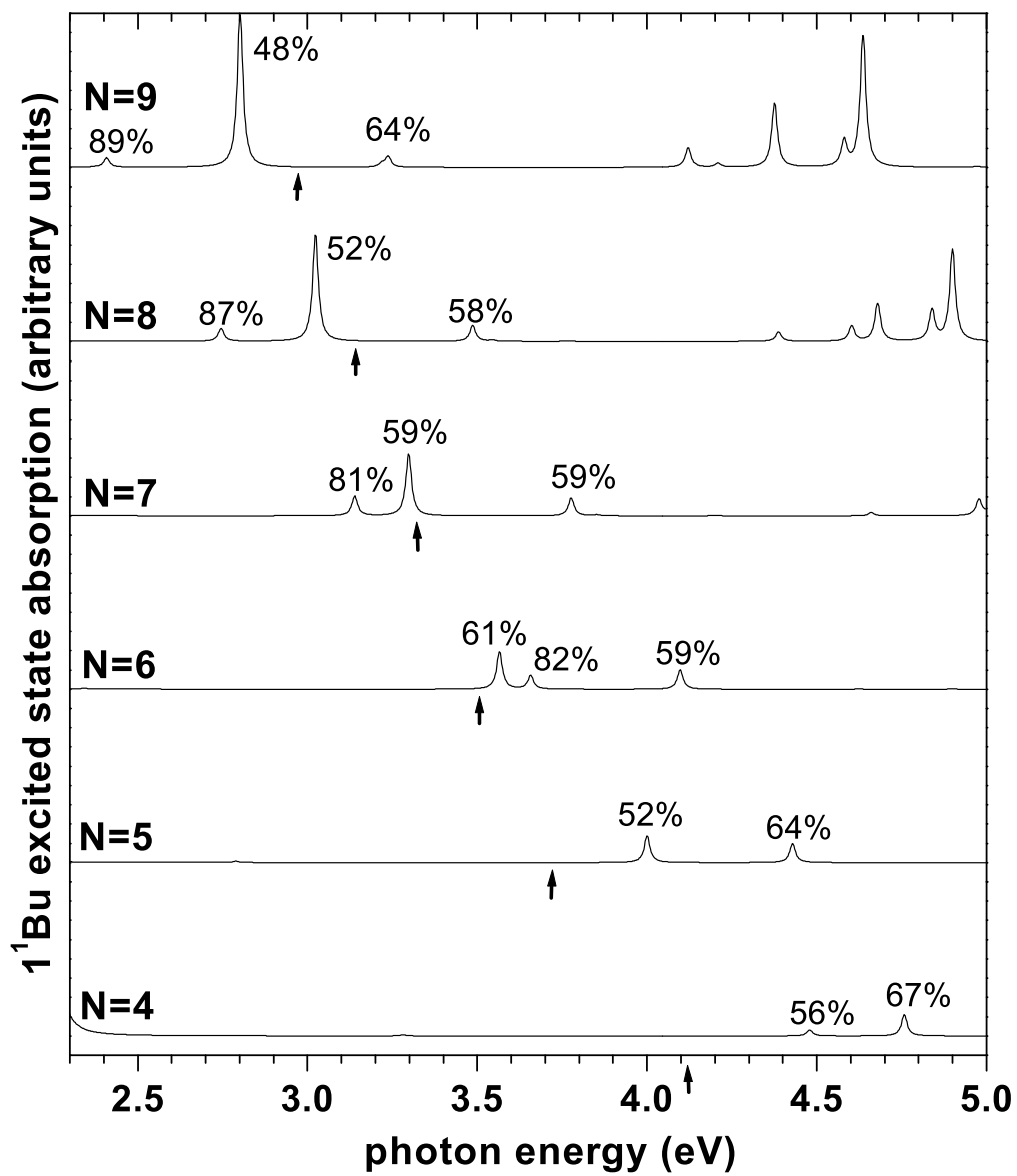


**Figure 7.4:** Excited-state absorption for polyenes with  $N$  unit cells. The  $1^1B_u$  state energies are indicated by arrows. The numbers above the peaks indicate the relative contribution of double electron-hole pair configurations to the relevant excited state.

do not agree with those for larger  $n_{\text{scat}}$ , which indicates that the interactions between excitons alters their form. As discussed in Section 7.2.3, this suggests that the Frenkel exciton approximation is not sufficient for these systems.

Fig. 7.6 shows the excited-state absorption spectra obtained for  $n_{\text{scat}} = 9$  on various chain lengths, and Table 7.1 gives the energies and the relative composition of single and double electron-hole pair configurations for each peak in the spectra. In considering the chain length dependence of the spectra, it is important to remember that the use of periodic boundary conditions on short chains is useful only as a means of extrapolation to the long-chain limit. Spectral features that do not persist in the limit of long chains can be artifacts of the boundary conditions, especially when large differences are observed between  $K = 0$  and  $K = 2$ , as is the case for some of the spectral features in Fig. 7.6. These spectra are strongly dependent on chain length below 51 unit cells, but appear reasonably well converged by 71 unit cells.

The most intense transitions in the spectra for 71 unit cells occur to states near  $2 \times E_{1^1B_u}$  for both  $K = 0$  (2.57 eV) and  $K = 2$  (2.63 eV). Fig. 7.7 shows an analysis of the wavefunctions for the states giving rise to the transitions in the spectra for 71 unit cells. Since most of the probability density for these intense transitions lies at large exciton-exciton separation distances, these states are comprised of two unbound excitons. The most significant result is the absence of spectral features below these transitions, which is a strong indication that this system does not support spectral biexciton states in the limit of long chains.

The behavior of the  $2 \times E_{1^1B_u}$  transition is different for  $K = 0$  and  $K = 2$  in Fig. 7.6; the most intense  $K = 2$  transition approaches  $2 \times E_{1^1B_u}$  from above while the most intense  $K = 0$  transition approaches  $2 \times E_{1^1B_u}$  from below. This difference can be rationalized in terms of the selection rule for  $K$  (Section 2.5). Since the one-photon  $1^1B_u$  state contains a single  $K = 1$  exciton,  $2 \times E_{1^1B_u}$  is the energy required for creation of two  $K = 1$  excitons, or a two-exciton state with  $K = 2$ . The difference between  $2 \times E_{1^1B_u}$  and the unbound two-exciton state with  $K = 2$  therefore arises only from excluded volume interactions between excitons. The excluded volume effect causes the  $K = 2$  transition to approach  $2 \times E_{1^1B_u}$  from higher energy. The difference between the  $K = 0$  and  $K = 2$  unbound two-exciton states arises from the band

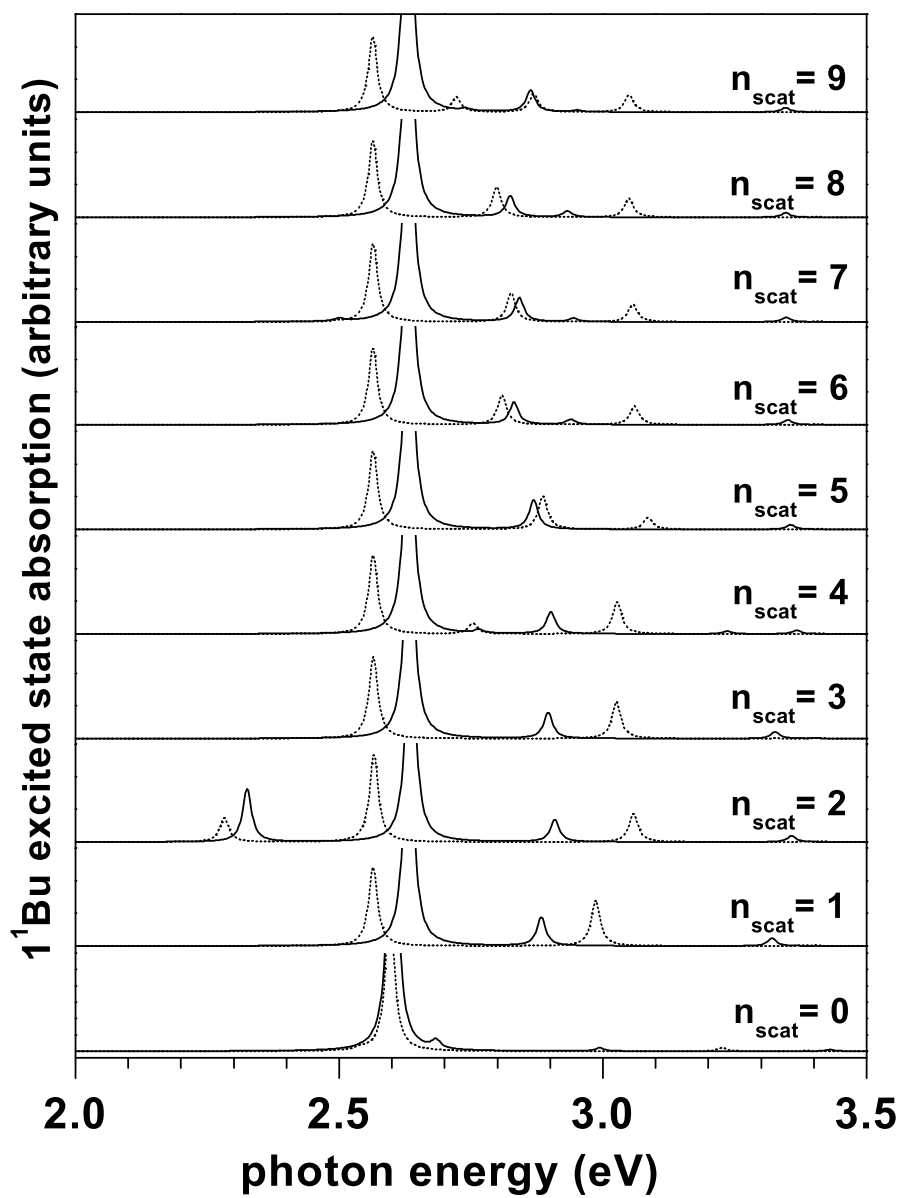


*Figure 7.5:* Excited state absorption from the  $1^1B_u$  state obtained for periodic polyacetylene chains with 71 unit cells and the indicated scattering regions,  $n_{\text{scat}}$ . The dotted line is  $K = 0$ , and the solid line is  $K = 2$ .

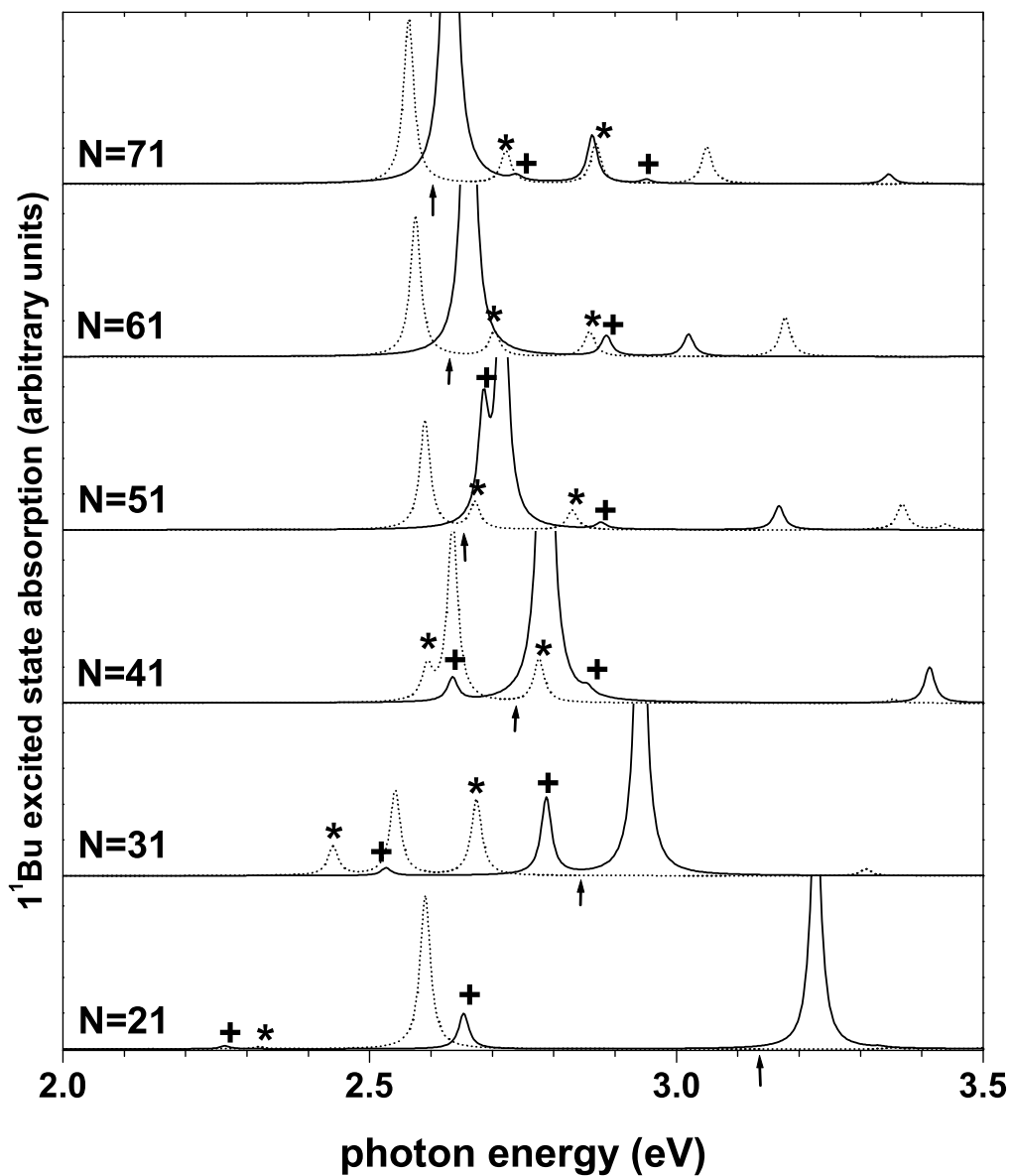


**Figure 7.6:** Excited state absorption from the  $1^1B_u$  state obtained for periodic polyacetylene chains with  $N$  unit cells and a scattering region of  $n_{\text{scat}} = 9$ . The arrows indicate the  $1^1B_u$  state energies, hence where the  $2 \times E_{1^1B_u}$  peak is expected. The dotted line is  $K = 0$ , and the solid line is  $K = 2$ . The marked peaks are explained in the text.

**Table 7.1:** Analysis of the wavefunctions giving rise to the transitions in the spectra of Fig. 7.6. The relative probabilities are listed for single electron-hole pair configurations (% singles) and for double electron-hole pair configurations within ( $<n_{\text{scat}}$ ) and outside ( $>n_{\text{scat}}$ ) of the scattering region. The  $K = 0$  and the corresponding  $K = 2$  peaks are aligned in the table.

N	K = 0				K = 2			
	E(eV)	%sing	%doub $<n_{\text{scat}}$	%doub $>n_{\text{scat}}$	E(eV)	%sing	%doub $<n_{\text{scat}}$	%doub $>n_{\text{scat}}$
71	2.57	0.3	0.4	99.3	2.63	0.6	1.6	97.8
	2.72(*)	37.8	58.2	4.0	2.74(+)	40.0	64.0	5.0
	2.87(*)	22.3	66.4	11.3	2.95(+)	30.9	34.4	34.6
	3.05	16.2	26.0	57.8	2.86	9.5	36.7	53.8
61	2.58	0.6	0.8	98.6	2.66	1.8	3.7	94.5
	2.70(*)	37.1	60.6	2.3	2.88(+)	31.7	54.7	13.6
	2.86(*)	29.8	66.7	3.5				
	3.18	11.1	34.7	54.2	3.02	11.6	16.5	71.9
51	2.59	2.1	2.5	95.4	2.72	3.0	16.5	80.5
	2.67(*)	34.9	61.2	3.9	2.68(+)	24.0	60.5	15.5
	2.83(*)	33.9	64.7	1.4	2.80(+)	41.5	54.1	4.4
	3.37	34.0	38.8	27.2	3.16	5.5	21.5	73.0
	3.44	72.7	16.2	11.1				
41	2.59(*)	26.0	37.4	36.6	2.63(+)	22.8	76.7	0.5
	2.64	10.2	29.9	59.9	2.79	4.5	13.8	81.7
	2.77(*)	36.8	60.7	2.5	2.86(+)	42.8	44.4	12.8
					3.41	9.1	36.1	54.8
31	2.44(*)	28.9	33.9	37.2	2.53(+)	17.9	82.1	0.0
	2.54	9.3	54.9	35.8	2.79(+)	50.2	48.4	1.4
	2.67(*)	38.6	47.7	13.7	2.95	2.1	14.6	83.3
	3.31	66.7	33.3	0.0				
21	2.32(*)	14.3	83.2	2.5	2.27(+)	13.2	86.8	0.0
					2.65(+)	54.9	45.1	0.0
	2.59	16.4	47.7	35.9	3.23	1.2	54.9	43.9

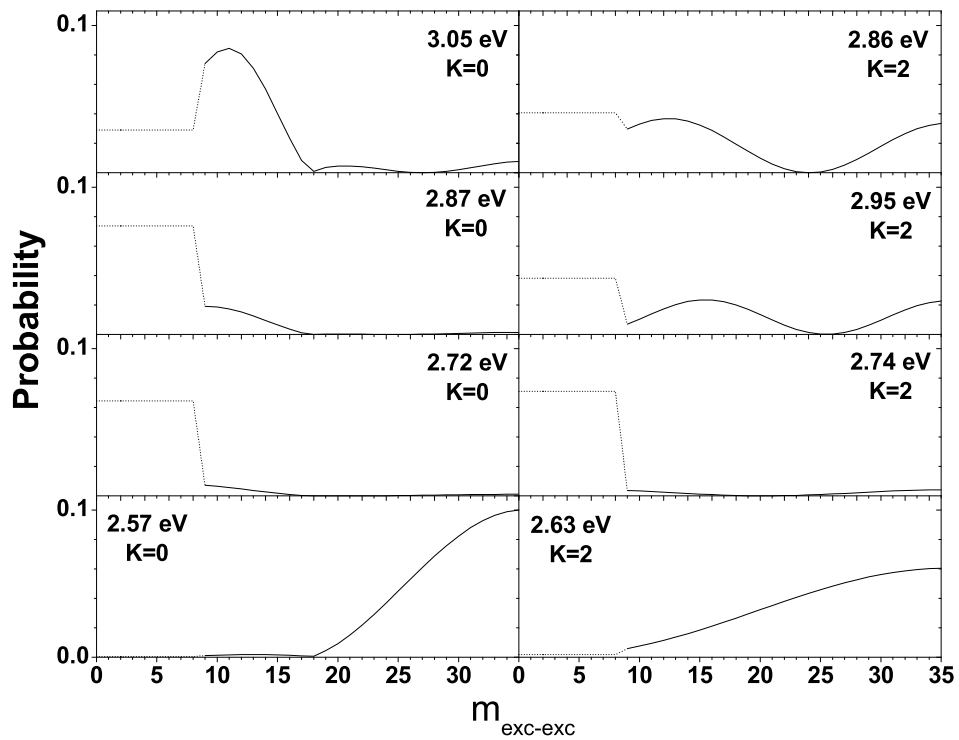


**Figure 7.7:** Analysis of the wavefunctions for the states giving rise to the transitions in the  $N = 71$  spectrum of Fig. 7.6. The probability density is shown as function of exciton-exciton separation,  $m_{\text{exc-exc}}$ . The dotted lines show the average probabilities within the scattering region. (Note that the probabilities due to single electron-hole configurations are not included.)

width of the exciton. While this difference also approaches zero in the limit of long chains, it is a larger effect than the excluded-volume effect and so the  $K = 0$  transition approaches  $2 \times E_{1^1B_u}$  from lower energy.

Fig. 7.8 shows the spectra obtained when only double electron-hole pair configurations (D-EOM) are included in the calculation of the two-photon states, which can be used to understand the extent of mixing between single and double electron-hole pair configurations. The inclusion of single electron-hole pair configurations in Fig. 7.6 has little effect on the intense  $2 \times E_{1^1B_u}$  transitions in the long-chain limit. For  $N = 61$  and  $71$ , these states have greater than 98% double electron-hole pair character. On shorter chains, the inclusion of single electron-hole pair configurations does have some effects on these transitions, which will be discussed in more detail below.

The  $K = 2$  spectra in Fig. 7.6 exhibit a higher-energy transition that behaves similarly to the higher-energy transitions of the Frenkel exciton model. For  $N = 41$ ,  $51$ ,  $61$ , and  $71$ , this transition occurs at  $3.41$ ,  $3.16$ ,  $3.02$ , and  $2.86$  eV, respectively, corresponding to a gradual decrease in state energy. These transitions are to states with greater than 90% double electron-hole pair character, and persist in the D-EOM spectra in Fig. 7.8 with a slight shift in energies and intensities. The analysis of the wavefunction in Fig. 7.7 for the  $2.86$  eV transition at  $N = 71$  shows a nodal pattern similar to that seen for the second-highest unbound exciton state in the Frenkel model in Fig. 7.2. The  $K = 0$  spectrum also exhibits a similar transition that decreases rapidly with chain-length, with energies  $3.37$ ,  $3.18$ , and  $3.05$  eV for  $N = 51$ ,  $61$  and  $71$  respectively. Although this state is also comprised of about 90% double electron-hole pair character, it differs a bit from the  $K = 2$  state in that the wavefunction has two nodes outside of the scattering region. Nevertheless, by analogy with similar states in the Frenkel exciton spectrum, we expect these higher-energy unbound exciton states to converge onto the lowest-energy unbound exciton states in the limit of an infinite chain.

Other high-energy features of the spectra in Fig. 7.6 have interesting behavior. There are two peaks marked with a (\*) in each  $K = 0$  spectrum in Fig. 7.6. The wavefunction analysis in Fig. 7.7 of these transitions for  $N = 71$  at energies  $2.72$  and  $2.87$  eV reveals that the probability density arising from the double electron-hole pair

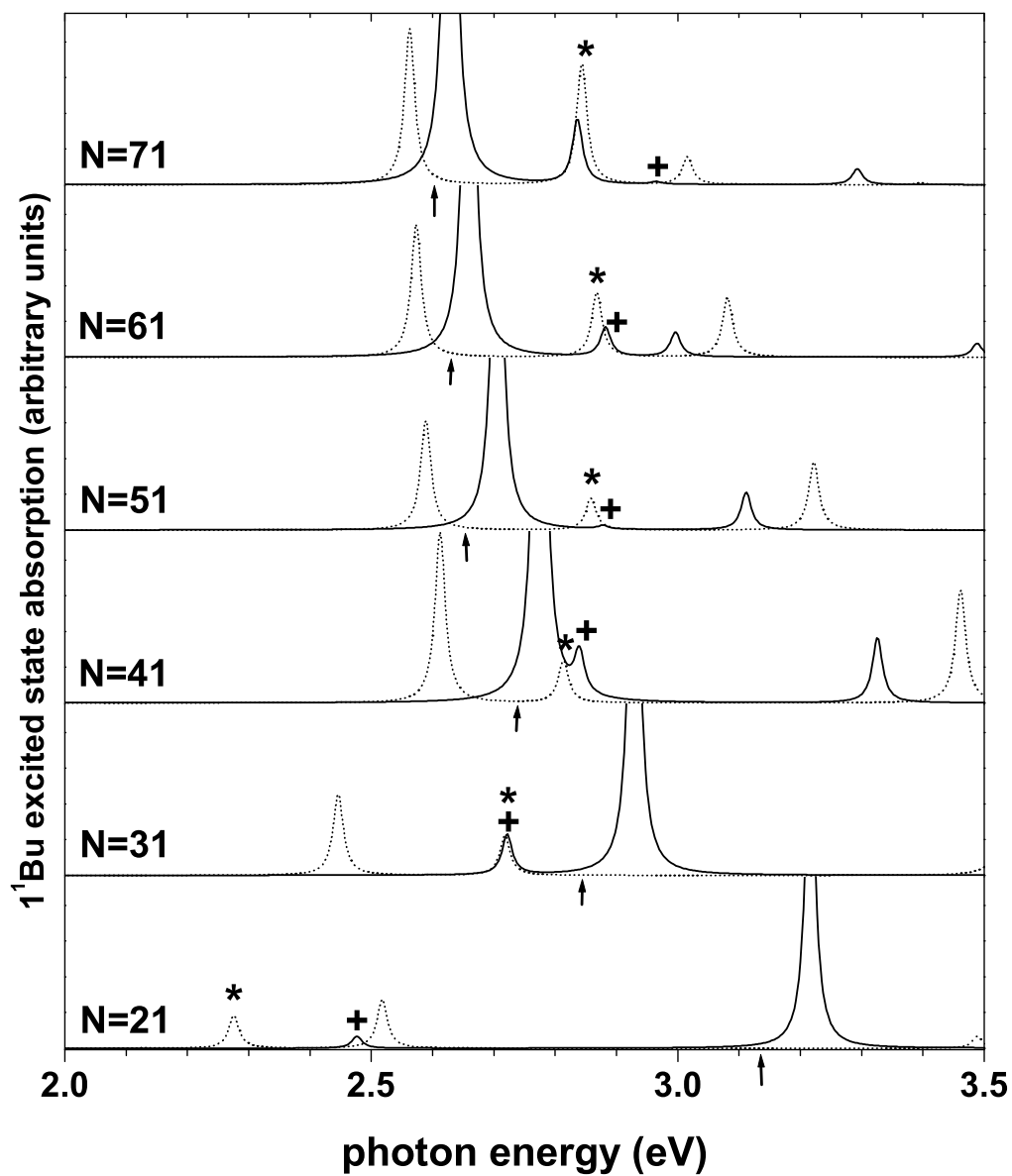


*Figure 7.8:* Same as Fig. 7.6, but without inclusion of single electron-hole pair configurations in the calculation of the two-photon excited states (D-EOM).

configurations lies predominantly in the scattering region, which indicates that these states are comprised of two overlapping excitons. The upper of these two transitions is 0.25 eV above the unbound two-exciton transition, and so may be experimentally observable, especially in a well-ordered material such as polydiacetylene. Similar peaks, marked with a (+), are also found in the  $K = 2$  spectra, except their intensity behaves somewhat differently.

Table 7.1 reveals that these overlapping exciton peaks, marked with a (\*) for  $K = 0$  and a (+) for  $K = 2$ , are comprised of a significant amount of single electron-hole pair configurations, between 20-40%. Each of the D-EOM spectra in Fig. 7.8 only has a single overlapping exciton peak, which indicates that the overlapping exciton state mixes strongly with single electron-hole pair configurations, leading to the two transitions in the SD-EOM spectra in Fig. 7.6.

The interesting chain length behavior of these overlapping exciton transitions is apparent in Figs. 7.6 and 7.8. As the chain length decreases, the energy of these transitions decreases, while the energy of the  $2 \times E_{1^1B_u}$  transition increases. Eventually the overlapping exciton state crosses the  $2 \times E_{1^1B_u}$  state as the chain length decreases, causing a state with overlapping exciton character to be lower in energy than the  $2 \times E_{1^1B_u}$ . Table 7.1 shows how the composition of double electron-hole pair configurations within the scattering region of these peaks also changes with chain length. For  $K = 2$ , the percentage for the lower energy peak increases as it drops lower in energy than the  $2 \times E_{1^1B_u}$  (from 64.0% for  $N = 71$  to 76.7% for  $N = 41$ ), indicating that the overlapping excitons are becoming more bound. For  $K = 0$ , a similar trend is found. However, in the  $N = 41$  and  $N = 31$  spectra for  $K = 0$  where the overlapping exciton transition is crossing the  $2 \times E_{1^1B_u}$  transition, there is a decrease in the percentage of double electron-hole configurations within the scattering region and an increase in those outside the scattering region, which indicates that the two free exciton state and the overlapping exciton state are mixing. As discussed earlier, the differences between the behavior of the  $K = 0$  and  $K = 2$  spectra are greater for shorter chain lengths, especially for the position of the  $2 \times E_{1^1B_u}$  peak relative to the  $1^1B_u$  state energy, which is an artifact of the boundary conditions. Despite the different behavior of the  $K = 0$  and  $K = 2$  spectra on shorter chain lengths, their

overall result is the same: the growth of a bound state below the  $2 \times E_{1^1B_u}$  in shorter chains, which can be attributed to confinement effects due to their finite size.

How about the nature of these overlapping exciton states above  $2 \times E_{1^1B_u}$ ? If these states do arise from overlapping excitons, their location above the energy of two free excitons is indicative of a scattering resonance rather than a biexciton. Alternatively, it may be that these states are not best viewed as containing overlapping excitons, and instead contain some other type of two-photon allowed effective particle.

## 7.4 Summary

The calculations presented here provide strong evidence that long-chain conjugated polymers do not support biexciton states.

The Frenkel exciton model provides a good benchmark to verify the approach used here to identify biexcitons. In the Frenkel model, there is a critical exciton-exciton interaction strength above which a biexciton state is formed. This biexciton state has an energy below that of  $2 \times E_{1^1B_u}$  and carries significant intensity from the  $1^1B_u$  state.

The PPP Hamiltonian of polyacetylene serves as a two-band model of conjugated polymers. On polyenes with between 7 and 9 unit cells, states are observed below  $2 \times E_{1^1B_u}$  that are dominated by double electron-hole pair configurations. While this is suggestive of a biexciton state, the energy of the state is dropping rapidly with chain length, unlike in the Frenkel exciton model where the biexcitons are relatively independent of chain length.

The existence of a biexciton state in the long-chain limit was investigated using periodic boundary conditions and the scattering methodology discussed above. When the size of the scattering region is set to zero, the scattering formalism is analogous to a Frenkel exciton model in that exciton-exciton interactions are not allowed to alter the form of the excitons. However, it differs from the Frenkel model in that it uses the PPP Hamiltonian to explicitly calculate the exciton-exciton interactions. In addition, it includes the finite size of the excitons and the resulting Pauli-exclusion interactions between excitons. Within this zero-scattering-region approximation, the lower energy

states show a build-up of probability near zero exciton-exciton separation, suggesting an attraction between excitons. However, formation of biexciton states is not observed, indicating that the attraction, if present, is not sufficient to lead to a binding between excitons.

As the size of the scattering region is increased, exciton-exciton interactions are allowed to alter the form of the excitons. Convergence is observed for a scattering region of about 9 unit cells. The need for a large scattering region and the significant difference between a scattering region of size 0 and 9 indicates that a Frenkel model, even with an explicitly calculated exciton-exciton potential, is not adequate to describe exciton-exciton interactions in these systems since it does not allow the excitons to change their form as they interact.

The principal result of the converged scattering calculations is the absence of a biexciton state in the long chains. This is in contrast to the results obtained for oligomers with up to 9 unit cells and the periodic calculations on chains up to 31 unit cells, which did exhibit states suggestive of biexcitons, i.e. states with predominantly double electron-hole pair character and with energies a few tenths of an eV below  $2 \times E_{1^1B_u}$ . Since the biexcitonic character of these states only appears in short chains, their presence is rationalized to be due to confinement effects.

Transitions are observed to states above  $2 \times E_{1^1B_u}$  which have a large contribution from double electron-hole pair configurations with overlapping electron-hole pairs. The observed energy being above  $2 \times E_{1^1B_u}$  is suggestive of a scattering resonance rather than a bound biexciton state.

# Bibliography

1. Marko Strukelj, Fotis Papadimitrakopoulos, Timothy M. Miller, and Lewis J Rothberg. Design and application of electron-transporting organic materials. *Science (Washington, D. C.)*, 267:1969, 1995.
2. R. H. Friend, R. W. Gymer, A. B. Holmes, J. H. Burroughes, R. N. Marks, C. Taliani, D. D. C. Bradley, D. A. DosSantos, J.-L. Bredas, M. Logdlund, and W. R. Salaneck. Electroluminescence in conjugated polymers. *Nature*, 397:121, 1999.
3. G. Kranzelbinder, M. Nisoli, S. Stagira, S. De Silvestri, G. Lanzani, K. Mullen, U. Scherf, W. Graupner, and G Leising. Cooperative effects in blue light emission of poly(para-phenylene)-type ladder polymer. *Appl. Phys. Lett.*, 71:2725, 1997.
4. U. Mitschke and P. Bauerle. The electroluminescence of organic materials. *Journal of Materials Chemistry*, 10:1471, 2000.
5. Rainer E. Martin, Florence Geneste, Robert Riehn, Beng Sim Chuah, Franco Cacialli, Andrew B. Holmes, and Richard H. Friend. Efficient electroluminescent poly(p-phenylene vinylene) copolymers for application in LEDs. *Synth. Met.*, 119:43, 2001.
6. N. Tessler, G. J. Denton, and R. H. Friend. Lasing from conjugated-polymer microcavities. *Nature*, 382:695, 1996.
7. F. Hide, M. A. Diaz-Garcia, B. J. Schwartz, M. R. Andersson, Q. Pei, and A. J. Heeger. Semiconducting polymers: a new class of solid-state laser materials. *Science*, 273:1833, 1996.
8. F. Hide, M. A. Diaz-Garcia, B. J. Schwartz, and A. J. Heeger. New developments in the photonic applications of conjugated polymers. *Acc. Chem. Res.*, 30:430, 1997.

9. Takashi Kondo, Takashi Azuma, Takashi Yuasa, and Ryoichi Ito. Biexciton lasing in the layered perovskite-type material  $(\text{C}_6\text{H}_{13}\text{NH}_3)_2\text{PbI}_4$ . *Solid State Commun.*, 105:253, 1997.
10. Nir Tessler. Lasers based on semiconducting organic materials. *Adv. Mater. (Weinheim, Ger.)*, 11:363, 1999.
11. N. Tessler, D. J. Pinner, V. Cleave, P. K. H. Ho, R. H. Friend, G. Yahiolu, P. Le Barny, J. Gray, M. de Souza, and G Rumbles. Properties of light emitting organic materials within the context of future electrically pumped lasers. *Synth. Met.*, 115:57, 2000.
12. J. H. Burroughes, D. D. C. Bradley, A. R. Brown, R. N. Marks, K. Mackay, R. H. Friend, P. L. Burns, and A. B. Holmes. Light-emitting diodes based on conjugated polymers. *Nature*, 347:539, 1990.
13. G. Gustafsson, Y. Cao, G. M. Treacy, F. Klavetter, N. Colaneri, and A. J. Heeger. Flexible light-emitting diodes made from soluble conducting polymers. *Nature*, 357:477, 1992.
14. Vladimir V. Grushin, Norman Herron, Daniel D. LeCloux, William J. Marshall, Viacheslav A. Petrov, and Ying Wang. New, efficient electroluminescent materials based on organometallic Ir complexes. *Chem. Commun.*, 16:1494, 2001.
15. A. Kraft, P. L. Burn, A. B. Holmes, D. D. C. Bradley, A. R. Brown, R. H. Friend, and R. W Gymer. Chemical control of color and electroluminescent device efficiency in copolymeric poly(arylenevinylenes). *Synth. Met.*, 55:936, 1993.
16. H. Kobayashi, S. Kanbe, S. Seki, H. Kigchi, M. Kimura, I. Yudasaka, S. Miyashita, T. Shimoda, C. R. Towns, J. H. Burroughes, and R. H. Friend. A novel RGB multicolor light-emitting polymer display. *Synth. Met.*, 111:125, 2000.
17. Heinrich Becker, Olaf Gelsen, Edgar Kluge, Willi Kreuder, Hermann Schenk, and Hubert Spreitzer. Development of high performance PPVs: implications of the polymer-microstructure. *Synth. Met.*, 111:145, 2000.
18. M. Yan, L. J. Rothberg, F. Papadimitrakopoulos, M. E. Galvin, and T. M. Miller. Spatially indirect excitons as primary photoexcitations in conjugated polymers. *Phys. Rev. Lett.*, 72:1104, 1994.
19. L. J. Rothberg, M. Yan, F. Papadimitrakopoulos, M. E. Galvin, E. W. Kwock, and T. M. Miller. Photophysics of phenylenevinylene polymers. *Synth. Met.*, 80:41, 1996.

20. M. Yan, L. J. Rothberg, F. Papadimitrakopoulos, M. E. Galvin, and T. M. Miller. Defect quenching of conjugated polymer luminescence. *Phys. Rev. Lett.*, 73:744, 1994.
21. N. T. Harrison, G. R. Hayes, R. T. Phillips, and R. H. Friend. Singlet intrachain exciton generation and decay in poly(p-phenylenevinylene). *Phys. Rev. Lett.*, 77:1881, 1996.
22. D. G. J. Sutherland, J. A. Carlisle, P. Elliker, G. Fox, T. W. Hagler, I. Jimenez, H. W. Lee, K. Pakbaz, L. J. Terminello, S. C. Williams, F. J. Himpsel, D. K. Shuh, W. M. Tong, J. J. Jia, T. A. Callcott, and D. L. Ederer. Photo-oxidation of electroluminescent polymers studied by core-level photoabsorption spectroscopy. *Appl. Phys. Lett.*, 68:2046, 1996.
23. Ji Yu, Dehong Hu, and Paul F. Barbara. Unmasking electronic energy transfer of conjugated polymers by suppression of O<sub>2</sub> quenching. *Science*, 289:1327, 2000.
24. Jeong-Ik Lee, Gerrit Klaerner, and Robert D. Miller. Oxidative stability and its effect on the photoluminescence of poly(fluorene) derivatives: end group effects. *Chem. Mater.*, 11:1083, 1999.
25. B. Kraabel, V. I. Klimov, R. Kohlman, S. Xu, H-L. Wang, and D. W. McBranch. Unified picture of the photoexcitations in phenylene-based conjugated polymers: Universal spectral and dynamical features in subpicosecond transient absorption. *Phys. Rev. B: Condens. Matter Mater. Phys.*, 61:8501, 2000.
26. R. Jakubiak, C. J. Collison, W. C. Wan, Lewis J. L.J. Rothberg, and B. R. Hsieh. Aggregation quenching of luminescence in electroluminescent conjugated polymers. *J. Phys. Chem. A*, 103:2394, 1999.
27. Arvydas Ruseckas, Mathias Theander, Mats R. Andersson, Mattias Svensson, Maurizio Prato, Olle Inganäs, and Villy Sundström. Ultrafast photogeneration of inter-chain charge pairs in polythiophene films. *Chem. Phys. Lett.*, 322:136, 2000.
28. D. Beljonne, Z. Shuai, J. Cornil, D. A. dos Santos, and J. L. Bredas. On the nature of electronic excitations in poly(paraphenylenevinylene): A quantum-chemical investigation. *J. Chem. Phys.*, 111:2829, 1999.
29. Christopher J. Collison, Lewis J. Rothber, Varaporn Treemaneeekarn, and Yi Li. Conformational effects on the photophysics of conjugated polymers: a two species model for MEH-PPV spectroscopy and dynamics. *Macromolecules*, 34:2436, 2001.

30. R. Lecuiller, J. Berrehar, C. Lapersonne-Meyer, and M. Schott. Dual resonance fluorescence of polydiacetylene chains isolated in their crystalline monomer matrix. *Phys. Rev. Lett.*, 80:4068, 1998.
31. D. Beljonne, J. Cornil, R. Silbey, P. Millie, and J. L. Bredas. Interchain interactions in conjugated materials: the exciton model versus the supermolecular approach. *J. Chem. Phys.*, 112:4749, 2000.
32. Dieter Neher. Substituted rigid rod-like polymers – building blocks for photonic devices. *Adv. Mater.*, 7:691, 1995.
33. Ananda M. Sarker, Liming Ding, Paul M. Lahti, and Frank E. Karasz. Synthesis and luminescent studies of poly(phenylenevinylene)s containing a biphenyl moiety. *Macromolecules*, 35:223, 2002.
34. Bubin Xu, Jianheng Zhang, and Zhonghua Peng. Poly[(p-phenylene vinylene)-alt-(2,2'-biphenylene vinylene)]s: new conjugated polymers with high solid state photoluminescence quantum efficiencies. *Synth. Met.*, 113:35, 2000.
35. G. R. Hayes, I. D. W. Samuel, and R. T. Philips. Exciton dynamics in electroluminescent polymers studied by femtosecond time-resolved photoluminescence spectroscopy. *Phys. Rev. B*, 52:11569, 1995.
36. G. R. Hayes, I. D. W. Samuel, and R. T. Phillips. Ultrafast high-energy luminescence in a high-electron-affinity conjugated polymer. *Phys. Rev. B*, 54:8301, 1996.
37. U. Rauscher, H. Bassler, D. D. C. Bradley, and M. Hennecke. Exciton versus band description of the absorption and luminescence spectra in poly(p-phenylenevinylene). *Phys. Rev. B*, 42:9830, 1990.
38. Niyazi Serdar Sariciftci. *Primary photoexcitations in conjugated polymers: molecular exciton versus semiconductor band model*. World Scientific, River Edge, NJ, 97.
39. S. Heun, R. F. Mahrt, A. Greiner, U. Lemmer, H. Bassler, D. A. Halliday, D. D. C. Bradley, P. L. Burn, and A. B. Holmes. Conformational effects in poly(p-phenylene vinylene)s revealed by low-temperature site-selective fluorescence. *J. Phys.: Condens. Matter*, 5:247, 1993.
40. Paul F. Van Hutten, Victor V. Krasnikov, and Georges Hadziioannou. A model oligomer approach to light-emitting semiconducting polymers. *Acc. Chem. Res.*, 32:257, 1999.

41. S. Mazumdar and F. Guo. Observation of three resonances in the third harmonic generation spectrum of conjugated polymers: Evidence for the four-level essential states model. *J. Chem. Phys.*, 100:1665, 1994.
42. A. Kohler, D. A. dos Santos, D. Beljonne, Z. Shuai, J.-L. Bredas, A. B. Holmes, A. Kraus, K. Mullen, and R. H. Friend. Charge separation in localized and delocalized electronic states in polymeric semiconductors. *Nature*, 392:903, 1998.
43. E. S. Maniloff, V. I. Klimov, and D. W. McBranch. Intensity-dependent relaxation dynamics and the nature of the excited-state species in solid-state conducting polymers. *Phys. Rev. B*, 56:1876, 1997.
44. M. Y. Lavrentiev and W. Barford.  $1^1B_u - 2^1A_g^+$  crossover in conjugated polymers: The phase diagram of the molecular-orbital model. *Phys. Rev. B*, 59:15048, 1999.
45. Z. G. Soos, S. Ramasesha, and D. S. Galvao. Band to correlated crossover in alternating Hubbard and PPP chains: nature of the lowest singlet excitation of conjugated polyers. *Phys. Rev. Lett.*, 71:1609, 1993.
46. F. Guo, D. Guo, and S. Mazumdar. Intensities of two-photon absorptions to low-lying even-parity states in linear-chain conjugated polymers. *Phys. Rev. B*, 49:10102, 1994.
47. J. M. Leng, S. Jeglinski, X. Wei, R. E. Benner, Z. V. Vardeny, F. Guo, and S. Mazumdar. Optical probes of excited states in poly(p-phenylenevinylene). *Phys. Rev. Lett.*, 72:156, 1994.
48. M. Chandross, S. Mazumdar, S. Jeglinski, X. Wei, Z. V. Vardeny, E. W. Kwock, and T. M. Miller. Excitons in poly(para-phenylenevinylene). *Phys. Rev. B*, 50:14702, 1994.
49. A. Mathy, K. Ueberhofen, R. Schenk, H. Gregorius, R. Garay, K. Mullen, and C. Bubeck. Third-harmonic-generation spectroscopy of poly(p-phenylenevinylene): a comparison with oligomers and scaling laws for conjugated polymers. *Phys. Rev. B*, 53:4367, 1996.
50. I. H. Campbell, T. W. Hagler, D. L. Smith, and J. P. Ferraris. Direct measurement of conjugated polymer electronic excitation energies using metal/polymer/metal structures. *Phys. Rev. Lett.*, 76:1900, 1996.
51. K. Pakbaz, C. H. Lee, A. J. Heeger, T. W. Hagler, and D. McBranch. Nature of the primary photoexcitations in poly(arylene-vinylenes). *Synth. Met.*, 64:295, 1994.

52. R. N. Marks, J. J. M. Halls, D. D. C. Bradley, R. H. Friend, and A. B. Holmes. The photovoltaic response in poly(p-phenylene vinylene) thin-film devices. *J. Phys., Condens. Matter*, 6:1379, 1994.
53. M. Deussen, M. Scheidler, and H. Bassler. Electric-field-induced photoluminescence quenching in thin-film light-emitting-diodes based on poly(phenyl-p-phenylene vinylene). *Synthetic Metals*, 73:123, 1995.
54. P. Gomes da Costa and E. M. Conwell. Excitons and the band gap in poly(phenylene vinylene). *Phys. Rev. B*, 48:1993, 1993.
55. Z. Shuai, J. L. Bredas, and W. P. Su. Nature of photoexcitations in poly(paraphenylene vinylene) and its oligomers. *Chem. Phys. Lett.*, 228:301, 1994.
56. M. Chandross and S. Mazumdar. Coulomb interactions and linear, nonlinear and triplet absorption in poly(para-phenylenevinylene). *Phys. Rev. B*, 55:1497, 1997.
57. T. Hasegawa, Y. Iwasa, H. Sunamura, T. Koda, Y. Tokura, H. Tachibana, M. Matsumoto, and S. Abe. Nonlinear optical spectroscopy on one dimensional excitons in silicon polymer, polysilane. *Phys. Rev. Lett.*, 69:668, 1992.
58. David Yaron. Nonlinear optical response of conjugated polymers: essential excitations and scattering. *Phys. Rev. B: Condens. Matter*, 54:4609, 1996.
59. Melissa A. Pasquinelli and David Yaron. Energy landscapes for effective particles in conjugated polymers. *Synth. Met.*, 101:518, 1999.
60. Youji Jurihara, Yruiko Aoki, and Akira Imamura. Calculations of the excitation energies of all-trans and 11,12s-dicis retinals using localized molecular orbitals obtained by the elongation method. *J. Chem. Phys.*, 107:3569, 1997.
61. Youji Kurihara and Yuriko Imamura Akira Aoki. Calculations of phase transition of polydiacetylenes using localized molecular orbitals by elongation method. *J. Chem. Phys.*, 108:10303, 1998.
62. I. Ohmine, M. Karplus, and K. Schulten. Renormalized configuration interaction method for electron correlation in the excited states of polyenes. *J. Chem. Phys.*, 68:2298, 1978.
63. R. A. Goldbeck and E. Switkes. Localized excitation analysis of the singlet excited states of polyenes and diphenylpolyenes. *J. Phys. Chem.*, 89:2585, 1985.

64. Igor V. Kurnikov and David N. Beratan. Ab initio based effective Hamiltonians for long-range electron transfer: Hartree Fock analysis. *J. Chem. Phys.*, 105:9561, 1996.
65. Yongqiang Xue, Supriyo Datta, and Mark A. Ratner. Charge transfer and band lineup in molecular electronic devices: A chemical and numerical interpretation. *J. Chem. Phys.*, 115:4292, 2001.
66. T. S. Elicker, J. S. Binette, and D. G. Evans. Topological effects in electron transfer: Applications to dendrimers and branched molecules. *J. Phys. Chem. B*, 105:370, 2001.
67. Robert J. Cave and Marshall D. Newton. Calculation of electronic coupling matrix elements for ground and excited state electron transfer reactions: Comparison of the generalized Mulliken-Hush and block diagonalization methods. *J. Chem. Phys.*, 106:9213, 1997.
68. Eric D. Glendening. Natural energy decomposition analysis: explicit evaluation of electrostatic and polarization effects with application to aqueous clusters of alkali metal cations and neutrals. *J. Am. Chem. Soc.*, 118:2473, 1996.
69. Jason D. Weibel and David Yaron. INDO/SCI in periodic boundary conditions: the absorption spectrum of poly(para-phenylene vinylene). *J. Chem. Phys.* (submitted).
70. Jason D. Weibel. *New methodologies for electronic structure calculations on organic materials*. PhD thesis, Carnegie Mellon University, 2001.
71. Eric E. Moore and David Yaron. An explicit-solvent dynamic-dielectric screening model of electron-hole interactions in conjugated polymers. *J. Chem. Phys.*, 109:6147, 1998.
72. Eric. E. Moore. *Solid state effects on the electronic structure of conjugated polymers*. PhD thesis, Carnegie Mellon University, 2000.
73. H Schlick, F. Stelzer, F. Meghdadi, and G. Leising. Synthesis and optical characterization of new highly luminescent poly(m,p-phenylenevinylene) derivatives. *Synth. Met.*, 119:529, 2001.
74. Taek Ahn, Min Sik Jang, Hong-Ku Shim, Do-Hoon Hwang, and Taehyoung Zyung. Blue electroluminescent polymers: control of conjugation length by kink linkages and substituents in the poly(p-phenylenevinylene) related copolymers. *Macromolecules*, 32:3279, 1999.

75. M. Nisoli, S. Stagira, M. Zavelani-Rossi, S. DeSilvestri, P. Mataloni, and C. Zenz. Ultrafast light-emission processes in poly(para-phenylene)-type ladder polymer films. *Phys. Rev. B*, 59:11328, 1999.
76. T. W. Hagler, K. Pakbaz, and A. J. Heeger. Polarized electroabsorption spectroscopy of highly ordered poly(2-methoxy,5-(2'-ethyl-hexoxy)-p-phenylene vinylene. *Phys. Rev. B*, 51:14199, 1994.
77. Phillip Wood, Ifor D. W. Samuel, Richard Schrock, and Ronald L. Christensen. Conformational disorder in long polyenes. *J. Chem. Phys.*, 115:10955, 2001.
78. Attila Szabo and Neil S Ostlund. *Modern quantum chemistry introduction to advanced electronic structure theory*. Dover Publications, Mineola, N.Y, 96.
79. K. Ohno. Some remarks on the Pariser-Parr-Pople method. *Theor. Chim. Acta*, 2:219, 1964.
80. J. Ridley and M. Zerner. An intermediate neglect of differential overlap technique for spectroscopy: pyrrole and the azines. *Theor. Chim. Acta*, 32:111, 1973.
81. J. Fernandez Rico, R. Lopez, and G. Ramirez. Molecular integrals with Slater basis. II. fast computational algorithms. *J. Chem. Phys.*, 91:4213, 1989.
82. David Yaron. Equation-of-motion calculations on an isolated chain of polyacetylene. *Mol. Cryst. Liq. Cryst. Sci. Technol., Sect. A*, 256:631, 1994.
83. Lionel Salem. *The molecular orbital theory of conjugated systems*. W. A. Benjamin, New York, 66.
84. P. Tavan and K. Schulten. Electronic excitations in finite and infinite polyenes. *Phys. Rev. B*, 36:4337, 1987.
85. F. B. Gallagher and F. C. Spano. Theory of biexcitons in one-dimensional polymers. *Phys. Rev. B*, 53:3790, 1996.
86. William H Press. *Numerical recipes in C: the art of scientific computing*. Cambridge University Press, Cambridge Cambridgeshire, New York, 2nd ed edition, 1992.
87. Eric Moore and David Yaron. Models of Coulomb screening and exciton binding in conjugated polymers. *Synth. Met.*, 85:1023, 1997.
88. Melissa A. Pasquinelli and David Yaron. Quantum-chemical investigation of chemical defects in conjugated polymers using the effective particle approach. (manuscript in preparation).

89. Melissa A. Pasquinelli and David Yaron. Quantum-chemical investigation of chemical disorder in conjugated polymers using the effective particle approach. (manuscript in preparation).
90. Janos G. Angyan and Gabor Naray-Szabo. Chemical fragmentation approach to the quantum chemical description of extended systems. In Z. B. Maksic, editor, *Theoretical methods of chemical bonding Part 4: Theoretical treatment of large molecules and their interactions*, pages 2–49. Springer-Verlag, Berlin, 91.
91. Gabor Naray-Szabo. Chemical fragmentation in quantum mechanical methods. *Computers and Chemistry*, 24:287, 2000.
92. Gabor Naray-Szabo. Chemical fragmentation in a quantum mechanical treatment of extended covalent systems. *Russian Journal of Physical Chemistry*, 74:34, 2000.
93. Akira Imamura, Yuriko Aoki, and Koji Maekawa. A theoretical analysis of polymers by using uniform localization of molecular orbitals: proposal of an elongation method. *J. Chem. Phys.*, 95:5, 1991.
94. Yuriko Aoki and Akira Imamura. Local density of states of aperiodic polymers using the localized orbitals from an ab initio elongation method. *J. Chem. Phys.*, 97:8432, 1992.
95. M. Sironi, A. Famulari, M. Raimondi, and S. Chiesa. The transferability of extremely localized molecular orbitals. *J. Mol. Struct.*, 529:47, 2000.
96. S. F. Boys. Construction of some molecular orbitals to be approximately invariant for changes from one molecule to another. *Rev. Mod. Phys.*, 32:296, 1960.
97. Clyde Edmiston and Klaus Ruedenberg. Localized atomic and molecular orbitals. *Rev. Mod. Phys.*, 35:457, 1963.
98. W. von Niessen. Density localization of atomic and molecular orbitals I. *J. Chem. Phys.*, 56:4290, 1972.
99. Janos Pipek and Paul G. Mezey. A fast intrinsic localization procedure applicable for ab initio and semiempirical linear combination of atomic orbital wave functions. *J. Chem. Phys.*, 90:4916, 1989.
100. V. Magnasco and A. Perico. Uniform localization of atomic and molecular orbitals I. *J. Chem. Phys.*, 47:971, 1967.

101. V. Magnasco and A. Perico. Uniform localization of atomic and molecular orbitals II. *J. Chem. Phys.*, 48:800, 1968.
102. A. Ramirez-Solis and Ramon Hernandez-Lomoneda. Localized orbitals for molecular calculations. *Revista Mexicana de Fisica*, 42:911, 1996.
103. Karl Jug and Heiko Gerwens. Quantum chemical model for electrostatic effects in biomolecules. *J. Phys. Chem. B*, 102:5217, 1998.
104. A. M. Tokmachev and A. L. Tchougreeff. Semiempirical implementation of strictly localized geminals for analysis of molecular electronic structure. *J. Comp. Chem.*, 22:752, 2000.
105. Juan Carlos Paniagua and Albert Moyano. Localization-consistent electronic energy partitions. *Int. J. Quant. Chem.*, 65:121, 1997.
106. Satoshi Yokojima, XiuJun Wang, DongHau Zhou, and GuanHua Chen. Localized-density-matrix, segment-molecular-orbitals and poly(p-phenylenevinylene) aggregates. *J. Chem. Phys.*, 111:10444, 1999.
107. A. I. Panin and O. V. Sizova. Construction of molecular orbitals localized on polyatomic fragments. *J. Struct. Chem*, 39:464, 1998.
108. Roman Boca. An extended PCILO method. *Theor. Chim. Acta*, 61:179, 1982.
109. Yirong Mo, Jiali Gao, and Sigrid D. Peyerimhoff. Energy decomposition analysis of intermolecular interactions using a block-localized wave function approach. *J. Chem. Phys.*, 112:5530, 2000.
110. Yirong Mo and Sigrid D. Peyerimhoff. Theoretical analysis of electronic delocalization. *J. Chem. Phys.*, 109:1687, 1998.
111. Yirong Mo and Jiali Gao. Ab initio QM/MM simulations with a molecular orbital-valence bond (MOVb) method: application to an SN2 reaction in water. *J. Comp. Chem*, 21:1458, 2000.
112. James J. P. Stewart. Application of localized molecular orbitals to the solution of semiempirical self-consistent field equations. *Int. J. Quant. Chem.*, 58:133, 1996.
113. Marc Couty, Craig A. Bayse, and Michael B. Hall. Extremely localized molecular orbitals (ELMO): a non-orthogonal Hartree-Fock method. *Theor. Chim. Acta*, 97:96, 1997.
114. A. Lazar and P. R. Surjan. The nature of electronic excitations in singly bonded C<sub>60</sub> dimer. *J. Mol. Struct.*, 501:369, 2000.

115. A. Ramirez-solis and J. P. Daudey. Theoretical study of the spectroscopy of low-lying electronic states of the CuF molecule. *Chem. Phys.*, 134:111, 1989.
116. Jun Maki, Hiroya Yamagishi, Takeshi Noro, Fukashi Sasaki, and Yuichi Yamamoto. New localized molecular orbitals appropriate for post Hartree-Fock calculations. *Int. J. Quant. Chem.*, 60:731, 1996.
117. P. O. Lowdin. J. chem. phys. *J. Chem. Phys.*, 18:365, 1950.
118. M. J. S. Dewar, E. G. Zoebisch, E. F. Healy, and J. J. P. Stewart. Am1: A new general purpose quantum mechanical molecular model. *J. Am. Chem. Soc.*, 107:3902, 1985.
119. P. W. Atkins. *Molecular Quantum Mechanics*. Oxford University Press, Oxford, second edition, 1983. note: Several mistakes were found in the formulas in the book; corrections are reflected in the equations given in this report.
120. S. Son, A. Dodabalapur, A. J. Lovinger, and M. E. Galvin. Luminescence enhancement by the introduction of disorder into poly(p-phenylene vinylene). *Science*, 269:376, 1995.
121. Rafael Gomes, Jose L. Segura, and Nazario Martin. Synthesis and characterization of novel optically active polyarylene vinylenes with controlled effective conjugation length. *J. Org. Chem.*, 65:7501, 2000.
122. J. J. P. Stewart. Optimization of parameters for semiempirical methods. *J. Comp. Chem.*, 10:209, 1989.
123. Mattias Hjort and Sven Stafstrom. Localization in quasi-one-dimensional systems. *Phys. Rev. B*, 62:5245, 2000.
124. I. D. W. Samuel, I. Ledoux, C. Dhenaut, J. Zyss, H. H. Fox, R. R. Schrock, and R. J. Silbey. Saturation of cubic optical nonlinearity in long-chain polyene oligomers. *Science*, 265:1070, 1994.
125. Mark N. Kobrak and Eric R. Bittner. A quantum molecular dynamics study of exciton self-trapping in conjugated polymers: temperature dependence and spectroscopy. *J. Chem. Phys.*, 112:7684, 2000.
126. T. Kobayashi, J. Hamazaki, M. Arakawa, H. Kunugita, K. Ema, K. Ochiai, M. Rikukawa, and K. Sanui. Self-trapped exciton dynamics in highly ordered and disordered films of polythiophene derivative. *Phys. Rev. B*, 62:8580, 2000.
127. G. R. Hayes, I. D. W. Samuel, and R. T. Phillips. Polarization dependence of the ultrafast photoluminescence of oriented poly(p-phenylenevinylene). *Phys. Rev. B*, 56:3838, 1997.

128. R. Kersting, U. Lemmer, R. F. Mahrt, K. Leo, H. Kurz, H. Bassler, and E. O. Gobel. Femtosecond energy relaxation in  $\pi$ -conjugated polymers. *Phys. Rev. Lett.*, 70:3820, 1993.
129. S. C. J. Meskers, J. Hubner, M. Oestreich, and H. Bassler. Time-resolved fluorescence studies and Monte Carlo simulations of relaxation dynamics of photoexcitations in a polyfluorene film. *Chem. Phys. Lett.*, 339:223, 2001.
130. G. Padmanaban and S. Ramakrishnan. Conjugation length control in soluble MEH-PPV: synthesis, optical properties, and energy transfer. *J. Am. Chem. Soc.*, 122:2244, 2000.
131. Stoyan Karabunarliev, Martin Baumgarten, Eric R. Bittner, and Klaus Mullen. Rigorous Frank-Condon absorption and emission spectra of conjugated oligomers from quantum chemistry. *J. Chem. Phys.*, 113:11372, 2000.
132. Gil C. Claudio and Eric R. Bittner. Random growth statistics of long-chain single molecule poly(p-phenylene vinylene). *J. Chem. Phys.*, 115:9585, 2001.
133. Mark N. Kobrak and Eric R. Bittner. A dynamic model for exciton self-trapping in conjugated polymers. I. theory. *J. Chem. Phys.*, 112:5399, 2000.
134. Mark N. Kobrak and Eric R. Bittner. A dynamic model for exciton self-trapping in conjugated polymers. II. implementation. *J. Chem. Phys.*, 112:5410, 2000.
135. V.R. Saunders and J.H. Van Lenthe. The direct CI method. A detailed analysis. *Molec. Phys.*, 100:167, 2002.
136. Aimee Tomlinson and David Yaron.
137. H. Haken and S. Nikitine. *Excitons at High Density*. Springer-Verlag, New York, 75.
138. A. Chakrabarti, A. Schmidt, V. Valencia, B. Fluegel, S. Mazumdar, N. Armstrong, and N. Peyghambarian. Evidence for exciton-exciton binding in a molecular aggregate. *Phys. Rev. B*, 57:4206, 1998.
139. M. Kuwata-Gonokami, N. Peyghambarian, K. Meissner, B. Fluegel, Y. Sato, K. Ema, R. Shimano, S. Mazumdar, F. Guo, T. Tokihiro, H. Ezaki, and E. Hanamura. Exciton strings in an organic charge-transfer crystal. *Nature (London)*, 367:47, 1994.
140. V. I. Klimov, D. W. McBranch, N. Barashkov, and J. Ferraris. Biexcitons in  $\pi$ -conjugated oligomers: Intensity-dependent femtosecond transient-absorption study. *Phys. Rev. B*, 58:7654, 1998.

141. V. Klimov, D. McBranch, N. Barashkov, and J Ferraris. Exciton and biexciton signatures in femtosecond transient absorption of  $\pi$ -conjugated oligomers. *Proc. SPIE-Int. Soc. Opt. Eng.*, 3145:58, 1997.
142. V. I. Klimov, D. W. McBranch, N. N. Barashkov, and J. P. Ferraris. Femtosecond dynamics of excitons in  $\pi$ -conjugated oligomers: the role of intrachain two-exciton states in the formation of interchain species. *Chem. Phys. Lett.*, 277:109, 1997.
143. B. Kraabel and D. W. McBranch. Subpicosecond study of excitons in a phenylenevinylene conjugated polymer: exciton-exciton interactions and infrared photoinduced absorption features. *Chem. Phys. Lett.*, 330:403, 2000.
144. J. M. Leng, D. Dick, X. Wei, Z. V. Vardeny, F. Guo, and S. Mazumdar. Excited energy states in poly(p-phenylenevinylene). *Mol. Cryst. Liq. Cryst. Sci. Technol., Sect. A*, 256:1, 1994.
145. F. Guo, M. Chandross, and S. Mazumdar. Stable biexcitons in conjugated polymers. *Phys. Rev. Lett.*, 74:2086, 1995.
146. A. Chakrabarti and S. Mazumdar. Theory of even-parity states in polyphenylenes. *Phys. Rev. B*, 59:4839, 1999.
147. M. Chandross, F. Guo, and S. Mazumdar. Excitons and biexcitons in poly(paraphenylenevinylene). *Synth. Met.*, 69:625, 1995.
148. F. Guo, M. Chandross, and S. Mazumdar. Theory of biexcitons in  $\pi$ -conjugated polymers. *Mol. Cryst. Liq. Cryst. Sci. Technol., Sect. A*, 256:53, 1994.
149. S. Mazumdar, F. Guo, K. Meissner, B. Fluegel, and N. Peyghambarian. Exciton-to-biexciton transition in quasi-one-dimensional organics. *J. Chem. Phys.*, 104:9292, 1996.
150. M. Chandross, Y. Shimoi, and S. Mazumdar. Systematic characterization of excited states in  $\pi$ -conjugated polymers. *Chem. Phys. Lett.*, 280:85, 1997.
151. V. A. Shakin and S. Abe. Two-photon absorption in conjugated polymers: Contributions of excitonic and biexcitonic states. *Phys. Rev. B*, 50:4306, 1994.
152. S. Abe, Y. Shimoi, V. A. Shaken, and K. Harigaya. Excitation effects in the optical properties of conjugated polymers and fullerenes. *Mol. Cryst. Liq. Cryst. Sci. Technol., Sect. A*, 256:97, 1994.
153. F. C. Spano. Pump-probe spectrum of interacting one-dimensional excitons: biexcitons and J-aggregates. *Chem. Phys. Lett.*, 234:29, 1995.

154. F. B. Gallagher and F. C. Spano. Theory of biexcitons in conjugated polymers. *Synth. Met.*, 85:1007, 1997.
155. Kunio Ishida, Hideo Aoki, and Tetsuo Ogawa. Biexciton on a one-dimensional lattice. *Phys. Rev. B: Condens. Matter*, 52:8980, 1995.
156. Z. G. Yu, R. T. Fu, C. Q. Wu, X. Sun, and K. Nasu. Excitons, biexcitons, and the band gap in poly(p-phenylene vinylene). *Phys. Rev. B: Condens. Matter*, 52:4849, 1995.
157. Stephane Pleutin. Excitonic strings in one-dimensional organic compounds. *Phys. Rev. B: Condens. Matter Mater. Phys.*, 61:4554, 2000.
158. S. Mazumdar, D. Guo, and S. N. Dixit. High energy two-photon states in finite versus infinite polymers. *J. Chem. Phys.*, 96:6862, 1992.
159. Frank C. Spano and Jasper Knoester. Fermions on a Frenkel chain: Nonlinear optical response of linear aggregates. *Adv. Magn. Opt. Reson.*, 18:117, 1994.
160. Frank C. Spano. Fermion excited states in one-dimensional molecular aggregates with site disorder: nonlinear optical response. *Phys. Rev. Lett.*, 67:3424, 1991.
161. F. C. Spano. Multiple-photon absorption and saturation in Frenkel-exciton chains. *Physical Review B*, 46:13017, 92.
162. Frank C. Spano and Eric S Manas. Theory of coherent transient spectroscopy in molecular aggregates: the effects of interacting excitons. *J. Chem. Phys.*, 103:5939, 1995.
163. Rudolph Pariser and Robert G. Parr. A semi-empirical theory of the electronic spectra and electronic structure of complex unsaturated molecules. I. *J. Chem. Phys.*, 21:466, 1953.
164. J. A. Pople. Electron interaction in unsaturated hydrocarbons. *Trans. Faraday Soc.*, 49:1375, 1953.
165. Shaul Mukamel. *Principles of nonlinear optical spectroscopy*. Oxford University Press, New York, 95.